UNIVERSIDADE DE SÃO PAULO
INSTITUTO DE FÍSICA DE SÃO CARLOS

LUCAS GABRIEL RABELO

Development of sputtered $BiVO_4$ - CuO Tandem cells for bias-free solar water splitting

São Carlos
2023

LUCAS GABRIEL RABELO

Development of sputtered $BiVO_4$ - CuO Tandem cells for bias-free solar water splitting

Dissertation presented to the Graduate Program in Physics at the Instituto de Física de São Carlos, Universidade de São Paulo, to obtain the degree of Master of Science.

Concentration area: Theoretical and Experimental Physics .

Advisor: Prof. Dr. Renato Vitalino Gonçalves

Corrected Version
(original version available on the Program Unit)

São Carlos
2023

Rabelo, Lucas Gabriel
Development of sputtered BiVO4 - CuO Tandem cells for bias-free solar water splitting / Lucas Gabriel Rabelo; advisor Renato Vitalino Gonçalves - corrected version -- São Carlos 2023.
110 p.

Dissertation (Master's degree - Graduate Program in Theoretical and Experimental Physics) -- Instituto de Física de São Carlos, Universidade de São Paulo - Brasil , 2023.

1. PEC water splitting. 2. Tandem cell. 3. Semiconductors. 4. Bismuth vanadate. 5. p-n heterojunctions. I. Gonçalves, Renato Vitalino, advisor. II. Title.

ACKNOWLEDGEMENTS

I would like to express my gratitude to Prof. Renato V. Gonçalves for his exceptional mentorship and unwavering support since the beginning of my scientific carrier.

A very special thanks to Dr. Washington Rosa for all the insightful discussions and significant contributions made throughout the past four years. His expertise and guidance have been instrumental in the success of this work.

I am very grateful to all group colleagues who contributed directly or indirectly to this work, especially Andressa, Higor, Fiacre, Jessenia, Yara, Luis, and Gabriel. I also thank the NaCA group team (Inês, Cássio, Geraldo, Manoel, Luiz, and Érica) for providing all the necessary support for this work.

Finally, I would like to thank CAPES (process 88887.601485/2021-00) and FAPESP (Grant 2017/18716-3, schoolarship 2019/18724-1) for funding this research project. I also thank the National Center for Energy and Materials Research (CNPEM) for the experimental facilities (INTERCOVAMEX H2 sputtering system).

THIS STUDY WAS FINANCED IN PART BY THE COORDINATION FOR THE IMPROVEMENT OF HIGHER EDUCATION PERSONNEL – BRAZIL (CAPES) – FINANCE CODE 001.

ABSTRACT

RABELO, L. G. **Development of sputtered $BiVO_4$ – CuO Tandem cells for bias-free solar water splitting.** 2023. 110 p. Dissertation (Master in Science) - Instituto de Física de São Carlos, Universidade de São Paulo, São Carlos, 2023.

Photoelectrochemical (PEC) water splitting has been considered as a promising technique for converting abundant solar energy into clean and renewable hydrogen (H_2) fuel. Recently, Tandem PEC cells based on stable and low-cost metal oxides have attracted tremendous attention for cleaving water molecules into green H_2 assisted only by solar energy. In this work, $BiVO_4/FeNiO_x$ photoanodes and CuO photocathodes were synthesized via magnetron sputtering deposition to perform oxygen and hydrogen evolution reactions (OER and HER), respectively, in a simple and low-cost Tandem PEC cell. In particular, the all-sputtered $BiVO_4/FeNiO_x$ photoanode showed excellent PEC performance and chemical stability for OER, achieving a high photocurrent density of $+1.22$ mA cm^{-2} and a charge transfer efficiency of 96 % at the water oxidation potential. In contrast, the all-sputtered CuO photocathode exhibited a modest PEC performance for HER, with an onset potential at 1.03 V vs. RHE (reversible hydrogen electrode) and photocurrent density of -0.35 mA cm^{-2} at $+0.40$ V vs. RHE. In this work, we also introduced a feasible model based on classical band theory to evaluate the interfacial band alignment of photoelectrodes under working conditions for PEC water splitting. Our energy band diagrams under simulated illumination demonstrated that the photogenerated holes (electrons) at the $BiVO_4/FeNiO_x$ (CuO) film have enough energy to perform the OER (HER) without external bias. Encouragingly, our novel $BiVO_4/FeNiO_x$ - CuO Tandem PEC device produced a stable operating photocurrent density of ~ 50 μA cm^{-2} under zero-bias and AM 1.5G illumination for at least 1000 seconds, evidencing the occurrence of bias-free solar water splitting reactions. Nevertheless, our proposed Tandem system is still far from meeting the requirements for practical applications due to the severe chemical instability and low photocurrent density of the CuO film. Therefore, further studies must be directed towards producing protective layers, inducing p-n heterojunction, and depositing HER cocatalysts for enhancing the chemical stability and PEC performance of the CuO film. In summary, we aimed herein to propose a scalable methodology for developing metal oxide-based Tandem PEC cells and to introduce suitable tools for assessing interfacial band alignment of photoelectrodes under working conditions for PEC water splitting. This work also thoroughly

discusses the fundamental limitations, current challenges, and prospects for employing Tandem PEC devices to produce green hydrogen as a clean and renewable energy carrier.

Keywords: PEC water splitting. Tandem cell. Semiconductors. Bismuth vanadate. p-n heterojunctions.

RESUMO

RABELO, L.G. **Desenvolvimento de células Tandem $BiVO_4$-CuO para a divisão fotoeletroquímica da água sem o auxílio de polarização externa.** 2023. 110 p. Dissertação (Mestrado em Ciências) - Instituto de Física de São Carlos, Universidade de São Paulo, São Carlos, 2023.

A divisão fotoeletroquímica da água emerge como uma técnica promissora para converter a abundante energia solar em hidrogênio verde (H_2). Recentemente, o desenvolvimento de células Tandem baseadas em semicondutores óxidos metálicos estáveis e de baixo custo tem atraído muita atenção para a clivagem de moléculas de água no combustível H_2, auxiliada somente por energia solar. No presente trabalho, fotoanodos de $BiVO_4/FeNiO_x$ e fotocatodos de CuO foram sintetizados (via pulverização catódica) para realizar as meias reações de evolução de oxigênio (OER) e evolução de hidrogênio (HER) em um dispositivo Tandem simples e de baixo custo. Em particular, o fotoanodo $BiVO_4/FeNiO_x$ totalmente pulverizado apresentou excelente desempenho fotoeletroquímico e estabilidade química para a OER, alcançando uma alta densidade de fotocorrente de $+1.22$ mA cm^{-2} e uma eficiência de transferência de cargas de 96% no potencial de oxidação da água. Em contraste, o fotocatodo de CuO totalmente pulverizado exibiu um desempenho fotoeletroquímico modesto para a HER, exibindo um potencial de *onset* em 1.03 V vs. RHE (eletrodo de hidrogênio reversível) e densidade de fotocorrente de -0.35 mA cm^{-2} em $+0.40$ V vs. RHE. Nesse trabalho, nós também introduzimos um modelo baseado na teoria clássica de bandas para analisar o alinhamento interfacial de bandas dos fotoeletrodos sob condições de trabalho para a divisão fotoeletroquímica da água. Os resultados dos diagramas de bandas sob iluminação simulada demostraram que os buracos (elétrons) fotogerados no filme de $BiVO_4/FeNiO_x$ (CuO) possuem energia suficiente para realizar a OER (HER) sem polarização externa. Conclusivamente, nosso dispositivo Tandem $BiVO_4/FeNiO_x$ - CuO produziu uma densidade fotocorrente operacional estável de ~ 50 μA cm^{-2} sob iluminação AM 1.5G e polarização externa nula por pelo menos 1000 segundos, evidenciando a ocorrência das reações de divisão fotoeletroquímica da água livre de potenciais externos. Entretanto, nosso sistema Tandem proposto ainda está longe de atender aos requisitos para aplicações práticas devido à forte instabilidade química e baixa densidade de fotocorrente do filme de CuO. Portanto, estudos futuros devem ser direcionados para a produção de camadas protetoras, indução de heterojunções p-n e deposição de cocatalisadores para aumentar a estabilidade química e o desempenho fotoeletroquímico do filme de CuO. Em suma, nesse trabalho nós objetivamos propor uma metodologia escalável

para a produção de células Tandem PEC à base de óxidos metálico, assim como introduzir ferramentas adequadas para analisar o alinhamento interfacial de bandas dos fotoeletrodos sob condições de trabalho durante a divisão fotoeletroquímica da água. Essa dissertação também discute minuciosamente as limitações fundamentais, os desafios atuais e as perspectivas de empregar dispositivos Tandem PEC para produzir hidrogênio verde como um portador de energia limpa e sustentável.

Palavras-chave: Divisão fotoeletroquímica da água. Célula Tandem. Vanadato de bismuto. Semicondutores. Heterojunções p-n.

LIST OF FIGURES

LIST OF TABLES

LIST OF ABREVIATIONS AND ACRONYMS

ABPE	Applied bias photon-to-current efficiency
BVO	Bismuth vanadate
CB	Conduction band
CE	Counter electrode
EIS	Electrochemical impedance spectroscopy
FE	Faradaic efficiency
FTO	Fluorine doped tin oxide
HER	Hydrogen evolution reaction
IPCE	Incident photon-to current efficiency
KBi	Potassium borate buffer
MS	Mott-Schottky
OCP	Open circuit potential
OER	Oxygen evolution reaction
PEC	Photoelectrochemical
QFL	Quasi-fermi level
RE	Reference electrode
RHE	Reversible hydrogen electrode
SCLJ	semiconductor/liquid junction
SCR	Space charge region
SEM	Scanning electron microscopy
STH	Solar-to-hydrogen
VB	Valence band
WE	Working electrode
XPS	X-ray photoelectron spectroscopy
XRD	X-ray diffraction

LIST OF SYMBOLS

E_G	Bandgap energy
ΔG	Gibbs free energy
$\Delta\mu_{ex}$	Helmholtz free energy of photogenerated electron-hole pairs
E_F	Fermi energy
E_C	Conduction band edge (energy)
E_V	Valence band edge (energy)
N_A	Acceptor impurity concentration
N_D	Donor impurity concentration
E_{redox}	Redox energy
W	Depletion length in a space charge layer
Ψ_{bi}	Built-in potential
E_{app}	Applied potential
E_{Fn}	Quasi-Fermi energy level for electrons
E_{Fp}	Quasi-Fermi energy level for holes
E_{FB}	Flat-band potential
$\eta_{ox(red)}$	Overpotential for water oxidation (reduction)
V_{ph}	Photovoltage
a_{ph}	Photoelectrochemical affinity
j	Current density
j_{ph}	Photocurrent density
j_{OP}	Operating current density
$\Psi_{1(2)}$	Potential drop on the n(p)-side of a p-n heterojunction
$W_{1(2)}$	Depletion length on the n(p)-side of a p-n heterojunction
η_{STH}	Solar-to-hydrogen conversion efficiency
η_{sep}	Charge separation (transfer) efficiency
η_{cat}	Charge transfer efficiency
R_{CT}	Charge transfer resistance
V_{OC}	Open circuit potential

CONTENTS

1 INTRODUCTION

One of the main challenges confronting humanity today is identifying clean, renewable, and sustainable energy sources to meet the expanding global energy demand. As shown in Figure 1a, despite substantial progress in renewable energy in recent decades, fossil fuels (oil, coal, and natural gas) still account for more than 80% of the world's total energy supply.[1-2] In particular, fossil fuels have been responsible for the dramatic expansion in global energy production since the advent of the industrial revolution (~ 18th century) due to their excellent properties of high energy density, accessible storage, and transportation facilities.[3,4] However, the usage of fossil fuels has several well-known inherent problems, including the limited character and rapid depletion of their natural reserves, the geopolitical conflicts triggered by their territorial decentralization, the susceptibility to market manipulation and price fluctuations (as exemplified by the energy crisis followed by Russia's invasion of Ukraine), and, ultimately, the environmental issues associated with the emission of CO_2 and other greenhouse gases.

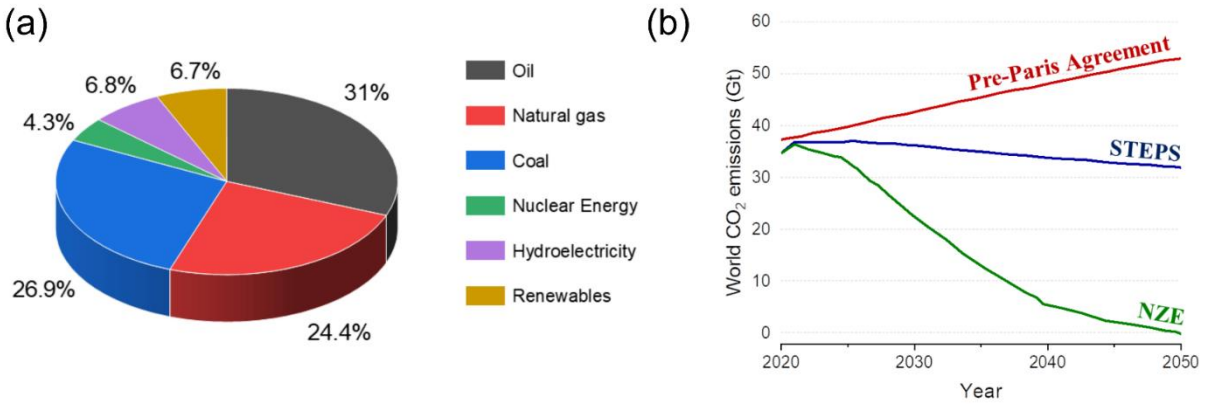

Figure 1 – (a) World total primary energy supply by source in 2021. (b) Energy-related CO_2 emissions between 2010 and 2050 as projected by the (IEA) pre-Paris, STEPS, and NZE scenarios.
Source: (a) STATISTICAL[1]…; (b) WORLD…[2]

As a result of the post-pandemic period in 2021, greenhouse gas emissions related to energy production reached their largest annual increase in history, amounting to an astonishing 36.6 Gt of CO_2.[2] According to the Stated Policy Scenario (STEPS) projected by the International Energy Agency (IEA), these CO_2 emissions will peak at 37 Gt before slowly decaying to 32 Gt in 2050 (Figure 1b), leading to a global average temperature rise of 2.5° by 2100.[2] Although this temperature increase is 1 °C lower than predicted before the Paris Agreement – indicating significant progress in policy changes since 2015 – STEPS can still not contain global warming at the upper well-established level of 1.5 °C. Therefore, the usage of renewable and carbon-free energy sources is critically important for the ideal Net Zero

Emission (NZE) scenario,[2,5] which, in turn, provides a trajectory of stabilization of the global average temperature at 1.5 °C through the reduction of CO_2 emissions to 23 Gt by 2030 and to zero by 2050 (Figure 1b).

In this context, hydrogen (H_2) has been regarded as a chemical fuel with significant potential to reduce (and replace) the usage of fossil fuels. It offers several advantages, including (i) high gravimetric density, (ii) carbon-free nature, (iii) absence of polluting gas emissions during its combustion, (iv) relatively easy transport and storage, and (v) versatility to be transformed into electricity and other derived fuels (e.g., ammonia and methanol).[6–9] To date, this versatile energy carrier has high demand ($\sim$94 Mt in 2021) in the refinery, industry, transport, construction, and electricity generation sectors. However, the majority of hydrogen production ($> 90\%$) still relies on fossil fuels, resulting in substantial CO_2 emissions of around 900 Mt in 2021.[6] Unfortunately, only $\sim$0.04% of the total H_2 demand has been met through water electrolysis, which is a clean and sustainable technique for producing this chemical fuel. Nevertheless, driven by various policies and growing investments, the IEA predicts a significant rise in the synthesis of renewable H_2 from water electrolysis technologies in the following years, estimating $\sim$14 Mt of H_2 by 2030 (an impressive 400-fold increase in just 9 years).[6]

In this regard, photoelectrochemical (PEC) water splitting has been considered a promising pathway for producing green H_2 using only water, semiconductors, and sunlight. Solar energy, in particular, is a clean, decentralized, inexhaustible, and plentiful energy source that provides over 23000 TWy of energy onto the surface of the Earth.[10–12] Remarkably, this energy is three orders of magnitude higher than the annual global energy consumption ($\sim$18.9 TWy in 2021),[1] evidencing that solar-based technologies are crucial for establishing a carbon-free society. Nevertheless, solar energy has inherent problems, such as the uneven illumination distribution throughout the Earth's surface and the sunlight's intermittent, variable, and diffuse nature.[11,13] Furthermore, solar energy cannot be directly utilized, requiring its capture and conversion into heat, electricity, or chemical fuels.[14] As a result, PEC water splitting emerges as a promising technique for storing solar energy into chemical bonds of H_2 molecules, thereby addressing the problems of sunlight storage and transport and providing an energy source with great potential for transitioning from fossil fuels to renewables.

Since the first solar-driven water splitting demonstration in 1972, several PEC configurations and novel semiconductor materials have been identified.[15] In a typical PEC device, a photoabsorber semiconductor drives either the hydrogen evolution reaction (HER) or the oxygen evolution reaction (OER), with a metallic counter electrode conducting the other

half-reaction. Unfortunately, these single photoabsorber-based PEC systems typically require external electric energy to meet the energy requirements for non-spontaneous overall water splitting. As a result, the concept of Tandem cells has been recently proposed to cleavage water molecules into green H_2 assisted only by solar energy.[16–18] Generally, Tandem cells are PEC devices where a combination of photoabsorber materials is applied for extending the light harvesting and producing charge carriers with enough driving force to overcome the energetic barriers for redox reactions. In the most straightforward Tandem approach, an n-type photoanode and a p-type photocathode are externally coupled to perform OER and HER, respectively. Remarkably, theoretical solar-to-hydrogen (STH) efficiencies of 20 to 30% have been predicted (for even) these simple Tandem devices,[16,18–20] which is far greater than the STH efficiency of 10%, currently regarded as the benchmark for practical applications.[21]

In this work, motivated by the promise of PEC technologies for producing green hydrogen, we developed a simple and low-cost Tandem device for bias-unassisted overall water splitting. Our novel Tandem cell comprised a $BiVO_4$-based photoanode for OER and a CuO photocathode for HER. $BiVO_4$, in particular, has been the most successful material for OER due to its narrow bandgap, suitable band structure, non-toxicity, abundance, and modest chemical stability.[22-23] Nevertheless, photocurrent densities for unmodified $BiVO_4$ films are still considerably lower than the theoretical maximum of 7.5 mA cm^{-2} due to its severe electron-hole recombination and sluggish water reaction kinetics.[24] Furthermore, since OER has been considered the bottleneck reaction for overall water splitting,[25] most of our efforts were dedicated to optimizing $BiVO_4$ films and mitigating their inherent problems. In contrast, despite the well-known chemical instability issues, the CuO photocathode was chosen because of its narrow bandgap of ~1.5 eV (allowing efficient visible light absorption), extremely high theoretical photocurrent density (~35 mA cm^2), and a band structure suitable for HER.[26,27]

In summary, our main objectives in this work can be listed in the following topics: (i) synthesize and optimize $BiVO_4$ and CuO films for OER and HER, respectively, (ii) apply surface modification on these films, aiming to achieve superior PEC performance and higher chemical stabilities, (iii) evaluate the interfacial band alignment and charge transfer properties in the PEC device, and ultimately (iv) investigate the ability of our novel Tandem cell for driving overall water splitting assisted only by solar energy. As a result, with this work, we intend to advance the development of a simple and low-cost PEC device that, with proper modifications, can be commercially applied for producing green H_2 on a large scale. Furthermore, we also aim to introduce simple tools for determining and elucidating the interfacial band alignment of photoelectrodes under working conditions for PEC water splitting.

2 THEORETICAL BACKGROUND

2.1 Photoelectrochemical (PEC) water splitting

PEC water splitting has been considered a promising clean and renewable pathway for storing sunlight energy into chemical bonds of high-energy H_2 molecules. The inspiration for PEC water splitting comes from natural photosynthesis, where essentially plants use solar energy to produce O_2 and glucose through the water photooxidation and CO_2 reduction reactions, respectively.[28-29] Similarly, PEC water splitting employs photo-absorbing semiconductors to carry out multi-electron transfer reactions that convert solar energy into chemical fuels. In essence, when a semiconductor (with bandgap E_G) receives photons with energy $h\nu \geq E_G$, electrons from its valence band (VB) are excited to the conduction band (CB), leaving electronic vacancies (holes) in the VB; these photogenerated electrons and holes, in turn, are responsible for the cleavage of water molecules. Importantly, the water splitting process involves two half-reactions: OER and HER. As shown in equations (1) to (4), the characteristic mechanisms involved in the OER and HER vary depending on the pH of the aqueous solution, while the overall water splitting is always described by equation (5).[30]

Acid and neutral condition:

OER: $2H_2O + 4h^+ \longrightarrow 4H^+ + O_2$ $\quad (E^0 = 1.23\ \text{V vs. RHE})$ (1)

HER: $4H^+ + 4e^- \longrightarrow 2H_2$ $\quad (E^0 = 0.00\ \text{V vs. RHE})$ (2)

Alkaline condition:

OER: $4OH^- + 4h^+ \longrightarrow 2H_2O + O_2$ $\quad (E^0 = 1.23\ \text{V vs. RHE})$ (3)

HER: $4H_2O + 4e^- \longrightarrow 2H_2 + 4OH^-$ $\quad (E^0 = 0.00\ \text{V vs. RHE})$ (4)

Overall water splitting

$2H_2O \longrightarrow 2H_2 + O_2$ $\quad (\Delta E^0 = 1.23\ \text{V vs. RHE} \Longrightarrow \Delta G = 237\ \text{kJ mol}^{-1})$ (5)

Here, E^0 is the equilibrium potential of the half-reaction expressed with respect to the reversible hydrogen electrode (RHE). According to equations (1) to (4), hydrogen and oxygen molecules are produced by 2-electron and 4-electron transfer reactions, respectively. Therefore, OER is the rate-limiting step for overall water splitting − from a kinetic and thermodynamic

perspective – due to the challenging four-electron transfer process.[25] Furthermore, water splitting is a non-spontaneous reaction involving a free energy change of $\Delta G = 237.2\ \mathrm{kJ\ mol^{-1}}$, corresponding to an electrochemical potential of $+1.23\ \mathrm{V}$ per electron. Therefore, the cleavage of the water molecule only occurs by applying a potential difference of at least $+1.23\ \mathrm{V}$ between photogenerated holes and electrons. However, this required potential difference is higher in practice due to additional overpotentials to overcome the kinetic barriers of redox reactions, in addition to ohmic losses.[18] As discussed below, such energy input, in theory, can be provided by sunlight if the semiconductor produces electron-hole pairs by absorbing photons with energy equal to or higher than the water splitting thermodynamic voltage plus the overpotentials.

Historically, the first demonstration of PEC water splitting was carried out by Honda and Fushijima in 1972, where they employed a TiO_2 photoanode for OER electrically coupled with a platinum counter electrode for HER, producing oxygen and hydrogen gases under ultraviolet radiation and external bias (Figure 2a).[15] Since then, many advances have been made in developing PEC technologies and synthesizing more efficient semiconductor materials. To date, there are three main configurations of PEC water splitting devices (Figure 2), constructed by the following components: (a) n-type semiconductor as a photoanode for OER and metal counter electrode for HER, (b) p-type semiconductor as a photocathode for HER and metal counter electrode for OER, and (c) n-type semiconductor as a photoanode for OER and p-type semiconductor as a photocathode for HER (Tandem cell). It is noteworthy that more complex architectures involving hybrid combinations of photovoltaic and PEC systems are also being widely developed to produce green hydrogen driven by solar energy.[16,31]

Essentially, all PEC devices share a similar mechanism, described by three well-defined steps: (i) photogeneration of electron-hole pairs in the semiconductor by absorbing photons with energy $h\nu \geq E_G$, (ii) charge carrier migration to the semiconductor or metal surfaces, and (iii) occurrence of water redox reactions at the semiconductor/electrolyte or metal/electrolyte interface (see Figure 2).[12,32] Unfortunately, PEC systems typically suffer from severe recombination of electron-hole pairs (which can occur through radiative recombination, Auger recombination, and via impurities scattering[33]), significantly reducing the efficiency of the PEC device for producing chemical fuels. Indeed, suppressing these recombination processes has been the main challenge of all PEC technologies. Nevertheless, it is essential to note that the (i) electrodes responsible for OER and HER are spatially separated and connected by an electrical circuit; (ii) it is possible to apply an external bias that aids in the separation of charges

and compensates for the overpotentials and ohmic losses of the system; and (iii) the produced gases can be separated by placing an ion exchange membrane between the two electrodes.

Importantly, configurations (a) and (b) exhibit only one photo-absorber material (n and p-type semiconductor, respectively) responsible for the absorption of sunlight and generation of charge carriers. Furthermore, these configurations are characterized by the absorption of two photons (ideally) to produce a single H_2 molecule. As discussed in section 2.3, both PEC cells (a) and (b) typically require an external bias to increase the charge separation efficiency by enhancing a built-in electric field and compensating for overpotentials and other energy losses. In this context, the coupling of an n-type semiconductor (acting as a photoanode for OER) with a p-type semiconductor (photocathode for HER) in the so-called Tandem cells (Figure 2c) emerges as a promising pathway for producing green hydrogen using only water, sunlight, and semiconductors. As shown in section 2.4, although it is necessary to absorb four photons to produce an H_2 molecule, Tandem cells provide free energy ($\Delta\mu_{ex}$) – powered only by sunlight – typically higher than the thermodynamic voltage of water splitting plus overpotentials.

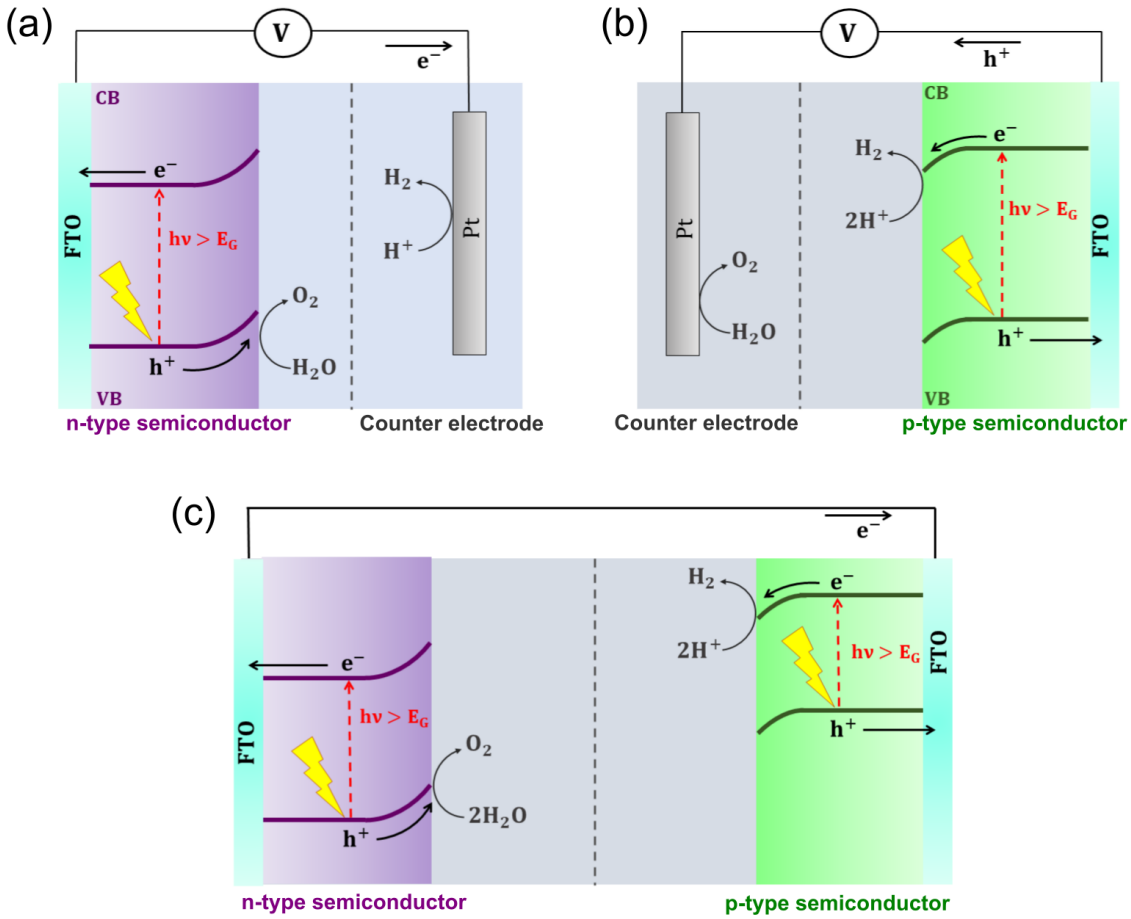

Figure 2 – Simplified energy diagram of PEC devices under operation. Single-absorber PEC cell composed of (a) a photoanode and a metallic counter electrode, (b) a photocathode and a metallic counter electrode. (c) Typical PEC Tandem cell composed of a photocathode externally coupled with a photoanode. Note that the photogenerated charges that migrate to the conductive substrate F-doped tin oxide (FTO) are conducted by the external circuit to the other component of the cell.
Source: By the author.

To understand the physics involved in PEC cells for producing H_2 from semiconductors, water, and sunlight, we will briefly discuss the fundamentals of semiconductors, the semiconductor/electrolyte interface under dark, applied bias, and illumination, and finally, the mechanism behind the single-absorber and Tandem cells configurations.

2.2 Physics behind PEC water splitting

2.2.1 Fundamentals of semiconductors

Understanding the physical properties of semiconductor materials is of fundamental importance for developing more efficient PEC systems. According to the classical band theory, crystalline solids can be classified into metals, insulators, and semiconductors.[34] Specifically,

the VB overlaps with the CB for metals, so the electrons can be freely excited to higher energies, efficiently conducting electricity. In contrast, for insulators (at 0 K), the VB is completely filled by electrons, thereby requiring the excitation of electrons from the VB to the CB for conducting electricity. However, the insulator bandgap is typically higher than ~4 eV, showing extremely low conduction at room temperature. In this context, a semiconductor is essentially a band insulator with a smaller bandgap (< 4 eV), thereby allowing the thermal excitation of some electrons even at room temperature and exhibiting higher conductivity as the temperature increases. Besides that, electrons can be excited from the VB to the CB of the semiconductor upon absorption of electromagnetic radiation (as long as the photon energy is higher than the E_G), thus producing electron-hole pairs that play a fundamental role in PEC applications.

In general, the probability of electron occupancy over available energy levels in a solid is defined by the Fermi-Dirac distribution function[18,34]:

$$f(E) = \frac{1}{1 + \exp\left(\frac{E - E_F}{k_b T}\right)}, \tag{6}$$

where E_F is the Fermi energy, k_b is the Boltzmann constant, and T is the temperature (in Kelvin). Therefore, the Fermi energy is defined as the energy level at which the probability of occupation by one electron is $f(E_F) = 1/2$. According to equation (6), this probability rapidly increases to 1 for $E < E_F$ and decreases to 0 for $E > E_F$, over a range of $\sim k_b T$, respectively. Initially assuming a semiconductor without impurities (intrinsic), the electrons in its VB can be thermally excited to the CB, leaving holes in the VB. The concentrations of n electrons and p holes, which must be equal in this situation, can be expressed in terms of the Fermi-Dirac function for the presence (f) or absence $(1 - f)$ of electrons, respectively. That is:

$$n = \int_{E_C}^{\infty} D_C(E) f(E) dE, \tag{7}$$

$$p = \int_{-\infty}^{E_V} D_V(E)[1 - f(E)] dE, \tag{8}$$

where D_C and D_V are the densities of states (DOS) for electrons in the CB and holes in the VB, respectively. In general, DOS distributions are complicated energy functions, but close to the band edges (which approach parabolic shapes), electrons and holes can be considered quasi-free, with effective masses (m_e^* and m_h^*) defined by the curvature of the band edges. It is straightforward to show that[35]:

$$D_C(E \geq E_C) = \frac{(2m_e^*)^{\frac{3}{2}}}{2\pi^2 \hbar^3} \sqrt{E - E_C}, \tag{9}$$

$$D_V(E \leq E_V) = \frac{(2m_h^*)^{\frac{3}{2}}}{2\pi^2\hbar^3}\sqrt{E_V - E}, \tag{10}$$

where $\hbar$ is the reduced Planck constant. Assuming non-degenerate semiconductors, i. e., with a low concentration of electrons and holes, where $E - E_F \gg k_bT$, the Fermi-Dirac distribution can replaced by the Boltzmann distribution: $\exp[-(\mathrm{E} - \mathrm{E_F})/\mathrm{k_b T}]$. From equations (7) and (8):

$$n(T) = N_C \exp\left[-\frac{(E_C - E_F)}{k_bT}\right], \qquad N_C = \frac{2(2\pi m_e^* k_b T)^{\frac{3}{2}}}{h^3} \tag{11}$$

$$p(T) = N_V \exp\left[\frac{(E_V - E_F)}{k_bT}\right], \qquad N_V = \frac{2(2\pi m_h^* k_b T)^{\frac{3}{2}}}{h^3} \tag{12}$$

where N_C and N_V are the effective DOS in the conduction and valence bands. These equations are general and hold for intrinsic and extrinsic semiconductors (defined below). For intrinsic semiconductors, $n = p$, and therefore:

$$E_F = \frac{E_C + E_V}{2} + \frac{k_bT}{2}\ln\left(\frac{N_V}{N_C}\right), \tag{13}$$

which shows that at temperature $T = 0\ K$, the Fermi energy is located precisely in the center of the midgap. Furthermore, the intrinsic charge density in the semiconductor (n_i) is determined by the mass balance equation (equation 14), [34-35] which shows that the concentration of electrons and holes in an intrinsic semiconductor increases rapidly with temperature.

$$np = N_C N_V \exp\left(-\frac{E_G}{k_bT}\right) = \sqrt{n_i}. \tag{14}$$

In practical terms, intrinsic semiconductors are materials with low conductivity and extremely difficult to synthesize. For PEC applications, semiconductors typically have electron-donating or electron-accepting impurities (n and p- type doping, respectively), which influence the conduction properties of these compounds. Specifically, in *n*-type semiconductors, the donor impurities have a higher number of valence electrons than the host atom and introduce occupied energy levels near E_C; therefore, the additional electrons can easily be promoted to the CB (Figure 3), contributing to conduction.[12,35-36] In contrast, in p-type semiconductors, the acceptor impurities have fewer valence electrons than the host atom and introduce vacant energy levels of electrons near the E_V; in this case, the VB electrons are easily transferred to the impurities, leaving holes in the semiconductor that contribute to conductivity.

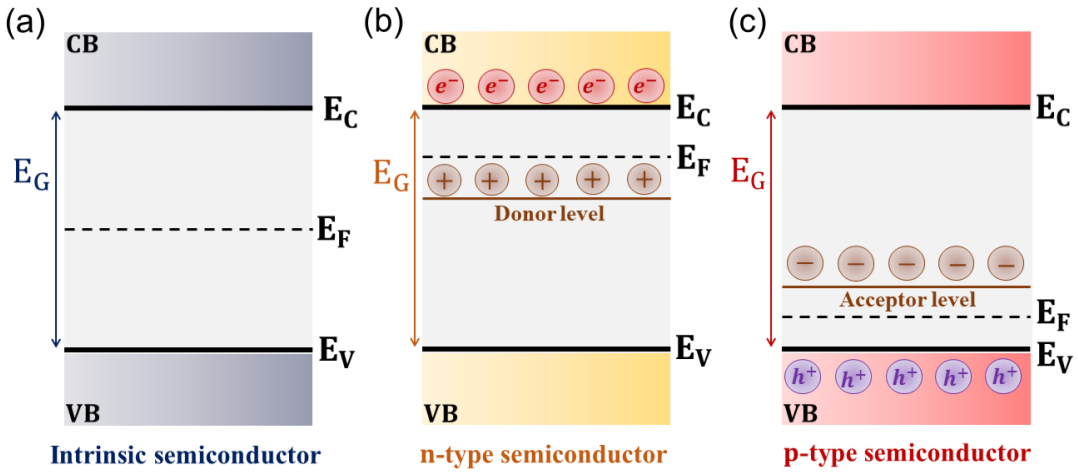

Figure 3 – Simplified band diagram of (a) an intrinsic semiconductor and extrinsic semiconductors of (b) n-type and (c) p-type nature. Note that the electrons and holes sketched in this figure refer only to those departing from impurity sites. In addition to these charges, electrons are excited from the VB to the CB when subjected to sufficient temperature or illumination to overcome the energy gap.
Source: By the author.

In the presence of impurities, semiconductors exhibit excess electrons or holes, giving rise to minority and majority charge carriers. Therefore, in $n(p)$-type semiconductors, electrons (holes) are the majority charge carriers. Due to this disturbance in the population of electrons and holes, the Fermi level of doped semiconductors is not in the middle of the gap. Assuming that all the concentration of electrons and holes comes from the impurities, that is, $n \approx N_D$ and $p \approx N_A$, where N_D and N_A represent the concentrations of donor and acceptor impurities, respectively, one finds using equations (11) and (12):

$$E_F = E_C - k_b T \ln\left(\frac{N_C}{N_D}\right), \tag{15}$$

$$E_F = E_V + k_b T \ln\left(\frac{N_V}{N_A}\right). \tag{16}$$

Therefore, the Fermi energy must be located close to the CB (VB) edge for the n-type (p-type) semiconductor. Furthermore, when the CB (VB) of the *n*-type (*p*-type) semiconductor has a concentration of electrons (holes) equal to N_C (N_V), the Fermi energy is located precisely at E_C (E_V). The possibility of doping semiconductors, originating minority and majority charge carriers, is of fundamental importance for PEC technologies since *n*-type and *p*-type semiconductors in contact with an electrolyte (subject of the following sections), act as photoanodes and photocathodes, respectively, capable of for the production of O_2 and H_2 gases.

2.2.2 Semiconductor/electrolyte interface under dark

When a semiconductor contacts an electrolyte with electrochemical potential $\mu \neq E_F$ under dark condition, a charge transfer between the two phases immediately occurs to ensure electronic neutrality in the system, thereby originating a semiconductor/liquid junction (SCLJ). Precisely, electronic equilibrium is only achieved when the electrochemical potentials of the two phases are equal.[12,18] As shown in the previous section, the Fermi level in semiconductors (electrochemical potential for the solid) is totally determined by the positions of the band edges and the concentration of electrons and holes. In contrast, the electrolyte is not a conductive electronic phase; according to the Marcus-Gerischer theory,[37-38] electrons in aqueous solutions are located in energy levels of Gaussian character. Thus, the electrochemical potential in aqueous solutions has been derived from the condition that the density of oxidized (D_{ox}) and reduced (D_{red}) species states are equal, defining the redox energy E_{redox} of the electrolyte. Therefore, electronic equilibrium at the SCLJ occurs when the Fermi level of the semiconductor aligns with the redox energy level of the aqueous solution.

For an *n*-type semiconductor in contact with an electrolyte, the Fermi level is typically higher than the redox energy of the electrolyte (Figure 4a). In this case, electrons are diffused from the semiconductor to the electrolyte, leaving behind positive ionized donor states and moving the Fermi level towards E_{redox}. After aligning the electrochemical potentials, a space charge layer (SCL) with depletion length W of around 100 to 1000 Å appears within the semiconductor (Figure 4b). This SCL is characterized by the upward band bending and the production of a built-in electric field (gradient of the built-in potential Ψ_{bi}) that points from the semiconductor (positively charged) to the electrolyte (negatively charged). Since the SCR is where the majority charge carriers (electrons) are depleted from the semiconductor, this region is also known as the depletion layer. Similarly, for a *p*-type semiconductor, the Fermi energy is typically lower than the redox energy level, so electronic equilibrium is achieved by diffusing electrons from the solution to the semiconductor. In this case, a negative charge appears in the SCR (negative ionized acceptor states), causing a downward band bending and a built-in electric field that points from the electrolyte to the semiconductor.

In PEC systems, the dark (equilibrium) condition is disturbed by applying electric energy and illumination, whose influences on the SCLJ properties will be discussed below.

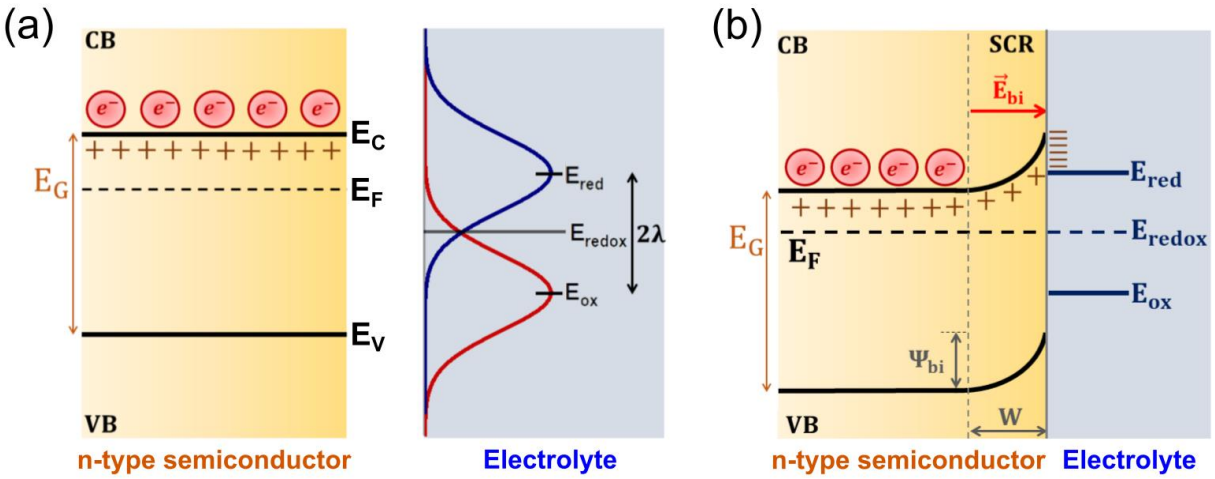

Figure 4 – Development of an SCLJ between an n-type semiconductor and an electrolyte with electrochemical potential E_{redox}. (a) Isolated band diagrams of the semiconductor and the electrolyte, and (b) band diagram at equilibrium (dark condition). Here λ is the reorganization energy[12], defining the separation between the peaks of the Gaussian redox distributions.
Source: By the author.

2.2.3 Semiconductor/electrolyte interface under applied bias

When a semiconductor in contact with an electrolyte receives an external potential (E_{app}), the Fermi energy of the solid (initially aligned with E_{redox}) tends to move towards equilibrium with E_{app}. If the semiconductor has a negligible amount of surface states, its CB and VB edges at the SCJL are unaffected by the bias application (band edge pinning). In contrast, energy bands at the bulk move together with E_F, thereby modulating the band bending intensity and orientation within the SCR. Figure 5a shows a typical *n*-type semiconductor in contact with an electrolyte under dark conditions. When applying a potential bias in this dark configuration (Figure 5a), three different situations need to be analyzed[18,39]:

(i) when $E_{app} = E_{FB}$, where E_{FB} is the flat band potential, there is no formation of an SCR (and, therefore, no built-in electric field) in the semiconductor; that is, the energy bands become flat (Figure 5b), and no charge transfer occurs at the electrolyte/semiconductor interface;

(ii) when $E_{app} > E_{FB}$ (reverse bias), the Fermi energy of the semiconductor moves downwards in relation to E_{redox}, giving rise to a depletion layer characterized by the upward band bending and a built-in electric field pointing from the semiconductor to the electrolyte (Figure 5c);

(iii) when $E_{app} < E_{FB}$ (forward bias), there is an excess of majority charge carriers (electrons) in the SCR, giving rise to an accumulation layer characterized by the downward band bending and a built-in electric field pointing from the electrolyte to the semiconductor (Figure 5d).

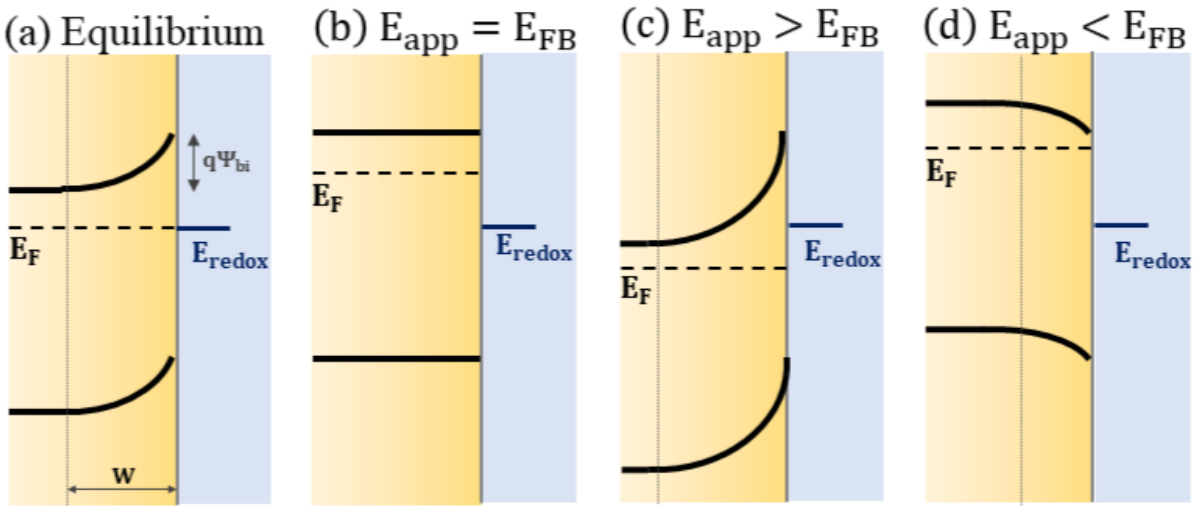

Figure 5 – Effect of varying the applied potential on a junction between an n-type semiconductor and an electrolyte in the dark. (a) Equilibrium situation ($E_{app} = 0$), (b) absence of SCR when $E_{app} = E_{FB}$, (c) formation of depletion layer ($E_{app} > E_{FB}$), and (d) development of an accumulation layer for $E_{app} < E_{FB}$.
Source: Adapted from GIMÉNEZ *et al.*[18]

A similar analysis for *p*-type semiconductors reveals a depletion layer for $E < E_{FB}$ and an accumulation layer for $E > E_{FB}$. The charge transfer properties at the SCLJ depend on the presence of a depletion or accumulation layer. Specifically, when there is an accumulation layer, the semiconductor behaves as a metallic electrode because there is an excess of majority charge carriers for charge transfer (in this case, the n-type semiconductor acts like a metallic cathode, and the p-type semiconductor behaves like a metallic anode).[18,39] In contrast, if there is a depletion layer under dark conditions, few charges are available for charge transfer, and the redox reactions are limited, resulting in low current densities. However, as discussed in the following section, electron-hole pairs are produced when a semiconductor is exposed to electromagnetic radiation with sufficient energy ($E > E_G$), thereby allowing minority charge carriers to engage in redox reactions and produce photocurrents under reverse bias.

2.2.4 Semiconductor/electrolyte interface under illumination

When the semiconductor electrode absorbs photons with energy $E > E_G$, electrons are promoted from its VB to the CB, originating electron-hole pairs. These charge carriers typically recombine when generated in the bulk (interior) of the semiconductor. However, if the electron-hole pairs are generated within (or very close to) the SCR, the built-in electric field in this region causes efficient charge separation, suppressing their recombination. Therefore, the increase in electron and hole density due to light absorption considerably disturbs the electron and hole

concentrations from their dark values, so they can no longer be described as a single Fermi energy. In this case, the concept of Fermi level splitting into quasi-Fermi levels (QFL) for electrons (E_{Fn}) and holes (E_{Fp}) has been considered a powerful tool to describe the conduction properties of the system.[12,18] The quasi-Fermi levels are defined by the concentration of free charges carriers within the SCR, added with the concentration of photogenerated charges, i.e.:

$$n + \Delta n = N_C \exp\left[-\frac{(E_C - E_{Fn})}{k_b T}\right], \tag{17}$$

$$p + \Delta p = N_V \exp\left[\frac{(E_V - E_{Fp})}{k_b T}\right], \tag{18}$$

where Δn and Δp represent the concentration of photogenerated electrons and holes, respectively. Fundamentally, these quasi-equilibrium distributions are justified due to the fast thermalization (10^{-12} s) of the photogenerated charge carriers with the lattice phonons, allowing the distribution of electrons and holes over the eigenstates of their respective bands to be described by Fermi distributions, even though the CB and VB are not in equilibrium with respect to electron exchange[40] (that is, the generation and recombination events necessary for restoring equilibrium between the bands take much longer (~10^{-9} s) than the thermalization of charge carriers in their respective bands).

It is important to note that when the minority charges leave the surface to drive redox reactions, a negative (positive) charge is accumulated on the depletion region of the *n*-type (*p*-type) semiconductor, producing a photovoltage (V_{ph}) of a negative (positive) sign. As shown in Figure 6, this photovoltage works similarly to a forward bias, reducing the band bending due to the presence of photogenerated charges in the SCR (band flattening phenomena) and raising the QFL of electrons (i.e., $qV_{ph} = |E_{Fn} - E_{redox}|$) for n-type semiconductors.[12,18] Furthermore, illumination also influences the electrochemical potentials within the semiconductor by splitting the dark Fermi level into QFL for electrons and holes (Figure 6b).

Importantly, the separation between the QFL of electrons and holes at the SCJL interface, that is, $\Delta\mu_{ex} = (E_{Fn} - E_{Fp})_{\text{int}}$, represents the free energy stored in the electron-hole pairs.[40] This Helmholtz free energy ($\Delta\mu_{ex}$), quantifying the energy available to perform work, is given by the difference between the internal energy (E) and the product of temperature and entropy (S), that is, $\Delta\mu_{ex} = E - TS$. Therefore, the internal energy of the electron-hole pair, represented by the E_G, always suffers significant losses associated with entropy, releasing a useful energy $\Delta\mu_{ex}$ always less than E_G. Furthermore, PEC systems typically exhibit slow water oxidation kinetics (i.e., E_{Fp} approaches E_V) so that the variations of electrostatic nature (given

by qV_{ph}) and electrochemical nature ($\Delta\mu_{ex}$) are never equal.[41-42] In this context, the difference between the free energy and photovoltage defines the so-called photoelectrochemical affinity (a_{ph}), i.e., $a_{ph} = \Delta\mu_{ex} - qV_{ph}$. According to the non-equilibrium thermodynamics, a_{ph} is connected to entropic losses caused by the irreversible hole transfer process between the VB and the electrolyte and can be associated with a driving force for producing photocurrents.[41-42]

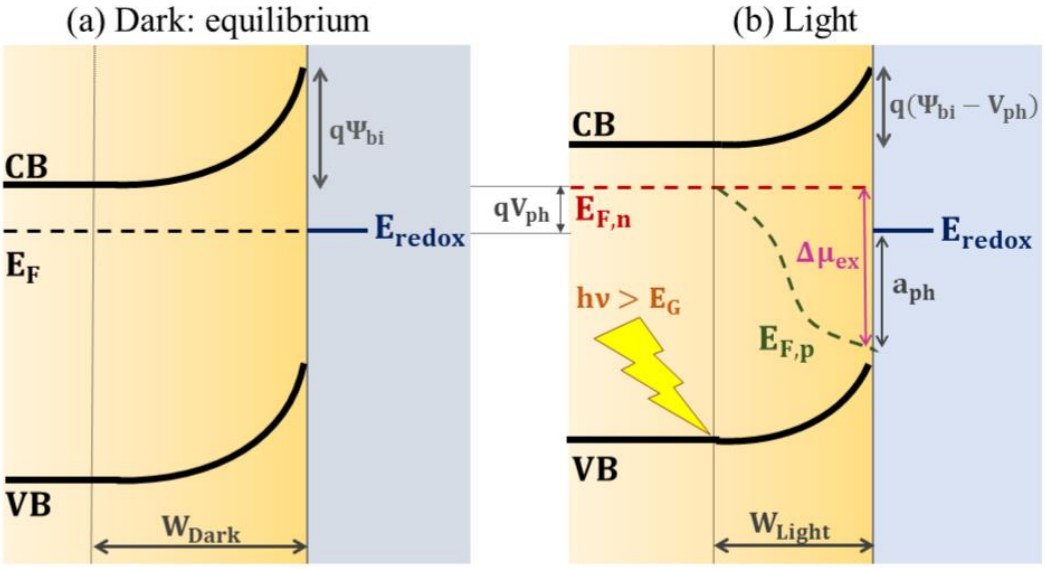

Figure 6 – Energy band diagram of an n-type semiconductor acting as photoanode in contact with an aqueous electrolyte solution (a) at equilibrium in the dark and (b) under illumination. W_{Dark} and W_{Light} refer to the depletion length under dark and illumination conditions, respectively. Note that $W_{Dark} > W_{Light}$.
Source: Adapted from MIAO *et al.*[42]

As a result, the QFL plays an essential role in describing electron transfer processes at the SCLJ since their relative position compared to the redox potentials are responsible for producing charge carriers capable of driving redox reactions. In the particular case of water splitting, the positions of the QFL for electrons and holes at the SCLJ interface must straddle the water reduction and oxidation potentials, respectively, for the production of H_2 and O_2 without applied bias.[18,41] In other words, the free energy $\Delta\mu_{ex}$ generated by the semiconductor must be higher than the water splitting thermodynamic voltage (1.23 V) plus kinetic overpotentials and ohmic losses. In essence, the key objective of any PEC device is to convert the largest possible fraction of the available energy $\Delta\mu_{ex}$ into storable chemical fuels (e.g., green hydrogen). Another crucial advantage of employing the QFL concept refers to the fact that their gradients are the fundamental driving forces for producing currents (electron and hole flow), that is[40]:

$$j = j_n + j_p = n\mu_n \nabla E_{Fn} + p\mu_p \nabla E_{Fp}, \quad (19)$$

where j is the total current, $j_{n(p)}$ is the partial current associated with the flow of electrons (holes), n and p are the concentrations of electrons and holes, and μ_n and μ_p their respective mobilities. In the equilibrium condition, where E_{Fp} = E_{Fn} = constant, equation (19) shows no driving forces for redox reactions, resulting in a net zero charge flows across the SCJL ($j = 0$). In theory, since the electrochemical potential can be decoupled into chemical and electrical components, it is possible to define currents associated with the chemical potential gradient (diffusion currents) and the electric potential gradient (drift current associated with the built-in electrical field).[40] However, diffusion and drift currents do not exist separately; the experiments only provide the total j current, which is solely associated with the gradients of the QFLs.

As a last consequence of applying illumination on semiconductors immersed in aqueous solutions, we see that *n*-type semiconductors behave as photoanodes because their built-in electric field accelerates photogenerated holes towards the electrolyte to drive the OER (whereas the photogenerated electrons are directed to the back contact). In contrast, p-type semiconductors act like photocathodes because their built-in electric field directs photogenerated electrons to reduce species in the electrolyte (while the holes are accelerated towards the back contact). From the knowledge of the semiconductor/electrolyte interface under dark, applied bias, and illumination, it becomes straightforward to understand the mechanisms behind the single-absorber and Tandem cell configurations for producing green hydrogen from water, sunlight, and semiconductor materials.

2.3 Single-absorber PEC cell

Single-absorber PEC cells are typically composed of an *n*-type semiconductor (photoanode) electrically connected to a Pt cathode (responsible for HER), in a two-electrode configuration under zero bias. In the dark (Figure 7a), the Fermi energies of the semiconductor and the metal (externally connected) must align to a value close to E_{redox}, ensuring net zero charge flow. However, the electrolyte has two redox pairs, characterized by energy levels E^0 (H_2O/O_2) and E^0 (H^+/H_2). Therefore, at equilibrium, the electrochemical potential of the solid and liquid phases must line up somewhere between the redox energies of the electrolyte; its precise position will depend on the relative concentrations of the species present in the solution.[12] Under illumination (Figure 7b), the semiconductor absorbs electromagnetic radiation with $E > E_G$, producing electron-hole pairs and developing a photovoltage V_{ph}, which increases its dark Fermi energy and reduces band bending. Furthermore, illumination causes

the splitting of the dark Fermi energy into QFL for electrons and holes, producing the free energy $\Delta\mu_{ex}$. Note that V_{ph} also raises the E_F of the counter electrode.

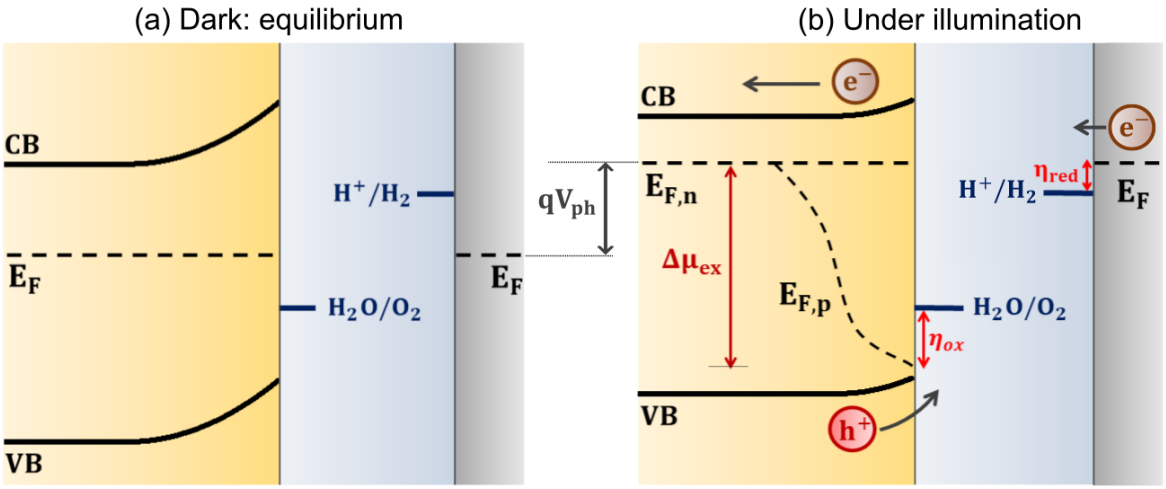

Figure 7 – Energy band diagram for a single photoabsorber PEC cell based on an n-type semiconducting photoanode that is electrically coupled to a metal counter electrode (a) at equilibrium in the dark and (b) under illumination.
Source: Adapted from KROL *et al.*[12]

In this single-absorber configuration, the semiconductor photoelectrode must supply sufficient free energy ($\Delta\mu_{ex}$) to overcome the water splitting thermodynamic voltage ($1.23\ V$), the kinetic overpotentials (η_{ox} and η_{red}), and ohmic energy losses to perform overall water splitting without applying bias. As a result, the QFLs must straddle the water reduction and oxidation potentials so that the photogenerated electrons have energy lower than $E^0(H^+/H_2) = 0$ eV and holes with energy higher than $E^0\ (H_2O/O_2) = 1.23$ eV. However, semiconductors that meet this requirement have a wide bandgap that restricts visible light absorption or are unstable in aqueous solutions. Therefore, single-absorber systems typically require applying a (reverse) bias between the photoelectrode and the metal counter electrode to increase the band bending (i.e., the built-in electric field intensity) in the SCR and also to compensate for unfavorable thermodynamic locations of the QFLs in relation to the OER and HER potentials.

Nevertheless, as the main purpose of every PEC system is to produce green H_2 from only water and sunlight, without external bias, single-absorber systems are typically employed to develop more efficient photoelectrodes for Tandem systems (see next section). These investigations are typically performed with a three-electrode configuration composed of the photoelectrode working electrode (WE), counter electrode (CE), and a reference electrode (e.g., reversible hydrogen electrode, RHE). In the three-electrode configuration, the potential difference between WE and RE is fixed by varying the current between the WE and CE.

Therefore, the CE does not need to be illuminated and can have a larger surface area than the WE, ensuring that the overpotentials are almost negligible on the CE surface.[12,32] Therefore, this configuration allows distinguishing the WE catalysis from the reactions on the CE, being ideal for characterizing the PEC performance of photoanodes and photocathodes, separately.

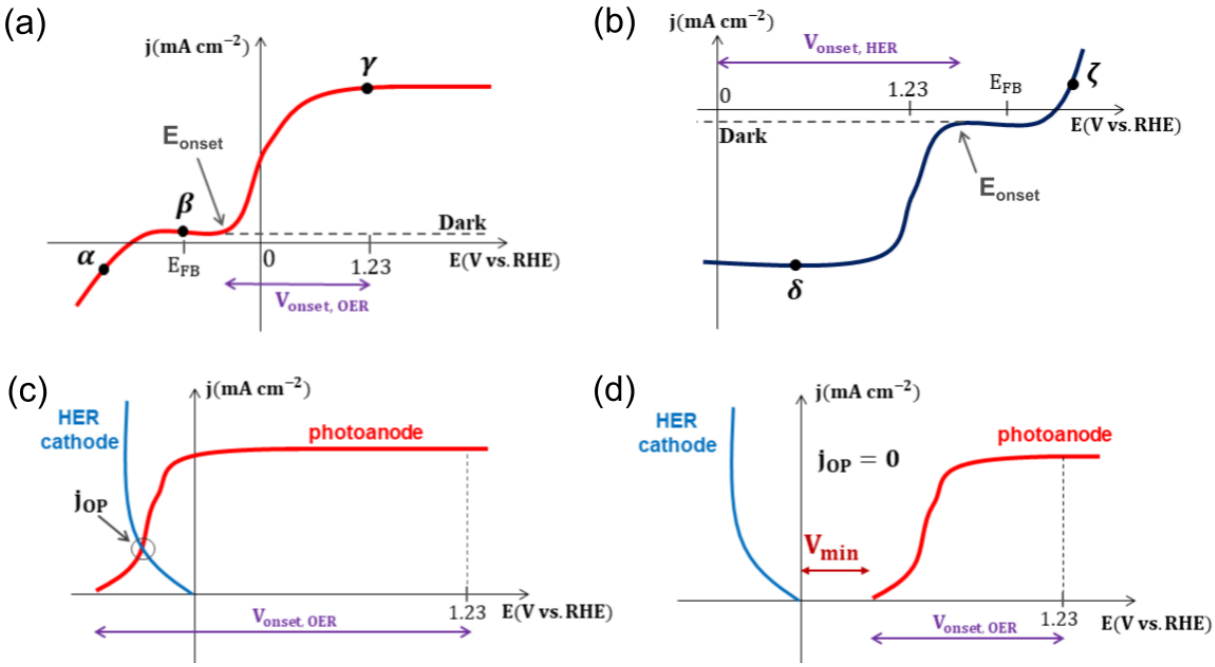

Figure 8 – (a) Typical photocurrent density response as a function of applied potential (j-V curves) for (a) an n-type semiconducting photoanode and (b) p-type semiconducting photocathode, and overlap of typical j-V curves for a photoanode and a metal cathode, exhibiting (a) $J_{OP} \neq 0$ and (b) $J_{OP} = 0$.
Source: Adapted from CHEN *et al.*[32]

Figure 8a shows the current density response (under dark and illumination) as a function of the applied potential (j-V curves) in the three-electrode configuration for a *n*-type photoanode. When illuminated with energy $E > E_G$, the photogenerated holes perform OER at the SCLJ, while electrons migrate to the CE to drive HER. The potential at which this process begins is defined by E_{onset}, displaced from the flat band potential (E_{FB}) by the water oxidation overpotential. When the applied potential is E_{FB} (point β), there is no current in the dark and light since there is no SCR to separate the charges. In potentials more negative than E_{FB} (point α), the semiconductor acts like a metallic cathode (producing cathodic current), in light and dark, due to the formation of an accumulation layer. In contrast, a depletion layer appears for $E_{app} > E_{FB}$ (point γ), limiting charge flow in the dark but causing high oxidative photocurrents under illumination (since the built-in electric field drives the photoholes for OER). A similar analysis (Figure 6b) shows that a *p*-type semiconductor acts as an anode for applied potential more positive than E_{FB} (point δ) and as a photocathode for $E_{app} < E_{onset}$ (point ζ).

Furthermore, the difference between the redox potential E^0 and the onset potential (E_{onset}) provides the underpotential (V_{onset}) for photocurrent onset relative to HER or OER.[32] Determining underpotentials with the three-electrode configuration is a powerful tool for analyzing the ability of photoelectrodes in bias-unassisted water splitting. Figure 8c shows the j-V curve of a typical photoanode with a large V_{onset}, superimposed with the current (with flipped sign) of a CE for HER. From these two curves, it is possible to extract the maximum operating photocurrent (j_{OP}) that would be measured in a two-electrode configuration with zero bias (i.e., j_{OP} is the short-circuit current). As the complete device must sustain the same current in the photoanode and cathode (electronic neutrality in the system), the intersection between the two curves represents the theoretical j_{OP}.[18,32] Therefore, the photoanode of Figure 8c can produce a V_{onset} sufficient to overlap with the CE current ($j_{OP} > 0$), and the system can spontaneously perform water splitting. In contrast, the photoanode in Figure 8d cannot produce enough V_{onset} to overlap with the CE, requiring a potential bias V_{min} to drive the water splitting. A similar analysis also applies to photocathodes coupled with CE for OER.

Fundamentally, the most important efficiency metric for PEC systems is the solar-to-hydrogen (η_{STH}) conversion efficiency, defined as the ratio between the chemical energy of the hydrogen produced and the solar energy input on the system.[12,32] The chemical energy of H_2 is calculated from the rate of hydrogen production (mmol H_2/s) multiplied by the change in Gibbs free energy per mole ($\Delta G = 237$ kJ mol^{-1}, at room temperature). The solar energy input on the system is determined by the total power density $P(\mathrm{mW\,cm^{-2}})$ multiplied by the illuminated area ($\mathrm{cm^2}$). That is:

$$\eta_{STH} = \left[\frac{(\text{mmol } H_2/\text{s}) \times (237 \text{ kJ mol}^{-1})}{P(\mathrm{mW\,cm^{-2}}) \times \text{area}(\mathrm{cm^2})}\right]_{\text{AM 1.5G}} \tag{20}$$

Equation 20 calculates the power input (energy/time) of the numerator based on direct detection of H_2 production (through gas chromatography, for example). However, by assuming that the photogenerated electrons carry out the water reduction reactions, it is possible to express this power input in terms of voltage and current[18,32]:

$$\eta_{STH} = \frac{j_{op}(\mathrm{mA\,cm^{-2}}) \times 1.23(\mathrm{V}) \times \mathrm{FE}}{P(\mathrm{mW\,cm^{-2}})} \tag{21}$$

where FE is the faradaic efficiency (percentage of electrons consumed for hydrogen conversion), j_{op} is the measured operating current in the two-electrode configuration under zero bias, and 1.23 V is the thermodynamic water splitting potential. Importantly, the determination of FE is crucial for calculating η_{STH}, as the faradaic efficiency is typically less than 100%. That

is, a fraction of the photogenerated electrons cannot drive the reduction of water into hydrogen, being lost during corrosive processes, recombination, or other surface reactions.

Interestingly, a maximum value of $\eta_{STH} = 11.6\%$ has been predicted for unbiased water splitting employing a single-absorber material with a bandgap of $E_G = 2.2$ eV.[20] However, the η_{STH} efficiencies of PEC water splitting with a single semiconductor are still far from reaching values higher than 10% (considered the benchmark for practical applications). In this regard, developing Tandem cells has been considered a promising strategy to overcome the difficulties of a single-absorber configuration, producing enough $\Delta\mu_{ex}$ to drive spontaneous (bias-unassisted) water splitting without sacrificing efficient visible light absorption.

2.4 Tandem PEC cells

Tandem cells emerge as promising PEC devices for developing enough free energy $\Delta\mu_{ex}$ to produce green H_2 while exploiting efficient solar photon harvesting.[16–18] In general, Tandem cells combine an *n*-type semiconductor with a *p*-type semiconductor in a two-electrode arrangement. Upon illumination, each photoelectrode develops a free energy $\Delta\mu_{ex,i}$ $(i = n, p)$ defined as the difference between the QFLs of electrons and holes at the SCLJ. As a result, photogenerated holes in the photoanode are driven toward the electrolyte to perform the OER. The corresponding electrons migrate to the external circuit, recombining with the holes of the photocathode. In contrast, electrons at the photocathode flow into the electrolyte to drive the HER (Figure 9). Therefore, the following conditions must be meet for spontaneous overall water splitting using Tandem cells: (i) $E_{Fp} > E^0(H_2O/O_2)$, (ii) $E_{Fn} < E^0(H_2O/H_2)$, and (iii) $E_{C1} < E_{V2}$ (subscript 1 and 2 referring to the photoanode and photocathode, respectively).

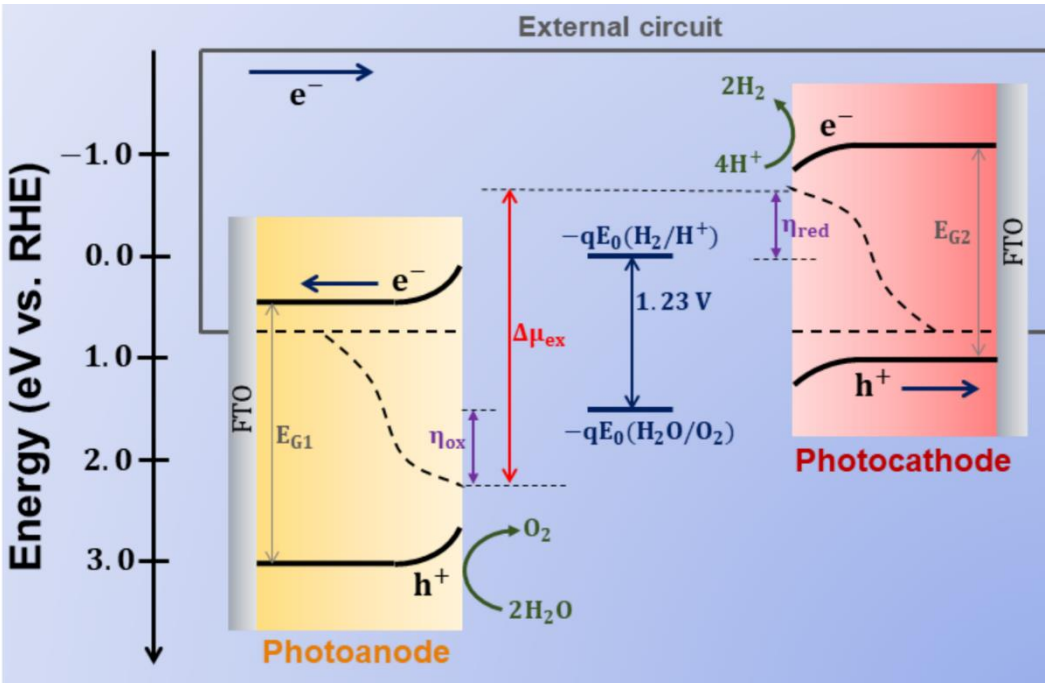

Figure 9 – Energy band diagram for a PEC Tandem cell based on an n-type semiconducting photoanode that is electrically coupled to a p-type semiconducting photocathode under operation conditions.
Source: Adapted from PRÉVOT *et al.*[16]

These requirements allow for semiconductors with narrower bandgaps since just one band edge position is constrained for each photoelectrode. Furthermore, note that the free energies of the photocathodes and photoanodes add up, i.e., $\Delta\mu_{ex} = \sum_i \Delta\mu_{ex,i}$. Thus, the condition $\Delta\mu_{ex} \geq 1.23\ eV + \eta_{ox} + \eta_{red} = \Delta\mu_{ex}^{min}$ necessary for bias-unassisted water splitting is significantly easier to achieve when compared to the single-absorber approach.[16,18]

Furthermore, to optimize the absorption of sunlight, the photoanode (bandgap E_{G1}) is typically placed in front of the photocathode (bandgap E_{G2}), where $E_{G1} > E_{G2}$, allowing photons to be collected successively by each semiconductor.[16–18] In this stacked configuration, photons with wavelengths smaller than $\lambda_1 = hc/E_{G1}$ are absorbed by the photoanode, whereas the remaining photons (disregarding reflections and scatterings) are transmitted to and absorbed by the photocathode. Figure 10a compares the photon harvesting efficiency (considering AM 1.5G illumination) between the Tandem cell and single-absorber approaches. While a semiconductor suitable for the latter method currently has a bandgap of ~3.2 eV (e.g., $SrTiO_3$ and TiO_2) and absorbs only photons with $\lambda < 387$ nm, a typical tandem configuration with $E_{G1} = 2.2$ eV and $E_{G2} = 1.4$ eV exploits an astonishing larger photon range ($\lambda < 885\ nm$). Importantly, semiconductors can also be placed side-by-side; however, photon harvesting is significantly less efficient in this configuration.

To understand the influence of semiconductor bandgaps and energy losses on the STH efficiency of the Tandem configuration, we will briefly address Bolton's method.[16,18-19,43] In this method, the free energy produced in each semiconductor is estimated to be $\Delta\mu_{ex,i} \approx 0.75E_{Gi}$, a typical value for real systems. Furthermore, all energy losses during PEC water splitting are included in the U_{loss} factor: $U_{loss} = \sum_i E_{G,i} + \eta_{red} + \eta_{ox} - \Delta\mu_{ex}$. Assuming that all photons are converted into photocurrents, the total photocurrent generated at the photoanode (j_1) can be calculated by integrating the AM 1.5G spectrum in the relevant wavelength range (i.e., $\lambda \in [\lambda_0, hc/E_{G1}]$, $\lambda_0 \approx 300$ nm). Similarly, integration of the AM 1.5G spectrum for $\lambda \in [hc/E_{G1}, hc/E_{G2}]$ determines the HER photocurrent assuming that all remaining photons are absorbed in the photocathode. Therefore, the operational photocurrent (j_{OP}) flowing in the two-electrode configuration, which must be the same in the photoanode and photocathode, may be determined by the lowest value of j_1 and j_2. Thus, $j_{OP} = \text{Min}[j_1, j_2]$ if $\Delta\mu_{ex} > \Delta\mu_{ex}^{min}$ (required for spontaneous water splitting) and null otherwise. After determining j_{OP}, the corresponding STH efficiency as a function of E_{G1} and E_{G2} can be directly calculated from equation (21).

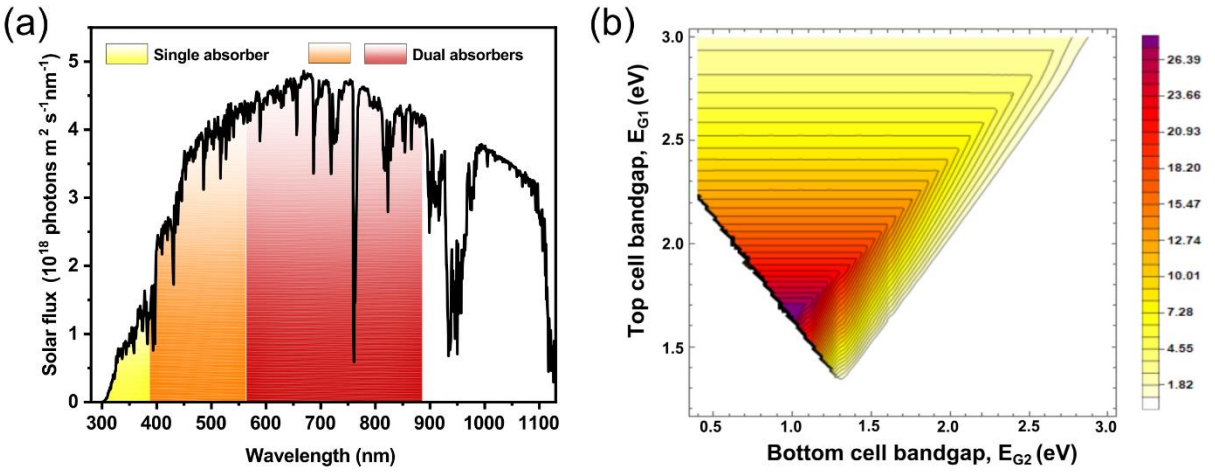

Figure 10 – (a) AM 1.5G solar photon flux as a function of wavelength. The shaded area of the spectrum represents the photos that could be harvested using a single absorber (yellow) and a Tandem approach (orange and red). (b) Contour plot (thick gray lines) showing the maximum predicted η_{STH} with AM 1.5G incident radiation and total energy loss (U_{loss}) set at 1.4 eV.
Source: Adapted from GIMÉNEZ *et al.*[18]

Figure 10b shows a contour plot of Bolton's method, giving the maximum value of η_{STH} as a function of E_{G1} and E_{G2}, assuming that $U_{loss} \approx 1.4$ eV. In this plot, the (triangular) shapes of the contours represent the values of E_{G1} and E_{G2} that develop the same STH efficiency. Note that η_{STH} is only defined for $E_{G1} > E_{G2}$, justifying the absence of contours in the upper left of the plot. Furthermore, the upper right zone also has $\eta_{STH} = 0$ since this region represents

combinations of E_{G1} and E_{G2} unable to produce enough free energy $\Delta\mu_{ex}$ for spontaneous water splitting given the assumed losses. Crucially, even considering significant energy losses in the Tandem cell ($U_{loss} = 1.4$ eV), the maximum value of STH efficiency occurs at 30% with $E_{G1} = 1.64$ eV and $E_{G2} = 0.99$ eV, which is a significant increase in relation to the single-absorber approach. Note also that higher STH values can be obtained for lower U_{loss}, showing that Tandem cells with low kinetic overpotentials and ohmic losses are very promising for producing green H_2 in a large scale.

In practical terms, the STH efficiency of Tandem cells can be determined by comparing the j-V curves of the individual semiconductors in a three-electrode configuration. Figure 11a shows a typical j-V curves for a photoanode (red curve) and a photocathode (blue curve) intersecting at a value $j_{OP}^{max} \neq 0$. Since the same current density must flow in the Tandem cell under operation, the value of j_{OP}^{max} represents the maximum value of the short-circuit current that would be measured in a two-electrode configuration (giving STH by equation (21)). Therefore, maximizing j_{OP}^{max} is the key challenge for Tandem technologies. Ideally, j_{OP}^{max} is maximized when the photoelectrodes have (i) onset for water oxidation (and reduction) at the most negative (positive) potentials possible, (ii) low kinetic overpotentials (i.e., $E_{onset} \approx E_{FB}$), (iii) and high photocurrent densities at low applied potentials.[16–18,32] It is important to note that due to ohmic losses and pH gradients in the aqueous solution, the actual value of j_{op} measured in the two-electrode configuration is always less than j_{OP}^{max}. Furthermore, similar to the single-absorber approach, the application of an external bias is necessary if the photoanode and photocathode *j-V* curves do not intersect (i.e., $\Delta\mu_{ex} < \Delta\mu_{ex}^{min} \Longrightarrow j_{OP}^{max} = 0$, see Figure 11b).

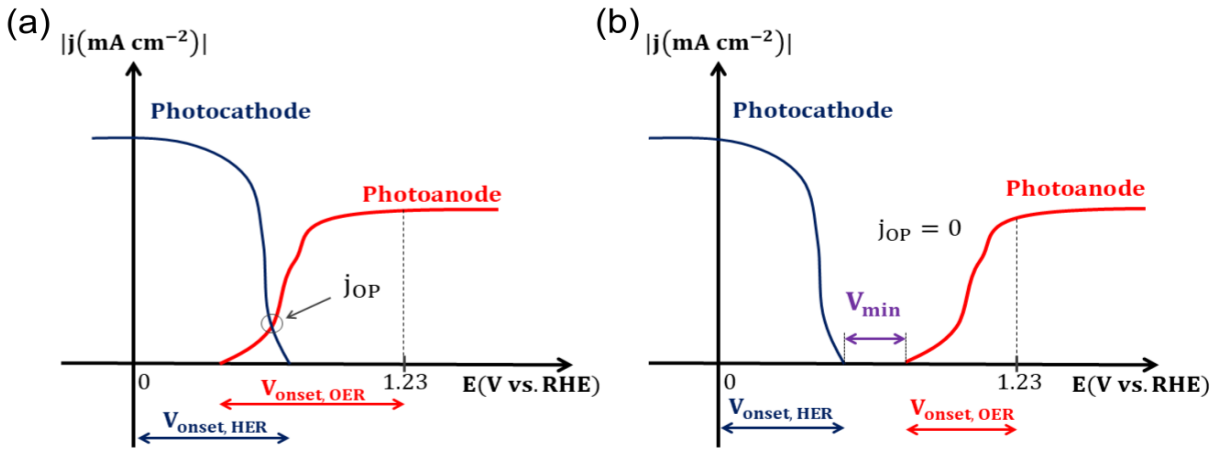

Figure 11 – overlap of typical j-V curves for an n-type semiconducting photoanode and a p-type semiconducting photocathode, exhibiting (a) $J_{OP} \neq 0$ and (b) $J_{OP} = 0$.

Source: Adapted from CHEN *et al.*[32]

Table 1 - Representative Metal Oxide-Based PEC Tandem Cells for bias-unassisted PEC Water Splitting.

Photoanode	Photocathode	Electrolyte	j_{OP}(mA cm^{-2})	STH (%)	Stability	Ref.
TiO_2	Cu−Ti−O	1 M KOH + 0.1 M Na_2HPO_4	0.25	0.30	350 s	44
W: $BiVO_4$/Co-Pi	$Cu_2O/ZnO/TiO_2/RuO_x$	0.5 M Na_2SO_4 + KPi +NaOH (pH 6)	0.71	0.87	5000 s	45
n-$BiVO_4$/Co-Pi	p-$BiVO_4$/Pt	0.1 M KPi (pH 7)	0.12	0.14	2 h	46
Mo-$BiVO_4$/TiO_2/ FeOOH	$Cu_2O/TiO_2/MoS_2$	0.1 M Na_2SO_4 (pH 6)	~0.065	– –	2900 s	47
$BiVO_4$	Pt–HfO_2/CdS/ HfO_2/Cu_2ZnSnS_4	Na_2HPO_4/NaH_2PO_4 (pH 6.5)	~2.5	~3.17	60 h	48
$CuWO_4$	$CuBi_2O_4$	0.1 M K_2HPO_4/K_3PO_4 (pH 11.66)	0.075	– –	0.75 h	49
$Fe_2O_3/NiFeO_x$	Si/Pt/TiO_2	0.5 M phosphate buffer (pH 11.8)	0.7	0.91	10h	50
$BiVO_4/NiFeO_x$-Bi	$(ZnSe)_{0.85}(CIGS)_{0.15}$ CdS /Ti/ Mo/Pt	0.5 M KBi (pH 9.5)	0.89	0.91	1800 s	51
Mo: $BiVO_4$/Co-Pi	p-Si/Pt	0.1 M KPi (pH 5.5)	0.46	0.57	3.5 h	52
ZnO/CdS	Cu_2O/Cu_2S	0.5 M Na_2SO_4	0.31	0.38	1h	53
$BiVO_4/CoO_x$/NiO	$(ZnSe)_{0.85}(CIGS)_{0.15}$ /CdS/In_2S_3/Ti/Mo/Pt	0.5 M KBi (pH 9.5)	~ 0.9	1.00	17 h	54
$BiVO_4/NiFeO_x$-Bi	$CuIn_{0.5}Ga_{0.5}Se_2$/CdS /Pt	0.5 M KBi (pH 9.5)	~ 3	3.7	3600 s	55
$BiVO_4$/FeOOH /NiOOH	CIGS/CdS/Al_2O_3/TiO_2 /Pt	1 M KBi (pH 9.2)	0.82	1.01	1800 s	56
Mo: $BiVO_4$/ $NiFeO_x$	$Cu_2O/Ga_2O_3/TiO_2$ /RuO_x	0.2 M KBi (pH 9.0)	2.4	3	12 h	57

Source: By the author.

Table 1 summarizes some representative research on semiconductor-based Tandem cells for bias-unassisted water splitting.[44–57] To date, the highest STH efficiency for these particular PEC devices is only 3.7% (obtained with the $BiVO_4/NiFeO_x$-Bi photoanode coupled with the $CuIn_{0.5}Ga_{0.5}Se_2$/Cds/Pt photocathode[55]), which is still far from meeting the requirements for practical applications. Precisely, the low STH efficiencies obtained so far are caused mainly by improper onset potentials and low photocurrent densities of the photoelectrodes.[12,17-18] Furthermore, the stability of PEC Tandem cells varies from minutes to

few hours, even for the most efficient devices, which is directly related to the severe photodegradation of semiconductors in aqueous solutions. Therefore, PEC Tandem cells technologies is still in its early stages, and many challenges still need to be overcome. For instance, the front photoelectrodes must be transparent to guarantee that sub-bandgap photons are transmitted to the rear photoelectrode. Furthermore, novel heterojunctions, protective layers, and cocatalysts must be employed for enhancing light absorption, charge transfer, interfacial catalysis, and stability of the photoelectrodes.

In this context, the following section aims to summarize the search for efficient semiconductors in PEC water splitting, in addition to introducing the metal oxides $BiVO_4$ and CuO as promising photoanodes and photocathodes, respectively, for bias-unassisted water splitting using PEC Tandem devices.

2.5 Semiconductors for PEC water splitting

To date, most of the PEC research has been focused on developing efficient photoanodes for OER, which is the rate-limiting step for overall water splitting.[25,58] In the last decades, binary metal oxides – semiconductors composed of a single metal cation with an oxygen anion – such as TiO_2,[59] WO_3,[60] and α-Fe_2O_3[61] have been extensively investigated as photoanodes for water oxidation. However, these semiconductors have restricted PEC performance due to several inherent limitations. For example, the large bandgaps of TiO_2 and WO_3 severely restrict their visible absorption range, resulting maximum STH efficiencies lower than $< 4\%$. In contrast, although α-Fe_2O_3 has a suitable bandgap (2 eV) and excellent chemical stability, its PEC performance suffers from low charge mobility and a short hole diffusion length.[62] In general, the bandgap of binary oxides is determined by transitions between O 2p (valence band) and metal d (conduction band) states[63]; the typical localized nature of these O 2p orbitals typically leads to a large hole effective mass, limiting the charge mobility of binary oxides.

As a result, ternary metal oxides composed of two metal cations in an oxide matrix (i.e., $BiVO_4$, $CuWO_4$, and $ZnFe_2O_4$) have recently been developed to overcome the limitations of binary oxides. For instance, adding occupied metallic *d* orbitals to binary oxides typically narrow the bandgap because these new states strongly hybridize with O 2p orbitals.[64] Therefore, the VB edge of ternary oxides tends to have more positive energies than that of binary oxides, enhancing visible light absorption and improving carrier mobility. Among all n-type semiconductors, ternary oxide $BiVO_4$ has been the most successful photoanode in Tandem cells (Table 1) because of its excellent electronic, structural, and PEC properties. Nevertheless, novel

ternary oxides will undoubtedly be identified in the following years. Ideally, these new materials must exhibit (i) bandgap less than 2 eV, (ii) STH efficiency higher than 10%, (iii) VB edge at highly oxidative potentials, and (iv) excellent chemical stability.

Compared to n-type semiconductors often employed as photoanodes in PEC devices, p-type metal oxides have received relatively less attention for use as photocathodes. In recent decades, most photocathode research has been focused on non-oxide semiconductors, including, for instance, p-Si[65] and p-GaP[66]. Nevertheless, the metal oxides CuO and Cu_2O have recently been investigated as photocathodes in PEC water splitting due to their narrow bandgaps, extremely high theoretical photocurrent densities, and excellent absorption of visible light.[26-27] Unfortunately, these Cu-based photocathodes are highly unstable in aqueous solutions during water reduction reactions, being critically important to develop protective layers for mitigating their self-corrosion. Furthermore, it is crucial to emphasize that novel ternary oxides, including, for instance, $CuBi_2O_4$ and $LaFeO_3$, $CuFeO_2$, and $ZnFe_2O_4$, have also been identified as promising photocathodes with higher chemical stability than typical bimetallic oxides during water reduction reactions.[67-68]

In this context, motivated by the promise of metal oxide semiconductors in PEC water splitting, we developed in this work, for the first time according to our knowledge, a Tandem cell device composed of a $BiVO_4$-based photoanode coupled with a CuO-based photocathode. The structural, optical, electronic, and PEC properties of these two semiconductors will be briefly discussed in sections 2.5.1 and 2.5.2, respectively.

2.5.1 Bismuth vanadate ($BiVO_4$)

In recent years, (monoclinic-scheelite) $BiVO_4$ has been considered one of the most efficient photoanodes for OER due to its high theoretical photocurrent density (7.5 mA cm^{-2}, corresponding to an STH efficiency of 9.2%), narrow bandgap (~2.4 eV), and suitable band structure (with a highly oxidative VB edge at ~2.4 V vs. RHE and a CB edge at ~0 V vs. RHE).[22-23] Specifically, there are three main crystal types of $BiVO_4$: tetragonal zircon (t-z), tetragonal scheelite (t-s), and monoclinic scheelite (m-s).[18] For all these structures, (i) each V atom is coordinated with four O atoms in a VO_4 tetrahedron, (ii) each Bi atom is coordinated with eight O atoms in a BiO_8 octahedron, and (iii) each O is coordinated with two Bi centers and one V center. Figures 12(a,b) show the crystal structures of the most common t-z and m-s polymorphs of $BiVO_4$. In particular, for the t-z $BiVO_4$, each BiO_8 unit is surrounded by six VO_4

tetrahedrons; this specific polymorph has a wide bandgap energy of 2.9 eV due to the dominance of O 2p orbitals in its VB and V 3d states in its CB (Figure 12c).[22]

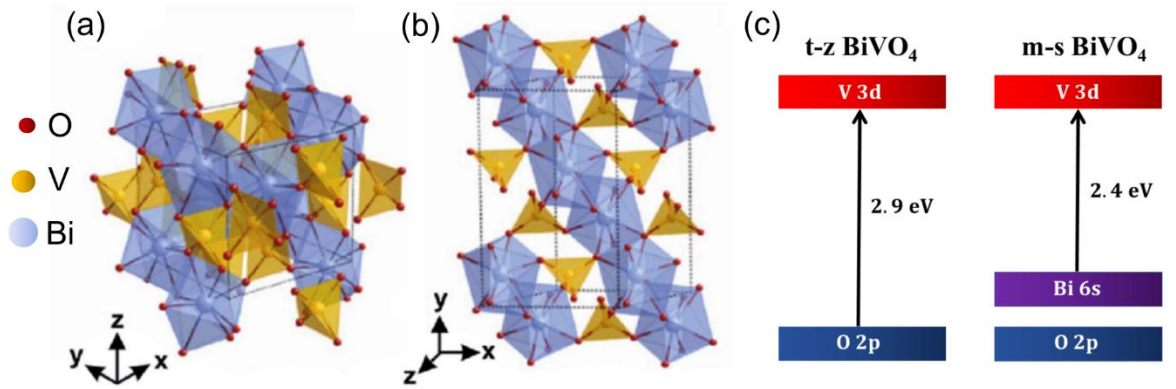

Figure 12 – Crystal structures of the most common $BiVO_4$ polymorphs: (a) tetragonal zircon and (b) monoclinic scheelite. (c) Schematic band structure of zircon-and scheelite-type $BiVO_4$.
Source: Adapted from GIMÉNEZ *et al.*[18]

In contrast, the two scheelite structures have eight VO_4 tetrahedra around each BiO_8 octahedron. Remarkably, Bi 6s orbitals appear above the O 2p orbitals for these polymorphs, reducing their bandgaps and increasing their visible absorption range (Figure 12c).[18,22] However, it is well known that the m-s $BiVO_4$ outperforms all other polymorphs in terms of PEC performance. The difference in PEC activities between the t-s and m-s structures has been attributed to different distortions in the local environments of V and Bi ions: whereas in the t-s structure, all V-O bond lengths are equal (1.73 Å), and there are only two Bi-O bond lengths (2.4 and 2.47 Å), in the m-s structure, there are two different V-O bond lengths (1.69 and 1.76 Å) and four different Bi-O bond lengths (2.35, 2.37, 2.52, and 2.63 Å). This distortion in the m-s $BiVO_4$ (breaking the fourfold symmetry) has been shown to enhance the local polarization, increasing the electron-hole separation and, consequently, the PEC performance.[69]

In a pioneering study, Kudo *et al*. proposed that the m-s $BiVO_4$ has superior PEC performance compared to the t-z polymorph due to their different electronic structures.[69] As shown in Figure 12c, while the optical transitions in t-z $BiVO_4$ occur between filled O 2p orbitals and empty V 3d orbitals, in the m-s structure, these electronic transitions apparently occur in Bi 6s orbitals or hybrid Bi 6s-O 2p orbitals and 3d empty orbitals. Indeed, experimental and theoretical works have shown that the m-s $BiVO_4$ has higher visible light absorption due to the smaller bandgap energy (2.4 and 2.9 eV for m-s and t-z $BiVO_4$, respectively). However, according to recent density functional theory (DFT) studies and X-ray spectroscopies, although m-s $BiVO_4$ exhibits Bi 6s orbitals above O 2p orbitals, the optical transitions under visible

illumination still occur between filled O $2p_\pi$ and empty V 3d orbitals.[70–72] Thus, the higher visible light absorption of m-s $BiVO_4$ is not directly associated with the Bi 6s orbitals but rather with the crystal distortion that pushes the O 2p states upwards and reduces its bandgap.

Interestingly, the nature of optical transition in m-s $BiVO_4$ was controversial in the literature. However, recent studies using advanced spectroscopic techniques (XAS, RIX, XPS, UV-vis) and DFT calculations have unambiguously confirmed that m-s $BiVO_4$ has optical transitions of indirect nature;[70,73] nevertheless, direct transitions also persist at slightly higher energies of $\sim$200 meV compared to indirect transitions, explaining the initial controversy. Furthermore, the charge carrier effective masses in m-s $BiVO_4$, determined by DFT, are also lower than in other $BiVO_4$ polymorphs and typical metal oxide semiconductors. The effective mass of electrons at the CB edge and holes at the VB edge of m-s $BiVO_4$ are $\sim$0.9 m_e and $\sim$0.7 m_e, respectively (m_e is the rest mass of the electron).[71] In comparison, t-z $BiVO_4$ has effective electron and hole masses of ~17.3 m_e and $\sim$1.2 m_e.[74] Importantly, it is well known that lighter charge carriers are ideal for PEC applications as they have a higher probability of reaching the semiconductor surface without undergoing recombination.

Table 2 - Some physical properties of m-s $BiVO_4$ and CuO at room temperature (300 K).

Property	**m-s $BiVO_4$**	**CuO**
Density (g cm^{-3})	6.1	6.3
Molar mass (g mol^{-1})	323.92	79.55
Refractive index	2.45	1.4
Dielectric constant	68	18
Bandgap (eV)	2.4 – 2.6 (indirect)	1.2 – 1.7 (direct)
Hole effective mass (m_e)	0.7	7.9
Electron effective mass (m_e)	0.9	$0.4 - 0.95$

Source: By the author.

Table 2 summarizes some important physical properties of m-s $BiVO_4$. Despite all these advantageous properties, m-s $BiVO_4$ has some intrinsic limitations, including (i) slow water oxidation kinetics, resulting in the accumulation of photogenerated holes at its surface, (ii) poor electronic conductivity due to a small polaron hopping conduction mechanism, (iii) significant recombination of electron-hole pairs both in bulk and surface, and (iv) relative chemical instability in aqueous solutions. In our research group, surface modification of $BiVO_4$ photoanodes with bimetallic oxide cocatalysts ($FeMO_x$, M = Co, Ni, Mn) has been extensively

applied to mitigate the aforementioned problems.[58,75] Nevertheless, several other approaches have also been applied, including, for instance, doping[76] and crystal facet engineering.[77] Interestingly, high photocurrent densities of 6.72 mA cm^{-2} (almost 90 % of the theoretical value), have already been reported for $BiVO_4$-based photoanodes.[78]

2.5.2 Cupric oxide (CuO)

CuO (Copper (II) oxide or cupric oxide) is an intrinsically p-type semiconductor with a monoclinic crystalline structure (lattice parameters $a = 4.6837$ Å, $b = 3.4226$ Å, $c = 5.1288$ Å, $\beta = 99.54°$, $\alpha = \gamma = 90°$), where four oxygen atoms coordinate each Cu atom in an approximately planar configuration (Figure 5a).[79] Remarkably, CuO has been considered a promising photocathode for application in Tandem cells due to its narrow bandgap of 1.2 to 1.7 eV, an impressively high theoretical photocurrent density (35 mA cm^{-2}, corresponding to an STH efficiency of 43%), and CB edge position suitable for HER.[26-27] Furthermore, CuO has a flat band potential around 1.0 V vs. RHE, indicating a large V_{onset} potential for PEC water splitting.[80] Other important properties of CuO are listed in Table 2. Although cupric oxide exhibits high activity for HER under simulated sunlight illumination, few works have focused on developing CuO-based photocathodes. Indeed, most of the PEC research involving Cu-based photocathodes is concentrated on the p-type Cu_2O (cuprous oxide), which, in turn, has an unfavorable higher bandgap (2.2 eV) and lower theoretical photocurrent density (14.7 mA cm^2) compared to that of CuO.

Despite all their attractive advantages, CuO photocathodes typically suffer severe chemical instability under water reduction operating conditions. For a photoelectrode to be stable against photocorrosion, its anodic and cathodic decomposition potentials ($E_{dec,n}$ and $E_{dec,p}$, respectively) must fulfill the following conditions: $E(H^+/H_2) < E_{dec,p}$ e $E(O_2/H_2O) > E_{dec,n}$ (Figure 13b).[27] Therefore, CuO is highly unstable because its anodic and cathodic decomposition potentials are located close to or within their bandgap (Figure 13c).[81] That is, the photogenerated electron-hole pairs may participate in the self-corrosion of CuO rather than being involved in HER. Under cathodic potentials and illumination, CuO is specifically reduced to Cu_2O, and further reduction produces metallic Cu.[82] Thus, constructing protective layers on the CuO surface is critically important to protect this material against photocorrosion. In this context, modification with cocatalysts,[83] morphology control,[84] and formation of

heterojunctions[85] have been widely used techniques to mitigate (with relative success) problems with stability and charge recombination in CuO-based photocathodes.

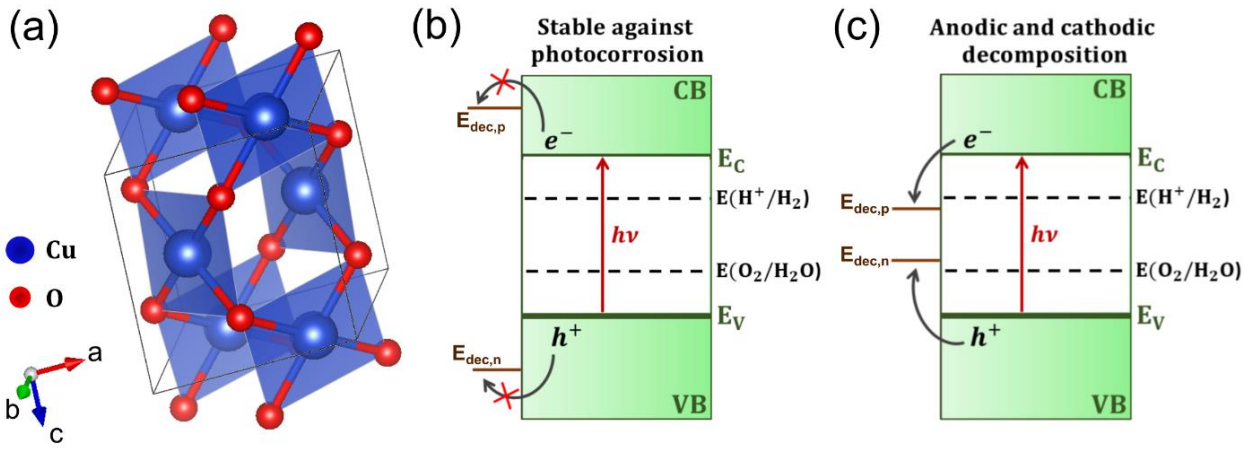

Figure 13 – (a) Crystal structure of monoclinic CuO; and thermodynamic stability against photodecomposition: (b) stable, and (c) unstable photoelectrode. CuO is a semiconductor with energy band positions similar to case (c).

Source: (a) KARTTUNEN [86]; (b) Adapted from LI *et al*.[27]

3 METHODOLOGY

3.1 Synthesis of $BiVO_4$-based and CuO photoelectrodes

All photoelectrodes developed in this work were synthesized via radio frequency (RF) magnetron sputtering deposition, a well-known technique that offers large-area deposition, low contamination, high reproducibility, and the ability to produce high-quality dense and well-adhered films.[58,75,87] Briefly, this technique employs high-energy ions (typically Ar^+) to eject atoms and atomic clusters from a target precursor of the desired compound onto a conductive substrate (e.g., FTO). Herein, bare $BiVO_4$ (BVO) films were deposited from a homemade ceramic and stoichiometric $BiVO_4$ target. Importantly, our $BiVO_4$ ceramic disk (see Figure 14) was synthesized through a conventional solid-state reaction, where the precursor powders consisting of V_2O_5 (99.6%, Alfa Aesar) and Bi_2O_3 (99.5%, Alfa Aesar) were stoichiometric weighted and mechanically ball-milled for 24 h in a polyethylene container with Zr cylinders and isopropyl alcohol. The resulting wet oxide mixture was dried to remove the alcohol and calcined at 500 ℃ for 1 h. Afterward, the as-calcined powders were mechanically ball-milled for 24 hours and then pressed at 15 MPa to produce a 55-mm-diameter disk. After this step, the as-compacted $BiVO_4$ target was sintered at 800 °C for 2 hours in an air atmosphere to achieve the desired crystalline phases and densification.[58,75] Finally, the crystallized $BiVO_4$ target was machined to have a 2-inch diameter and 3 mm thickness.

For all RF-magnetron sputtering depositions, (i) the distance between the targets and the FTO was set at 5 cm, and (ii) the base pressure of the sputtering chamber was set at 7.5×10^{-6} Torr. The bare BVO films were deposited with an atmosphere of argon and oxygen gases (18.5 Ar scm and 2.1 O_2 scm) at a working pressure of 3.2×10^{-2} Torr. The RF power was set at 50 W, and the depositions occurred between 6 and 12 minutes. In sequence, these as-deposited films were calcined in an ambient atmosphere at 400 °C for 1h, resulting in crystalline $BiVO_4$ films. A thin layer of $FeNiO_x$ was deposited on the BVO films using a Fe-Ni metal alloy target (50 wt. % Fe and 50 wt. % Ni, 99.9% purity) with an Ar/O_2 (18.5:2.1 scm) working pressure of 4.0×10^{-2} torr and deposition times varying between 30 and 90 seconds.

In contrast, CuO films were deposited from a metallic Cu target (99.9% purity), using a pure argon atmosphere at a working pressure of 3.2×10^{-2} Torr and RF power set at 50 W. The sputtering depositions of metallic Cu were varied between 5 and 30 minutes. These as-deposited films were annealed in an ambient atmosphere at 550 °C for 8 h, resulting in

crystalline CuO films. A thin layer of BVO was deposited over the CuO films using our prepared ceramic target, with an Ar/O_2 working pressure of 4.0×10^{-2} Torr and deposition times ranging from 2 to 6 minutes.

Figure 14 – Digital photographs of the (as-prepared) $BiVO_4$, Fe-Ni, and Cu-target. The circular paths formed on the surface of the targets after magnetron sputtering deposition are the tracks left behind by secondary electrons under the influence of orthogonal magnetic and electric fields.
Source: By the author.

3.2 Physical characterization

The crystalline structures of the BVO and CuO-based films were characterized by X-ray diffraction (XRD, Rigaku Ultima IV diffractometer) with Cu Kα ($\lambda = 0.15406$ nm) radiation. Raman spectra were obtained from a Witec alpha 300 microscope equipped with a linear stage, piezo-driven, 20× Nikon objective lens (NA = 0.46), and polarized laser ($\lambda =$ 488 nm). Scanning electron microscopy (SEM, Sigma Gemini model field emission microscope) was employed to analyze the morphology of the films. UV-vis absorption measurements were performed on a Shimadzu UV-2600 spectrometer equipped with an integrating sphere. Film thicknesses were determined using a DekTak 150 Veeco profilometer. The surface chemical states and composition of the films were investigated by X-ray photoelectron spectroscopy (XPS, Scienta-Omicron ESCA+ spectrometer) with a monochromatic Al Kα ($h\nu = 1486.6$ eV) radiation source. The XPS spectra were recorded at a pass energy of 30 eV with a step energy of 0.05 eV. A low-energy electron flood gun was utilized to eliminate charging effects during XPS measurements. All the binding energies were calibrated using adventitious carbon (C1s, 284.8 eV) as a reference. The XPS spectra were fitted from CasaXPS software using Shirley-type background subtraction.

3.3 Photoelectrochemical measurements

The PEC performances of our photoelectrodes were individually characterized in a typical three-electrode configuration with an Autolab (PGSTAT128N) electrochemical workstation. The BVO-based or CuO films were used as a working electrode (area: 1 cm^2), Ag/AgCl as a reference electrode, and platinum foil as a counter electrode (Figure 15a). All PEC measurements were performed in 1 M potassium borate buffer (KBi, pH 9.5). Importantly, this KBi electrolyte was prepared by adjusting the pH of a 1 M H_3BO_3 solution with KOH. Before each PEC measurement, argon gas was purged for at least 10 minutes to remove any dissolved oxygen. The solar simulator for the PEC experiments was a Xe lamp (300 W) coupled with an AM 1.5G filter. The light intensity was carefully calibrated at 100 mW cm^{-2} with a Gentec XLP 12-3S-H2-D0 photometer. Photocurrent density vs. potential (j-V) curves were performed using linear sweep voltammetry with a scan rate of 10 mV s^{-1}. Electrochemical impedance spectroscopy (EIS) was performed from 100 kHz to 0.1 Hz, with an AC voltage amplitude of 10 mV, at the illuminated open-circuit potential or specifically applied bias. The chronoamperometry measurements (j-t curves) were performed for 1 hour under fixed applied potentials (1.23 V vs. RHE for photoanodes and 0.46 V vs. RHE for photocathodes), with constant Ar gas purging during the entire measurement.

Mott-Schottky (MS) analyses were performed at $+1$ kHz under dark conditions in a suitable potential range for each photoelectrode. The MS equations for *n*-type and *p*-type semiconductors are defined by [88]:

$$\frac{1}{C_{SC}^2} = \frac{2}{qA^2\epsilon_r\epsilon_0 N_D}\left(E - E_{FB} - \frac{kT}{e}\right), \qquad \text{for n-type} \tag{22}$$

$$\frac{1}{C_{SC}^2} = \frac{2}{qA^2\epsilon_r\epsilon_0 N_A}\left(-E + E_{FB} - \frac{kT}{e}\right), \qquad \text{for p-type,} \tag{23}$$

where C_{SC} is the total capacitance in the space-charge depletion layer, ϵ_0 is the permittivity in the vacuum, ϵ_r is the relative permittivity of the semiconductor ($\epsilon_r = 68, 13,$ and 18 for n-BVO[89], p-$FeNiO_x$[90], p-CuO semiconductors[26], respectively), A is the geometric surface area of the working electrode, E is the applied potential, E_{FB} is the flat-band potential, N_D is the donor carrier density, N_A is the acceptor carrier density, T is the temperature, and q is the electric charge. The flat band potential is calculated from the intercept of the plot $1/(C_{SC})^2$ versus E, whereas the majority-carrier densities are calculated from the respective slopes

$$N_D = \frac{2}{\mathrm{A}^2\epsilon_\mathrm{r}\epsilon_0 q}\left[\frac{d(\mathrm{C}_{\mathrm{SC}}^{-2})}{dE}\right]^{-1}, \text{and } N_A = -\frac{2}{\mathrm{A}^2\epsilon_\mathrm{r}\epsilon_0 q}\left[\frac{d(\mathrm{C}_{\mathrm{SC}}^{-2})}{dE}\right]^{-1}. \tag{24}$$

The incident photon-to-current conversion efficiency (IPCE) was performed by measuring the photocurrent density under (i) monochromatic light irradiation with a Xe lamp (300 W) coupled with a monochromator grating (Bausch&Lomb 1350 grooves/mm) and (ii) applied potentials (1.23 V vs. RHE for photoanodes and 0.45 V vs. RHE for photocathodes). The light intensity in each wavelength was determined with a Gentec XLP 12-3S-H2-D0 photometer. The IPCE values were calculated with equation (25), where j_{ph} is the current density under monochromatic radiation, and P_{light} is the respective power density.

$$\text{IPCE}(\%) = \frac{|j_{ph}(mA\ cm^{-2})| \times 1240}{\lambda(nm) \times P_{light}(mW\ cm^{-2})} \times 100(\%). \quad (25)$$

The applied bias photon-to-current efficiency (ABPE) of BVO and CuO-based films was calculated from the respective j-V curves by using the equation (26), where j_{ph} is the photocurrent density, V_{app} is the applied potential vs. RHE, and P_{light} is the calibrated power density of the simulated AM 1.5G illumination (100 mW cm^{-2}).

$$\text{ABPE}(\%) = \frac{|j_{ph}|(mA\ cm^{2}) \times \left(1.23 - \left|V_{app}\right|\right)(V)}{P_{light}(mW\ cm^{-2})} \times 100(\%). \quad (26)$$

The charge separation ($\eta_{sep}(\%)$) and charge transfer ($\eta_{cat}(\%)$) efficiencies were calculated from the methodology proposed by Dotan. *et al*.[61] In particular, the photocurrent density (j_{ph}) calculated in PEC measurements results from three distinct processes: (i) light absorption, (ii) separation and transport of photogenerated charges, and (iii) injection of photogenerated charges into the electrolyte. Therefore, the photocurrent density can be expressed by $j_{ph} = j_{abs} \times \eta_{sep} \times \eta_{cat}$, where j_{abs} is the absorption current density defined as the photocurrent obtained when all absorbed photons are converted to electric current, η_{sep} is the electron-hole separation yield, and η_{cat} the charge transfer (injection) yield. The absorption current density (j_{abs}) can be calculated using the following equation[23]:

$$j_{abs} = \int_{\lambda_1}^{\lambda_2} \frac{\lambda(nm)}{1240\ (V \cdot nm)} \phi(\lambda)\left(1 - 10^{-A(\lambda)}\right)\left(\frac{mW}{cm^2 \cdot nm}\right) d\lambda, \quad (27)$$

where $\phi(\lambda)$ is the AM 1.5G photon flux in units of $W \cdot m^{-2} \cdot nm^{-1}$ (provided by the National Renewable Energy Laboratory, USA), and A(λ) is the absorbance at different wavelengths estimated by UV-vis measurements. Note that $(1 - 10^{-A(\lambda)})$ is the light-harvesting efficiency (or absorptance) of the photoelectrode, defined as the fraction of electron-hole pairs generated by incident photon flux. To determine the η_{sep} and η_{cat} efficiencies for the photoanodes, the PEC measurements were performed by adding 0.25M Na_2SO_3 into the 1 M KBi electrolyte. Precisely, Na_2SO_3 acts as a hole scavenger since the sulfite oxidation ($SO_3^{-2} + h^+ \rightarrow SO_3^-, E^0 =$

0.73 V_{RHE}) is a much kinetically and thermodynamically easier reaction than OER.[23] In this case, all photogenerated holes are readily consumed in the sulfite oxidation, such that $\eta_{cat} \approx$ 100% and $\eta_{sep} = j_{ph}^{Na_2SO_3}/j_{abs}$, where $j_{ph}^{Na_2SO_3}$ is the photocurrent density in the presence of hole scavengers. Therefore, the values of η_{cat} and η_{sep} can be determined by comparing the photocurrent densities in the presence ($j_{ph}^{Na_2SO_3}$) and absence ($j_{ph}^{H_2O}$) of the sacrificing agent:

$$\eta_{sep} = j_{ph}^{Na_2SO_3}/j_{abs}; \quad (28)$$

$$\eta_{cat} = j_{ph}^{H_2O}/j_{ph}^{Na_2SO_3}. \quad (29)$$

The two-electrode measurements (for the tandem cell) were conducted by connecting the working electrode lead of the potentiostat to the BVO-based photoanode, and the reference and counter electrode leads to the CuO-based photocathode (Figure 15b). The light source was a Xe lamp (300 W) coupled with an AM 1.5G filter (100 mW cm^{-2}). The irradiated area was 0.1 cm^2 for each photoelectrode. Furthermore, the photoanode was placed in front of the photocathode in our Tandem cell (stacked configuration). As a result, the light is initially absorbed by the BVO-based photoanode and then transmitted to the CuO-based photocathode.

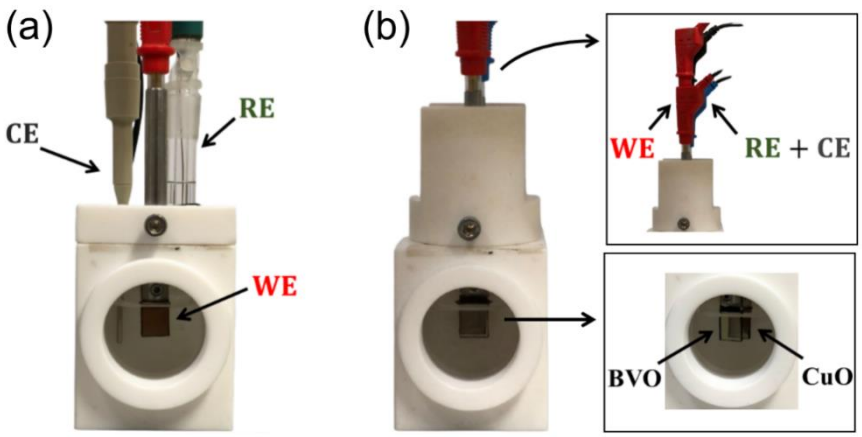

Figure 15 – Digital photographs of the (a) three-electrode configuration and (b) two-electrode configuration. Source: By the author.

3.4 Interfacial band alignment model

The interfacial band alignment of p-n heterojunctions (under dark) was calculated by employing the classical band bending model (Anderson's model).[36,58,75,91] This simplified model captures the SCR development through the following hypotheses: (i) surface states are neglected, that is, the band edges are fixed at the p-n interface, (ii) the total charge density ρ across the SCR is determined only by the concentration of ionized impurities, and (iii) bandgap energies and electronic affinity are fixed during the alignment of Fermi energies. Figure 16a

shows the band diagrams for typical n-type and p-type semiconductors before equilibrium. After contact (Figure 16b), the different Fermi energies align and produce a built-in potential (Ψ_{bi}) defined by $q\Psi_{bi} = E_{F1} - E_{F2}$. Importantly, this built-in potential manifests as the potential drops in the *n* and *p*-side layers (Ψ_1 and Ψ_2, respectively), that is, $\Psi_{bi} = \Psi_1 + \Psi_2$. Furthermore, the spatial extent of the as-developed SCR is given by the depletion lengths W_1 and W_2 for the n and p-type layers, respectively. By employing these hypotheses, the unidimensional Poisson equation ($\nabla^2\Psi = \rho/\epsilon_0\epsilon_r$, where ϵ_0 is the vacuum permittivity, ϵ_r is the semiconductors' dielectric constant, and $\rho = -qN_D$ for $x \in [-W_1, 0]$ and $\rho = qN_A$ for $x \in [0, W_2]$) provides the following expression for the CB edge as a function of position:

$$E_C(x) = \begin{cases} E_{c1} + q\Psi_1, -L_1 < x < -W_1 \\ E_{c1} + q\Psi_1 - \dfrac{qN_D}{2\epsilon_0\epsilon_{r,n}}(x + W_1)^2, -W_1 \le x < 0 \\ E_{c2} - q\Psi_2 + \dfrac{qN_A}{2\epsilon_0\epsilon_{r,p}}(x - W_2)^2, 0 \le x < W_2 \\ E_{c2} - q\Psi_2, W_2 < x < L_2 \end{cases}, \tag{30}$$

where L_1 (L_2) is the thickness of the n(p)-type layer. It is straightforward to show that:

$$\Psi_1 = \frac{N_D W_1^2}{2\epsilon_0\epsilon_{r,n}} = \frac{\epsilon_{r,2}N_A}{\epsilon_{r,2}N_A + \epsilon_{r,1}N_D}\Psi_{bi} \text{ and } \Psi_2 = \frac{N_A {W_2}^2}{2\epsilon_0\epsilon_{r,p}} = \frac{\epsilon_{r,n}N_D}{\epsilon_{r,p}N_A + \epsilon_{r,n}N_D}\Psi_{bi}, \tag{31}$$

$$W_1 = \left(\frac{2\epsilon_0\epsilon_{r,p}N_A\Psi_{bi}}{N_D(\epsilon_{r,p}N_A + \epsilon_{r,n}N_D)}\right)^{1/2} \text{ and } W_2 = \left(\frac{2\epsilon_0\epsilon_{r,n}N_A\Psi_{bi}}{N_A(\epsilon_{r,p}N_A + \epsilon_{r,n}N_D)}\right)^{1/2}. \tag{32}$$

The Fermi energy after equilibrium is defined as: $E_{F,dark} = E_{F1} - q\Psi_1 = E_{F2} + q\Psi_2$. Note also that (i) $E_V(x)$ can be obtained from $E_C(x)$ and bandgap energies and (ii) the as-developed built-in electric field inside the SCR points from the n-type to the p-type semiconductor. These equations are valid under the application of external potential by making the substitution $\Psi_{bi} \to \Psi_{bi} - V$, where $V > 0$ for reverse bias and $V < 0$ for forward bias.

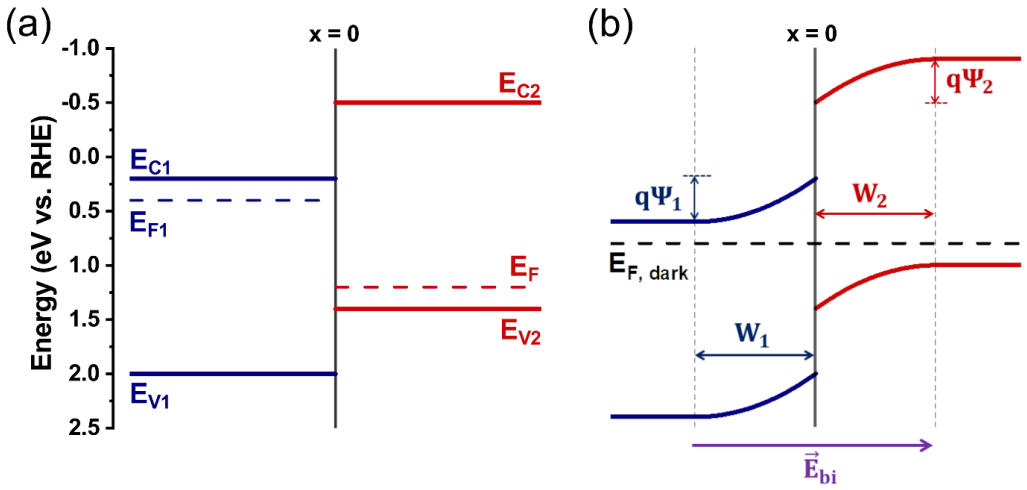

Figure 16 – (a) Isolated band diagrams of typical n-type and p-type semiconductors before contact, and (b) interfacial band alignment of the p-n heterojunction under dark (equilibrium), showing the production of an SCR and a built-in electric field ($\vec{E}_{bi}$) poiting from the n-type to the p-type semiconductors.
Source: Elaborated by the author.

4 RESULTS AND DISCUSSION

The results of this dissertation were divided into three main sections, contemplating the development of BVO/$FeNiO_x$ photoanodes for OER (section 4.1) and CuO photocathodes for HER (section 4.2), and ultimately, the application of these optimized photoelectrodes in a simple and low-cost Tandem cell for bias-unassisted overall water splitting (section 4.3.)

4.1 Development of $BiVO_4$-based photoanodes

In this work, all $BiVO_4$-based photoanodes were produced from magnetron sputtering deposition. To optimize our bare $BiVO_4$ films for OER, we varied the deposition time (i.e., film thickness) between 6, 8, 10, and 12 minutes. The as-sputtered films have an amorphous character, requiring heat treatment to obtain the crystalline phase. Previous work published by our research group showed that annealing at 400 °C for 1 hour is the optimal heat treatment for as-sputtered $BiVO_4$ films.[75] Therefore, this annealing condition was employed to crystallize the as-sputtered BVO films. After investigating the PEC performance of these unmodified films, we deposited $FeNiO_x$ cocatalyst (with 30, 60, and 90 seconds) on the surface of the optimized BVO film to improve its PEC properties and chemical stability. The morphological, structural, optical, electronic, PEC, and interfacial band alignment properties of these photoanodes are discussed in the following sections.

4.1.1 Structural and morphological properties

XRD and Raman spectroscopy were employed to investigate the structural properties of our bare BVO films. Figure 17a shows the XRD patterns for the BVO films deposited in 6, 8, 10, and 12 minutes and annealed at 400 °C for 1 hour. The analysis of XRD patterns is challenging due to the intense presence of substrate (FTO) peaks. Nevertheless, the diffraction peaks at 19.0 ° and 29.0 ° correspond, respectively, to the (110) and (121) crystalline planes of the monoclinic $BiVO_4$ (JCPDS no. 00-014-0688). The additional peaks were not identified due to their low intensity compared to the prominent ones from FTO and BVO. Remarkably, all XRD peaks have increased intensity for longer deposition times, which is expected due to the production of more atomic layers to diffract X-rays. This behavior also explains why the low-intensity peak at 35.3 ° slightly appears for BVO films deposited at 10 and 12 minutes; for low thicknesses, the low-intensity peaks of BVO are superimposed by the measurement noise. It is

essential to emphasize that no impurities or secondary phases were observed in the XRD patterns, showing that our as-sputtered BVO films were successfully converted to monoclinic $BiVO_4$ following annealing.

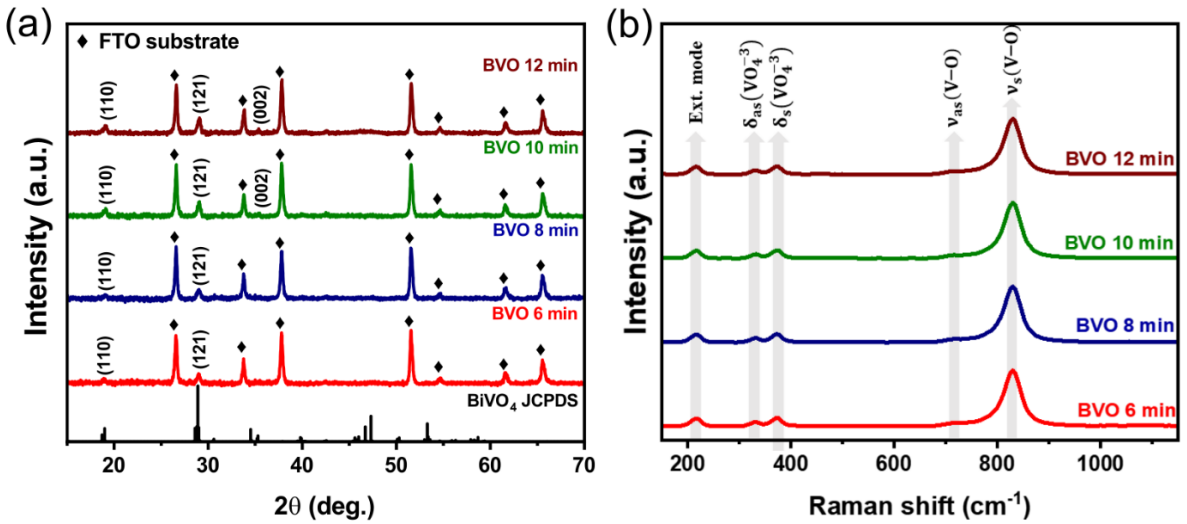

Figure 17 – (a) XRD patterns and (b) Raman spectra for BVO films deposited in 6, 8, 10, and 12 minutes and annealed at 400° for 1 hour.
Source: By the author.

Conclusively, Figure 17b shows the Raman spectra for these as-annealed BVO films, clearly evidencing five vibrational bands at about 210, 327, 367, 712, and 826 cm^{-1}, which are characteristic signatures of monoclinic $BiVO_4$.[92-93] The most intense band at 826 cm^{-1} corresponds to the symmetrical stretching mode of the V–O bonds [ν_S (V-O)], whereas the shoulder peak at 826 cm^{-1} refers to their asymmetric stretching modes [ν_{AS} (V-O)]. The vibration bands at 327 and 367 cm^{-1} are associated with asymmetric [δ_{AS} (VO_4^{-3})] and symmetrical [δ_S (VO_4^{-3})] deformation modes of the VO_4^{-3} tetrahedron, respectively. Finally, the band at 210 cm^{-1} refers to the external modes corresponding to the translations and vibrations of the molecular entities within the crystalline structure. Importantly, there were no significant differences between the Raman spectra of BVO films with different thicknesses, unambiguously evidencing that all our as-sputtered BVO films were converted to high-purity monocyclic $BiVO_4$ films following annealing. As a result, the increased XRD peaks intensity for BVO films deposited in longer times is directly associated with their thickness (more atomic layers for diffracting X-rays) rather than a higher degree of crystallization.

Scanning electron microscopy (SEM) was used to investigate the morphology of crystallized BVO films. As shown in the top-view SEM images (Figure 18), all BVO films showed a compact and dense structure composed of particles with similar shapes that uniformly

cover the FTO substrate and grow progressively with increasing deposition. This behavior is expected for sputtering depositions, where the atoms and atomic cluster of the BVO target impinge on the substrate and form mobile nucleation sites, diffusing until their total energy is minimized. With increasing deposition time and thermal treatment, such nucleation sites and gran boundaries tend to grow, giving rise to increasingly larger $BiVO_4$ particles.[94-95] Indeed, the average particle size (for representative surface samples) grows from 220 nm for the 6-minute film to 430 nm for the 12-minute film. Interestingly, the growth of our BVO films occurs by the Volmer-Weber mechanism, where the nucleated particles grow as isolated hemispheres, and the continuous film is formed by the juxtaposition of such structures.[95] As shown in Figure 19, cross-sectional images of as-annealed BVO films are challenging to analyze due to the small thickness of the $BiVO_4$ layers and the inhomogeneous character of the FTO surface. Therefore, profilometry was used to determine the thicknesses of our crystalline BVO films, which estimates a layer of about 63 nm, 85 nm, 110 nm, and 125 nm for the films deposited in 6, 8, 10, and 12 minutes, respectively. Importantly, these thicknesses roughly match the known linear deposition rate of 10.06 nm min^{-1} for the crystallized BVO films.

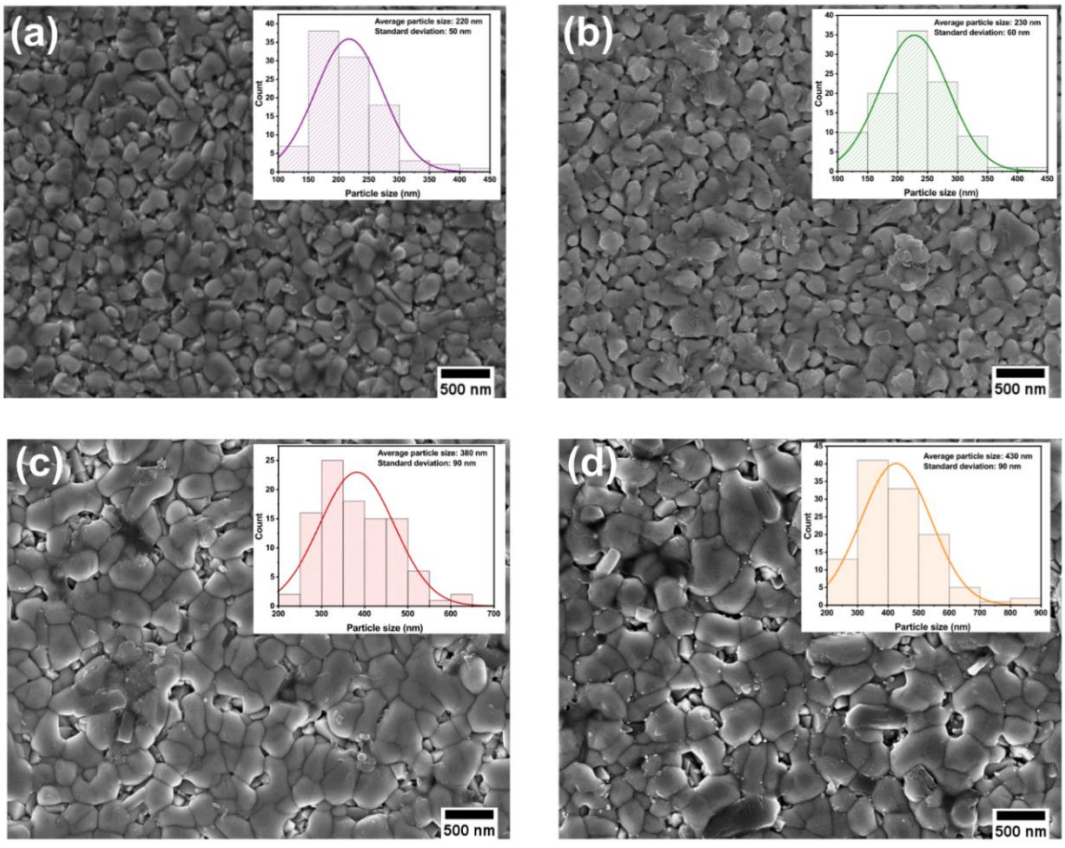

Figure 18 – Top-view SEM images for the bare BVO films deposited in (a) 6, (b) 8, (c) 10, and (d) 12 minutes. The average particles size and standard deviations for representative samples are shown in the insets.
Source: By the author.

Due to their similar structural and morphological properties, BVO films deposited at 6, 8, 10, and 12 minutes and calcined at 400 °C for 1 hour were employed as photoanodes for OER (see section 4.1.3). Among these films, the BVO film with the highest PEC activity was chosen to undergo surface modification with the $FeNiO_x$ cocatalyst. The bimetallic oxide $FeNiO_x$ was deposited for 30, 60, and 90 seconds (via magnetron sputtering, using a Fe-Ni metal alloy target) on the surface of the optimized bare BVO. Remarkably, no apparent differences between the resulting BVO/$FeNiO_x$ and bare BVO films were identified in the XRD patterns, Raman spectra, and SEM images. Corroborating with previous publications,[58,75] the absence of $FeNiO_x$ effects in these analyses may be due to its ultrathin thickness (~1 nm, according to our alloy deposition rate) and amorphous character. As discussed in the following section, only the XPS technique, which is surface sensitive, successfully identified and characterized the composition of the as-deposited $FeNiO_x$ layer.

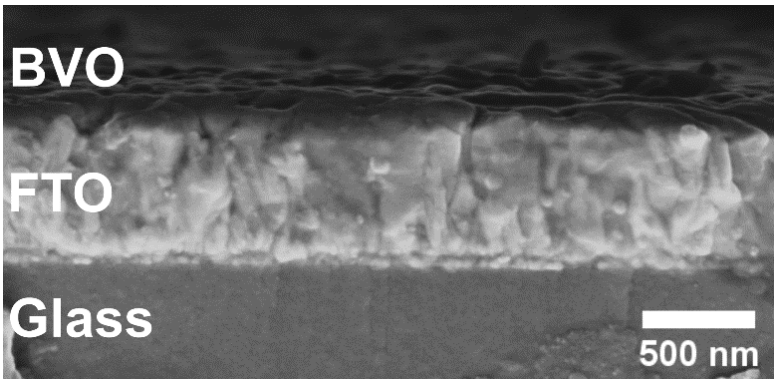

Figure 19 – Cross-sectional SEM image for the bare BVO film deposited in 8 minutes and annealed at 400° C for 1 hour.
Source: By the author.

4.1.2 Optical and electronic properties

In this section, we will only discuss the optoelectronic properties of BVO and BVO/$FeNiO_x$ films that were optimized for OER (i.e., bare BVO film deposited in 8 minutes and annealed at 400° C for 1 hour and BVO/$FeNiO_x$ film produced by depositing 60 seconds of $FeNiO_x$ on the surface of optimized BVO, see section 4.1.3) because the absorbance, bandgap, electronic structure, and surface chemical composition of our BVO-based films were not thickness dependent.

As shown in Figure 20a, the bare BVO has an absorption threshold of around 535 nm, characteristic of monoclinic $BiVO_4$ with a bandgap between 2.4 and 2.6 eV. Tauc analysis

(inset of Figure 20a) indicates that BVO has a direct bandgap of 2.58 eV, consistent with similar works.[96-97] Tauc analysis was also conducted with an indirect bandgap; however, the absorbance spectrum was not reliably simulated for $\alpha = 1/2$. It is crucial to emphasize that the UV-vis analysis becomes challenging due to the Fabri-Perot interference fringes, manifesting itself as oscillatory signals convoluted with the sample absorbance.[32] Our previous work associated the absorption tail seen for wavelengths above 535 nm with structural defects in the BVO film, including oxygen vacancies and the Bi/V ratio (see XPS discussion).[75] However, the absorption tail may be associated with interference fringes or the FTO background. Therefore, a future study should be directed for understanding the origin of this possible extended light absorption.

Figure 20b shows the effect of depositing $FeNiO_x$ on the absorbance spectrum of bare BVO film. Interestingly, there are no significant differences in the absorbance behavior up to ~ 480 nm; however, an intense absorption tail that extends to the infrared region is evidenced for the BVO/$FeNiO_x$ film. Wang *et al*. obtained a similar result for the BVO/$FeCoO_x$ film, suggesting that Fe-based bimetallic oxides can increase the absorption range of BVO photoanodes.[98] However, as discussed in section 4.1.3, the IPCE values for all $BiVO_4$-based films are null from 520 nm onwards, with no apparent redshift after $FeNiO_x$ deposition. This result shows that the light absorption extended by the absorption tails seen for BVO (possibly associated with structural defects) and BVO/$FeNiO_x$ cannot be directly converted into photocurrent densities.

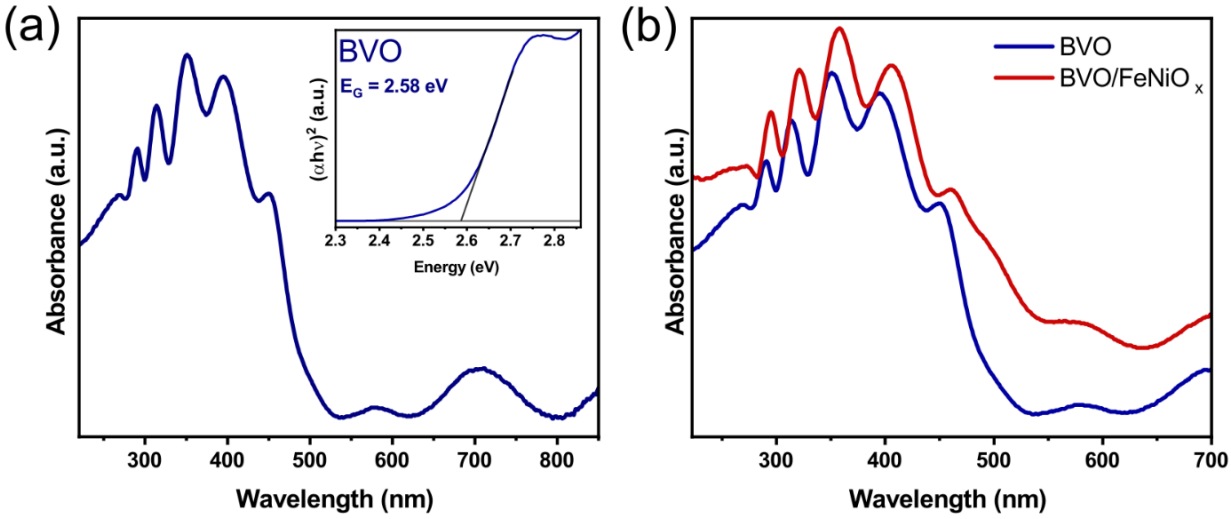

Figure 20 – (a) UV-vis absorption spectrum for the optimized BVO film (deposited in 8 minutes and annealed at 400° C) and Tauc Plot analysis (inset). (b) Comparison the absorbance profile of optimized BVO and BVO/$FeNiO_x$ films ($FeNiO_x$ layer deposited for 60 seconds).
Source: By the author.

X-ray photoelectron spectroscopy (XPS) was performed on the BVO and BVO/$FeNiO_x$ films to investigate their electronic structure and surface chemical composition. Figures 21a,b,c show the XPS spectra of our optimized bare BVO film. The high-resolution XPS spectra of Bi 4f (Figure 21a) exhibit a doublet with components at 158.9 and 164.2 eV, ascribed to the Bi $4f_{5/2}$ and Bi $4f_{7/2}$ spin-orbit splitting states, respectively. These two peaks are characteristic signatures of the Bi^{3+} species in the electronic structure of $BiVO_4$.[99] The high-resolution XPS spectra of the V 2p region (Figure 21b) show two peaks of V $2p_{1/2}$ at 524.3 eV and $2p_{3/2}$ at 516.6 eV, separated by an energy value of 7.5 eV. The positions and the separation between the V 2p doublet components are characteristic signatures of the V^{5+} oxidation state in the $BiVO_4$. However, the peak areas of the V 2p spin-orbit doublet do not match the 2:1 ratio predicted for the 2p orbital. Furthermore, the peak shape is asymmetric for a Gaussian/Lorentzian function fitting, thereby raising the prospect of another oxidation state, such as V^{4+}, which may induce oxygen defects/vacancies. In addition, the FWHM for the V $2p_{1/2}$ peak is 1.62-fold higher than that of the V $2p_{3/2}$. The anomalous behavior of the V 2p orbital is attributed to the Coster–Kronig effect, a well-known phenomenon that makes it challenging to distinguish V^{4+} and V^{5+} species by XPS.[100-101]

Furthermore, the O1s XPS spectra for the bare BVO film (Figure 21c) can be fitted into three distinct peaks. The peak at 529.5 eV (O_L) corresponds to the oxygen lattice in $BiVO_4$, and the less intense peak at 532.7 eV (O_C) is associated with the C-O groups. In contrast, the peak at 531.3 eV (O_{vo}) is a characteristic signature of oxygen vacancies/defects in semiconductor structures.[98,102] The presence of oxygen vacancies can significantly modify the electronic structure of $BiVO_4$ and, hence PEC characteristics of the compound. Several studies have shown that the oxygen vacancies may induce charge transition levels within the bandgap (intragap), typically enhancing the carrier density and promoting charge separation for metal oxide semiconductors.[97,103-104] As previously noted, the existence of oxygen vacancies/defects is a significant indicator of V^{5+}/V^{4+} oxidation states in the electronic structure of BVO.

XPS is also a powerful tool for determining the position of the valence band (VB) relative to the Fermi level. This information is useful for understanding the electronic structure of materials. Hence, XPS was further employed to investigate the valence band composition of bare BVO film. As shown in Figure 21d, deconvolution of the VB spectrum produces four photoemission components between 9 and 2 eV, with an isolated feature around 12 eV. RIXS analysis and DFT calculations performed by Cooper *et al.*[73] have revealed that these peaks are directly associated with (i) unhybridized O $2p_\pi$ orbitals mixed with Bi 6s states at ~2.44 eV, (ii) O $2p_\pi$ states at ~3.69 eV, (iii) O sp^2/V 3d hybridized states at ~5.49 eV, (iv) O sp^2/Bi 6p

hybridized states at ~7.18 eV, and (v) Bi 6s states at ~12.18 eV. As a result, the VB edge of BVO is mainly composed of Bi 6s and O 2p states, corroborating with Figure 12c. Furthermore, since these energies are measured relative to the Fermi energy of $BiVO_4$, the linear extrapolation of the leading edge of the VB with zero baseline intensity gives the distance between the VB edge and the Fermi energy of the semiconductor.[58,75,105] As shown in the inset of Figure 21d, $E_V - E_F$ is 1.72 eV for the BVO film, which combined with the bandgap energy of ~2.58 eV clearly evidences the n-type nature of BVO (E_F located near to the CB edge).

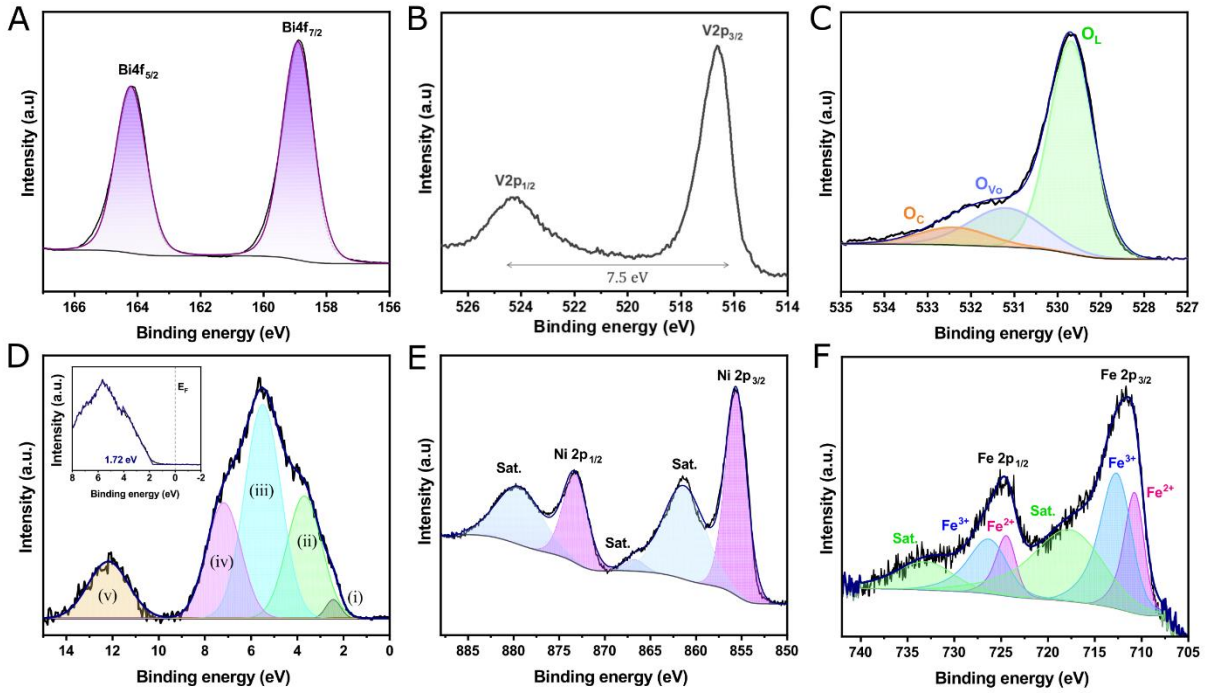

Figure 21 – XPS spectra of bare BVO film deposited in 8 minutes and annealed at 400° C for 1 hour: (a) Bi 4f, (b) V 2p, (c) O 1s, (d) VB spectra. XPS spectra of as-sputtered BVO/$FeNiO_x$ with $FeNiO_x$ deposited for 60 seconds: (e) Fe 2p and (f) Ni 2p.
Source: By the author.

XPS was also employed to characterize the chemical surface composition of the as-deposited $FeNiO_x$ ultrathin layer on the surface of BVO films. Figure 21e shows the Ni 2p XPS spectra of $FeNiO_x$, clearly exhibiting a doublet with components at 855.6 and 873.2 eV, corresponding to the Ni^{2+} oxidation state. Additionally, the presence of two more intense satellite peaks around 861.3 and 879.3 eV also indicates the presence of Ni^{2+} states in the $FeNiO_x$ structure.[108] As shown in Figure 21f, the Fe $2p_{1/2}$ and Fe $2p_{3/2}$ peaks of Fe 2p reveal the presence of Fe^{3+} and Fe^{2+} oxidation states in the $FeNiO_x$ structure. The characteristic peaks at 712.5 and 726.1 eV correspond to Fe^{3+}, whereas the two splitting peaks at 710.6 and 724.3 eV are associated with Fe^{2+}.[103] Furthermore, the peaks at 717.3 and 732.7 are ascribed to the typical

satellite peaks of Fe 2p.[106,107] Therefore, these results unambiguously confirm that the $FeNiO_x$ bimetallic oxide was successfully coated on the surface of the BVO film.

4.1.3 Photoelectrochemical properties

The PEC performance of all photoelectrodes was evaluated in a 1 M potassium borate buffer (KBi, pH 9.5). Figure 22a shows the current density vs. applied potential (j-V) curves (under constant 100 mW cm^{-2} AM 1.5G illumination) for the bare BVO films deposited in 6, 8, 10, and 12 minutes and annealed at 400 °C for 1 hour. All BVO films exhibited anodic photocurrents when polarized in the reverse direction, evidencing their n-type semiconducting nature. Among these photoanodes, the BVO deposited in 8 minutes showed the highest PEC performance, reaching 0.72 mA cm^{-2} in the water oxidation potential (1.23 V vs. RHE). Remarkably, the slight variation in photocurrent densities as a function of film thickness is due to the compromise between light absorption and charge recombination. While the 6-minute film is not thick enough to absorb all incident photons with $E > E_G$, the 12-minute film has a large thickness at which the charge recombination process is dominant. In contrast, the 8- and 10-minute films represent the situation in which the light is efficiently absorbed, and the photogenerated electrons and holes have a smaller mean free path for reaching the surface of the back contact and electrolyte, respectively. Due to its higher PEC performance, the 8-minute film was chosen for future characterizations and modification with the $FeNiO_x$ cocatalyst.

Importantly, all BVO photoanodes showed a significant residual peak around 0.4 V vs. RHE, which has been associated to the production of surface peroxide species (chemical compounds that contain peroxide ions O_2^{2-}).[103,109,110] These peroxide species are typically formed during oxidation reactions in the presence of oxygen or oxygen intermediates (such as PEC water splitting) and can participate in several chemical reactions such as OER and hydrogen peroxide reduction, thereby increasing the photocurrent density of the BVO film. As a consequence, although the presence of excess peroxide species elevates the PEC activity of the BVO film, a significant part of this photocurrent density is attributed to chemical reactions not directly associated with oxygen evolution (resulting in a photoconversion efficiency of photogenerated holes into oxygen molecules much less than 100%).

To investigate the behavior of this residual peak, we measured the j-V curve of the optimized BVO film by sweeping the applied potential from 0.1 V (notice that the first measurements were started at -0.03 V). As shown in Figure 22b, the residual peak is significantly reduced when starting at $+0.1$ V, indicating a lower production of peroxide

species. In this case, the behavior of the j-V curve is drastically altered, exhibiting lower photocurrents at all applied potentials. Therefore, our findings show that starting the potential at 0.1 V is insufficient to fully activate the formation of surface peroxide species, justifying the lower photocurrent densities. Importantly, STH efficiencies of around 100% have been reported for BVO-based photoanodes with small residual peaks at ∼0.4 V vs. RHE.[103] As a result, we attributed the current density without intense peaks in Figure 22b as mainly caused by water oxidation reactions. In this case, the OER photocurrent density of our BVO film drops to 0.52 mA cm^{-2} at +1.23 V, and the onset potential of water oxidation is ∼0.45 V. Henceforth, all PEC properties of bare BVO were measured with films polarized from +0.1 V.

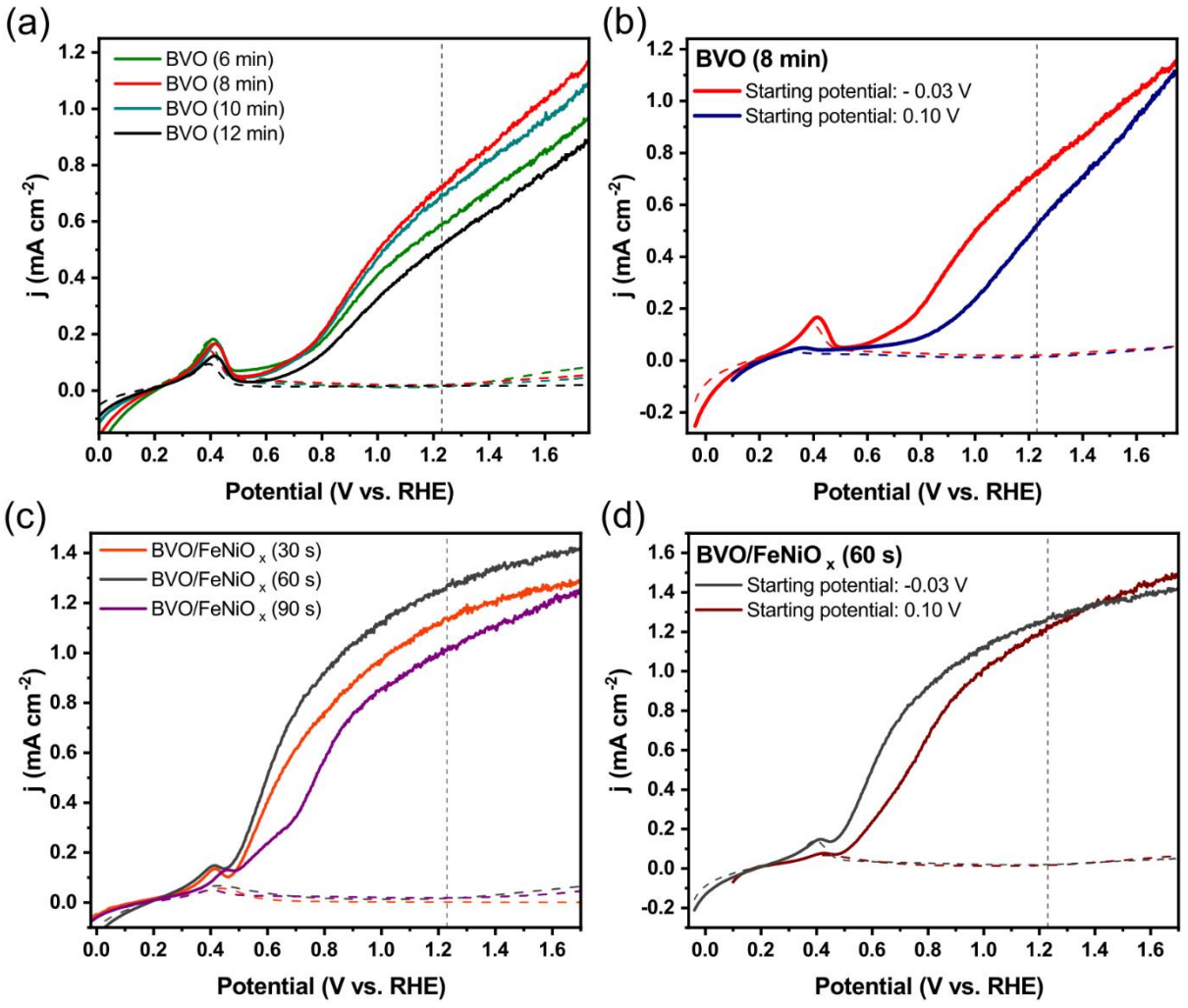

Figure 22 – (a) j-V curves for bare BVO films deposited in 6, 8, 10, and 12 minutes and annealed at 400° C for 1 hour. (b) Comparison between the j-V curves starting at −0.03 V and 0.1 V vs. RHE for the optimized BVO film (8 minutes). (c) j-V for BVO/$FeNiO_x$ with $FeNiO_x$ deposited for 30, 60, and 90 seconds. (d) Comparison between the j-V curves starting at −0.03 V and 0.1 V vs. RHE for the optimized BVO/$FeNiO_x$ film (60 seconds of $FeNiO_x$).

Source: By the author.

To suppress charge recombination and accelerate the surface chemical reaction kinetics, we deposited the $FeNiO_x$ cocatalyst (30, 60, and 90 seconds) on the surface of the BVO films. As shown in Figure 22c, all resulting BVO/$FeNiO_x$ photoanodes produce high photocurrent densities at low applied potentials, a signature of the cocatalyst effect.[58,98,111-112] Deposition of $FeNiO_x$ for 60 seconds clearly produces the photoanode with the highest PEC performance, reaching 1.27 mA cm^{-2} in water oxidation potential. The lower catalytic activity of the 30-second $FeNiO_x$ condition is likely associated with the low production of a few active sites for the OER. In contrast, a longer 90-second deposition can lead to the formation of recombination centers at the BVO/$FeNiO_x$ interface, lowering the photocurrent density. Similar to the bare BVO films, all BVO/$FeNiO_x$ photoanodes showed an intense signal at ~ 0.4 V related to the production of peroxide species. Figure 20d shows the comparison of j-V curves for optimized BVO/$FeNiO_x$ (60 seconds of $FeNiO_x$) starting from -0.03 V (condition I) and 0.1 V (condition II). In condition II, the residual peak is drastically reduced, implying a lower production of peroxide species; that is, photogenerated holes are mostly used in water oxidation. However, the photocurrent generated at low applied potentials in condition II is significantly reduced compared to the condition I. This indicates that the photocurrent density in condition I is inflated due to the formation of peroxide species and their subsequent chemical reactions. Therefore, all subsequent BVO/$FeNiO_x$ characterizations were performed with the initial bias at 0.1 V.

Figure 23a shows the final j-V curves of bare BVO and BVO/$FeNiO_x$ photoanodes, clearly showing that the onset potential of water oxidation of bare BVO is cathodically shifted to 0.38 V after $FeNiO_x$ deposition, indicating enhanced charge separation efficiency in low applied potential range.[58,98,113] Furthermore, the photocurrent density of BVO/$FeNiO_x$ (1.22 mA cm^{-2}) is 2.3-fold higher than that of bare BVO at water oxidation potential. To further investigate the enhanced PEC performance of the surface-modified BVO film, the ABPE curves of the BVO and BVO/$FeNiO_x$ were determined using equation (26). As shown in Figure 23b, the bare BVO film exhibits an ABPE peak of only 0.05 % at around 1.03 V vs. RHE, whereas the ABPE peak of the BVO/$FeNiO_x$ reaches a significant increase of 0.30 % at a lower applied potential (0.85 V vs. RHE). The excellent PEC performance of the BVO/$FeNiO_x$ in the low applied bias clearly opens the possibility of using this film as a photoanode in a Tandem cell.

To investigate the influence of light absorption on enhanced PEC performance of the surface-modified BVO films, we measured their IPCE values under +1.23 V vs. RHE. As shown in Figure 23c, the bare BVO and BVO/$FeNiO_x$ photoanodes have a photoactive response in the $300 - 505$ nm range, consistent with a bandgap of $\sim 2.4 - 2.6$ eV for the monoclinic phase of $BiVO_4$. The IPCE values of the bare BVO film are lower than 6.8 % in the entire

photocurrent responsive range. After depositing $FeNiO_x$, the IPCE values are significantly boosted to a maximum of ~14.7 %. It is crucial to emphasize that the improved solar-to-current conversion of BVO/$FeNiO_x$ is mainly attributed to the reduction of surface charge recombination. To investigate the charge transfer kinetics at the BVO-based/electrolyte interface, we performed EIS at +0.90 V vs. RHE under constant AM 1.5G illumination. As shown in Figure 23d, the Nyquist plots of bare BVO and BVO/$FeNiO_x$ exhibit only a single semicircle, which can be simulated from the equivalent circuit (inset) characterized by a series resistance (R_S), charge transfer resistance (R_{CT}) at the photoanode/electrolyte interface and a constant phase element (CPE) to describe the double-layer capacitance for the inhomogeneous electrode surface.[114] Remarkably, the calculated R_{CT} for BVO/$FeNiO_x$ (0.55 kΩ) is significantly lower than that of bare BVO (6.35 kΩ), clearly indicating that $FeNiO_x$ enhances interfacial charge separation and increases the solar-to-current efficiencies.

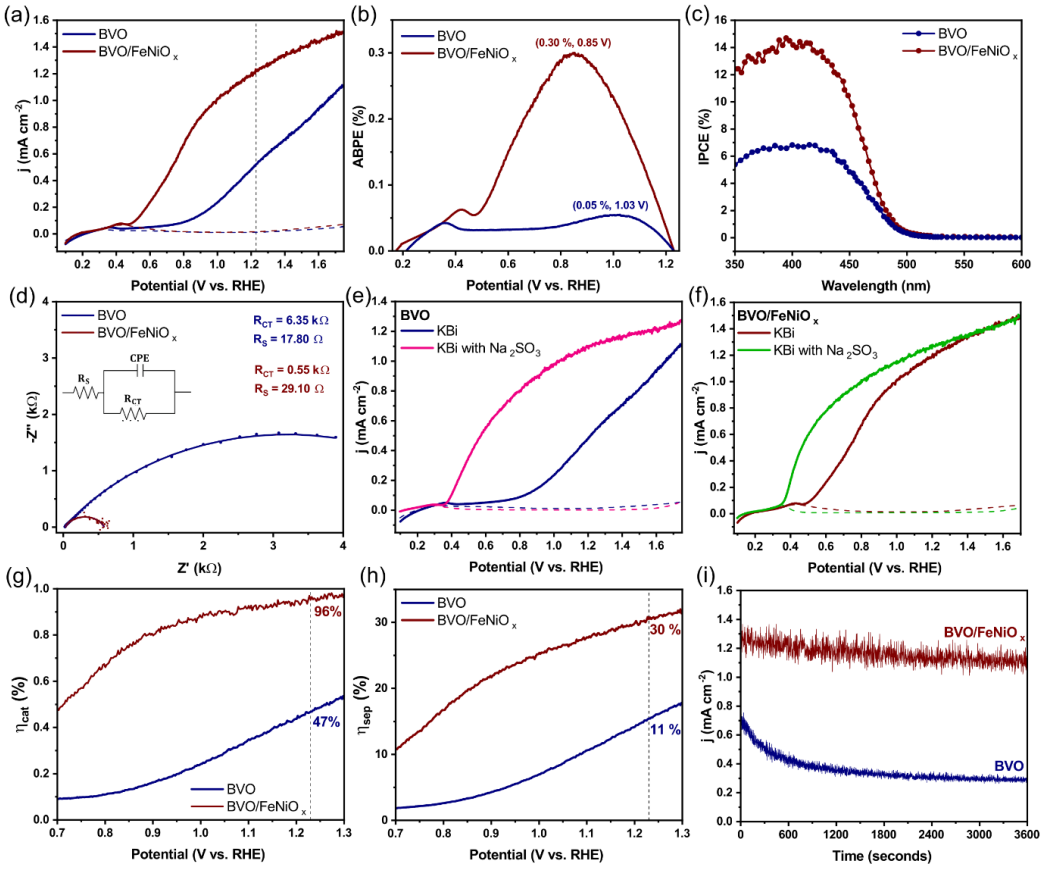

Figure 23 – PEC performance of optimized BVO and BVO/$FeNiO_x$ films. (a) j-V curves; (b) ABPE curves; (c) IPCE curves obtained at +1.23 V vs. RHE; (d) EIS response measured under 0.90 V vs. RHE and (inset) the equivalent Randles circuit model; j-V curves for (e) BVO and (f) BVO/$FeNiO_x$ in 1 M KBi buffer (pH 9.5) with and without hole scavenger species (0.25 M Na_2SO_3); (g) charge transfer efficiencies and (h) charge separation efficiencies at different applied potentials; (i) temporal stability by chronoamperometry measurements under +1.23 V vs. RHE.

Source: By the author.

To further unravel the charge-transfer and separation properties on the BVO/$FeNiO_x$ films, we decoupled the photocurrent density (j) from the PEC measurements into three significant contributions: $j = j_{abs} \times \eta_{cat} \times \eta_{sep}$ (see experimental section). The values of j_{abs} for bare BVO and BVO/$FeNiO_x$, calculated from equation (27), are 3.38 and 4.00 mA cm^{-2}, respectively. To assess the charge separation (η_{sep}) and interfacial transfer efficiencies (η_{cat}), we performed the PEC measurements with 1 M KBi plus 0.25 M Na_2SO_3 (pH 9.5). As shown in Figures 23e and 23f, the Na_2SO_3 species exhibits fast kinetics for consuming photogenerated holes at the semiconductor-electrolyte interface ($\eta_{cat} \sim 1$), resulting in higher photocurrent density values. Furthermore, note that the onset potential for the BVO and BVO/$FeNiO_x$ photoanodes suffers a new cathodic shift, approaching the flat band potential (~0.30 V, section 4.1.4) as the overpotential for oxidation reactions tends to zero. Figures 23g and 23h show the calculated efficiencies as a function of the applied potential. For the bare BVO photoanode, both η_{cat} and η_{sep} rise from small values under low applied potentials to ~47.0 and ~11 %, respectively, at +1.23 V vs. RHE. Encouragingly, our BVO/$FeNiO_x$ photoanode drastically enhances the charge transfer efficiency, reaching ~96 % at +1.23 V vs. RHE. In addition, the separation efficiency was also improved under low applied bias, reaching ~30 % at +1.23 V vs. RHE. These significant results indicate that the $FeNiO_x$ has an excellent activity for separating photogenerated charges (driven by a built-in electric field, discussed in section 4.1.4) and consuming the photogenerated holes from the BVO layer, thereby reducing the onset for water oxidation and enhancing the PEC performance.

The PEC stability of bare BVO and BVO/$FeNiO_x$ photoanodes was evaluated through chronoamperometry measurements (j-t curves). It is crucial to emphasize that the chemical stability of the photoanode during the harsh conditions for OER is one of the main challenges for constructing Tandem cells aiming at practical applications. Figure 23i shows the j-t curves for the BVO-based photoanodes submitted to 1.23V vs. RHE and AM 1.5G illumination for 1 hour. The bare BVO film exhibits modest chemical stability in the 1 M KBi buffer at pH 9.5, retaining ~ 40.5 % of its initial value during 1 hour. The chemical instability of BVO photoanodes in the presence of potassium borate species at pH 9.5 is probably attributed to significant photocorrosion of the BVO layer during the PEC water oxidation.[75,103] In contrast, the BVO/$FeNiO_x$ films exhibit superior PEC stability, retaining ~ 90.0 % of its initial photocurrent density during 1 hour. This remarkable result indicates that the deposition of $FeNiO_x$ bimetallic oxides also protects the BVO layer from photocorrosion, consistent with previous research concerning BVO/$FeMO_x$ (M = Co, Ni, Mn) heterojunctions.[58,75,98,103] In

summary, our results evidence that the all-sputtered BVO/$FeNiO_x$ photoanode is a very promising candidate for driving OER in a Tandem cell because it produces high photocurrent densities at low applied potentials and enhances the chemical stability of the BVO during the water oxidation reaction.

4.1.4 Interfacial band alignment and charge transport properties

To provide solid insights into the interfacial band alignment and charge transfer process in the BVO/$FeNiO_x$ photoanode, we started by constructing the energy band diagrams of the isolated semiconductors from UV-vis spectroscopy and Mott-Schottky (MS) analysis. In particular, the Mott-Schottky curves were measured in the dark condition (under 1 kHz) to estimate the semiconductors' flat band potential and impurity concentration. As shown in Figure 24a, the MS curve for the bare BVO film exhibits a straight line with a positive slope, characteristic of n-type semiconductors, resulting in a flat band potential (E_{FB}) of 0.26 V vs. RHE and donor concentrations (N_D) of 1.1×10^{19} cm^{-3}. Interestingly, our BVO/$FeNiO_x$ film showed a noticeable shift of the flat band potential towards more positive energies compared to bare BVO, which is a characteristic signature when forming a p-n heterojunction.[58,75,98] To confirm the development of a p-n heterojunction, we deposited bare $FeNiO_x$ (under the same conditions to synthesize BVO/$FeNiO_x$) on an FTO substrate. The MS curve of the bare $FeNiO_x$ film (Figure 24b) shows a straight line with a negative slope, evidencing its p-type semiconducting nature. According to equation (23), the flat band potential and impurity concentration for the bare $FeNiO_x$ film are ~ 1.16 V vs. RHE and 1.9×10^{21} cm^{-3}, respectively. As a result, contact between the n-BVO and p-$FeNiO_x$ semiconductors certainly induces local p-n heterojunctions.

To estimate the energy band diagram of the n-type semiconductor, we assumed that the difference between the flat band energy (Fermi energy of the semiconductor in contact with the electrolyte) and the CB edge is ~ 0.2 eV.[115-116] Similarly, the difference between the flat band energy and the VB edge was estimated to be ~ 0.2 for the p-type semiconductor. We used this approach due to the following considerations: (i) BVO and $FeNiO_x$ films have a high concentration of impurities in such a way that equations (11) and (12) are not valid; that is, the Fermi Dirac distribution cannot be simplified to Boltzmann distribution in these semiconductors, and (ii) the band diagram calculated with the VB XPS of the BVO suggests that the distance between the Fermi energy and the CB edge is ~ 0.86 eV, which is inconsistent

for semiconductors with high doping.[75] Furthermore, this last approach suggests that the CB edge value for the bare BVO is around -0.6 eV vs. RHE, in discrepancy with the well-established value of ~ 0 eV vs. RHE. Figure 24c shows the band diagrams of the isolated semiconductors, considering $E_{FB} \approx E_F$ and using the bandgap values calculated by UV-vis spectroscopy (2.58 eV for BVO and 2.32 eV for $FeNiO_x$, see Figure 24b).[58,75,117] Remarkably, our flat band energy diagrams clearly indicate the formation of a type II heterojunction (staggered bands) at the n-BVO/p-$FeNiO_x$ interface, which has been considered a very beneficial interfacial alignment for PEC applications.[58,118]

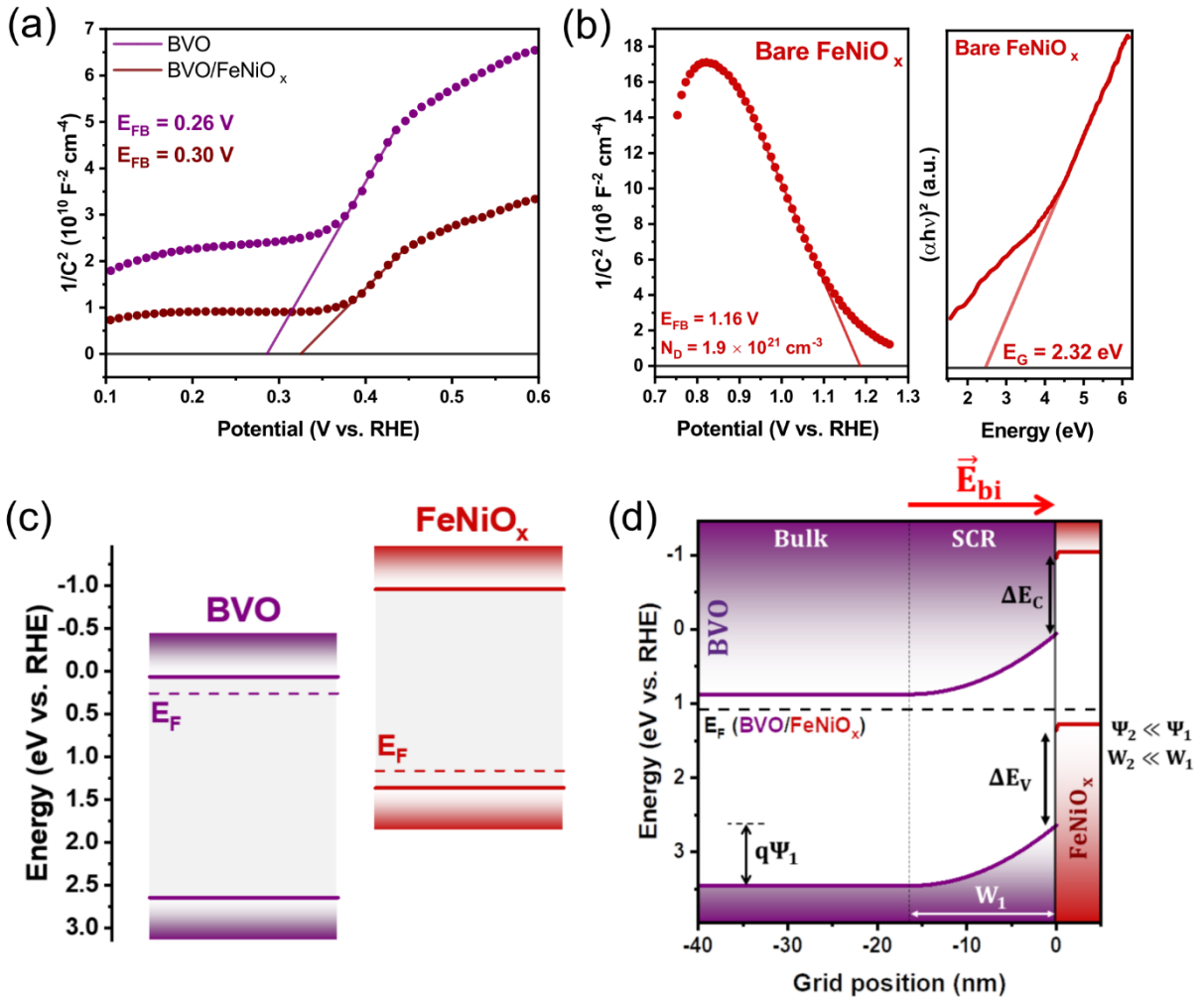

Figure 24 – (a) MS curves for optimized BVO and BVO/$FeNiO_x$ films; (b) MS curve and Tauc plot analysis for bare $FeNiO_x$ film; (c) isolated flat band diagrams of bare BVO and $FeNiO_x$ semiconductors constructed by MS analysis and UV-vis spectroscopy; (d) interfacial band alignment of BVO/$FeNiO_x$ p-n heterojunction under dark condition.
Source: By the author.

Furthermore, according to the classical band theory, an interfacial space charge layer (SCR) appears immediately after contacting the n-type and p-type semiconductors. In the dark

condition, electrons of the n-type layer are preferentially diffused (driven by the electrochemical potential gradient) to the p-layer. At the same time, p-type holes tend to diffuse into the n-layer. The diffusion of electrons and holes continues until the Fermi energy becomes a constant throughout the material (representing net zero current flow across the p-n heterojunction).[36,58,91] After equilibrium, the p-n heterojunction interface is characterized by the band bending phenomena and the development of a built-in electric field that points from the n-layer to the p-layer. Neglecting the surface states (excellent approximation due to the simple RC circuit for the Nyquist plot of BVO/FeNiO$_x$ heterojunction under dark), the VB and CB edges of the semiconductors are fixed at the p-n interface (band edge pinning phenomena). In contrast, the energy bands in bulk move along with the Fermi energies, modulating the band bending intensities and directions. Figure 24d depicts the interfacial band alignment of the BVO/FeNiO$_x$ heterojunction constructed from the classical band bending model (see experimental section) under dark conditions, clearly capturing the abovementioned physics. Importantly, the as-developed SCR is defined by (i) the potential drops $\Psi_1 = 0.87$ V and $\Psi_2 =$ 27 mV supported in the *n* and *p* layers, respectively, (ii) the depletion lengths $W_1 = 23.8$ nm and $W_2 = 1.4$ Å in the corresponding layers, (iii) the built-in electric field that points from the *n* to the *p* side, and (iv) the constant Fermi energy at 1.13 eV vs. RHE throughout the p-n heterojunction. Our BVO/FeNiO$_x$ heterojunction has an SCR entirely concentrated on the BVO side due to the higher impurity concentration in the bimetallic oxide ($N_A \gg N_D$).

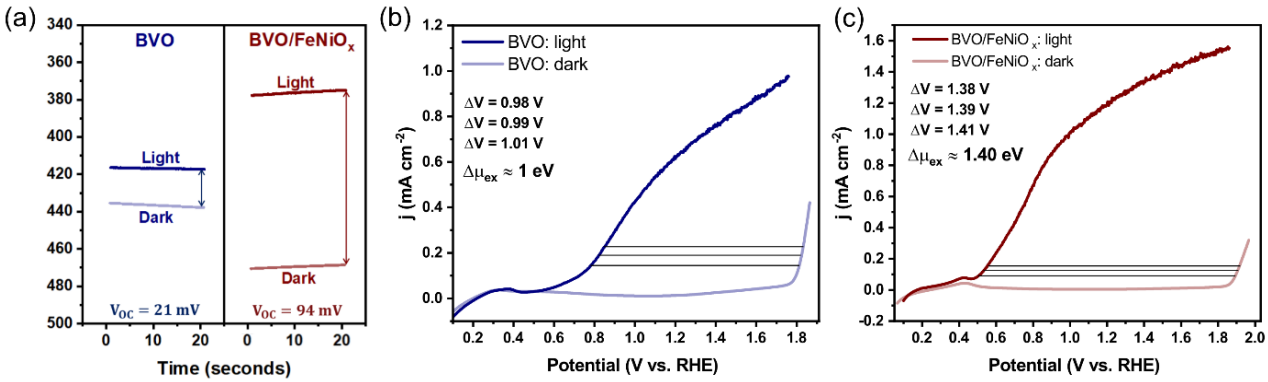

Figure 25 – (a) OCP potentials under dark and AM 1.5 illumination for BVO and BVO/FeNiO$_x$ films. Determination of $\Delta\mu_{ex}$ for (b) BVO and (c) BVO/FeNiO$_x$ photoanodes by comparing the j-V curves under dark and AM 1.5 illumination.
Source: By the author.

To provide solid insights into the effect of 1.5G AM illumination on our BVO-based films, we estimated the values of photovoltage (V_{ph}) and free energy stored in electron-hole pairs ($\Delta\mu_{ex}$) from PEC measurements. In analogy with the SCLJ (section 2.2), illumination

splits the dark Fermi energy into QFL for electrons and holes, whose separation at the p-n (or SCLJ) interface provides the free energy stored in the electron-hole pairs available for performing work.[42,119] Furthermore, illumination acts as a slight forward bias, reducing the band bending of the SCLJ or p-n heterojunction (band flattening) and lowering the dark Fermi energy for electrons $\left(qV_{ph} = |E_{Fn} - E_{F,dark}|\right)$. In our following analyses, we will consider that only the BVO layer is responsible for absorbing light and producing electron-hole pairs.

It is well known that the photovoltage can be estimated by comparing the open circuit potentials (V_{OC}) under dark and illumination, i.e., $V_{ph} = |V_{OC}^{dark} - V_{oc}^{light}|$.[18,32] Figure 25a shows that the bare BVO film exhibits a small photovoltage of only 21 mV. In contrast, the photovoltage developed in the BVO/FeNiO$_x$ has significantly boosted to ~ 94 mV, evidencing that the formation of the p-n heterojunction employs the available free energy $\Delta\mu_{ex}$ more efficiently for the OER reaction (recall that $a_{ph} = qV_{ph} - \Delta\mu_{ex}$ is associated with entropic losses due to the slow water oxidation kinetics). Furthermore, as shown by Miao *et al*., the value of $\Delta\mu_{ex}$ can be estimated from straightforward PEC measurements.[42] Briefly, $(\Delta\mu_{ex}/q)$ is defined by the potential difference between points on the j-V curves that produce the same current density under dark and illumination. This relationship can be demonstrated by examining the band diagrams associated with the production of an arbitrary photocurrent (j_{arb}) under applied potentials of V_{dark} and V_{light} for dark and light conditions, respectively. Due to the development of $\Delta\mu_{ex}$, $V_{light} \ll V_{dark}$ is typically required to attain j_{arb}, such that $\Delta\mu_{ex} = V_{dark} - V_{light}$. In this context, Figures 25b and 25c show that the $\Delta\mu_{ex}$ value for bare BVO is around 0.90 eV, while the BVO/FeNiO$_x$ heterojunction shows a higher $\Delta\mu_{ex}$ of around 1.40 eV. As a result, the p-n BVO/FeNiO$_x$ film gives rise to electron-hole pairs with higher Helmholtz free energy for OER reactions. Note, however, that these estimated $\Delta\mu_{ex}$values are much smaller than those considered for Bolton's method ($\Delta\mu_{ex} \approx 0.75E_G \approx 1.93$ eV),[19,43] indicating that the slow water oxidation kinetics is still a significant limitation for our BVO-based photoanodes.

Figure 26a shows the energy band diagram of BVO in contact with the KBi electrolyte (pH 9.5) under dark conditions. In this case, the electrochemical potential of the aqueous solution (between 0 V and 1.23 V) must align with the Fermi energy of the BVO layer. As a result, the open-circuit potential (OCP) in the dark ($qV_{OC}^{dark} = E_{dark} \approx 0.44$ eV) provides the equilibrium value of the electrochemical potentials of the semiconductor and liquid phases, measured in reference to the RHE scale.[42] Therefore, Figure 26a was constructed by assuming that all potential drop in the BVO/KBi interface occurs over BVO side (i.e., $q\Psi_1 = E_{F1} -$

$E_{dark} = q\Psi_{bi}$), resulting in $\Psi_1 = 0.18$ V and $W_1 = 11.08$ nm. The effect of AM 1.5G illumination on the BVO/KBi interface is shown in Figure 26b. It shows the qualitative splitting of the dark Fermi energy in QFL for electrons and holes, whose separation at the SCLJ interface is given by $\Delta\mu_{ex} \approx 0.9$ eV, as well as the flattening band phenomenon caused by the photovoltage, which lowers the SCR ($\Psi_1^{light} = \Psi_1 - V_{ph}$ and $W_1^{light} = 10.42$ nm) and slightly decreases the Fermi energy of the electrons by $qV_{ph} =$ 21 meV. Remarkably, the estimated QFL of holes in the SCLJ $(E_{Fp} \approx 1.32$ eV$)$ is higher than +1.23 eV vs. RHE, indicating that photogenerated holes in the VB of the BVO have enough energy to oxidize H_2O in O_2.

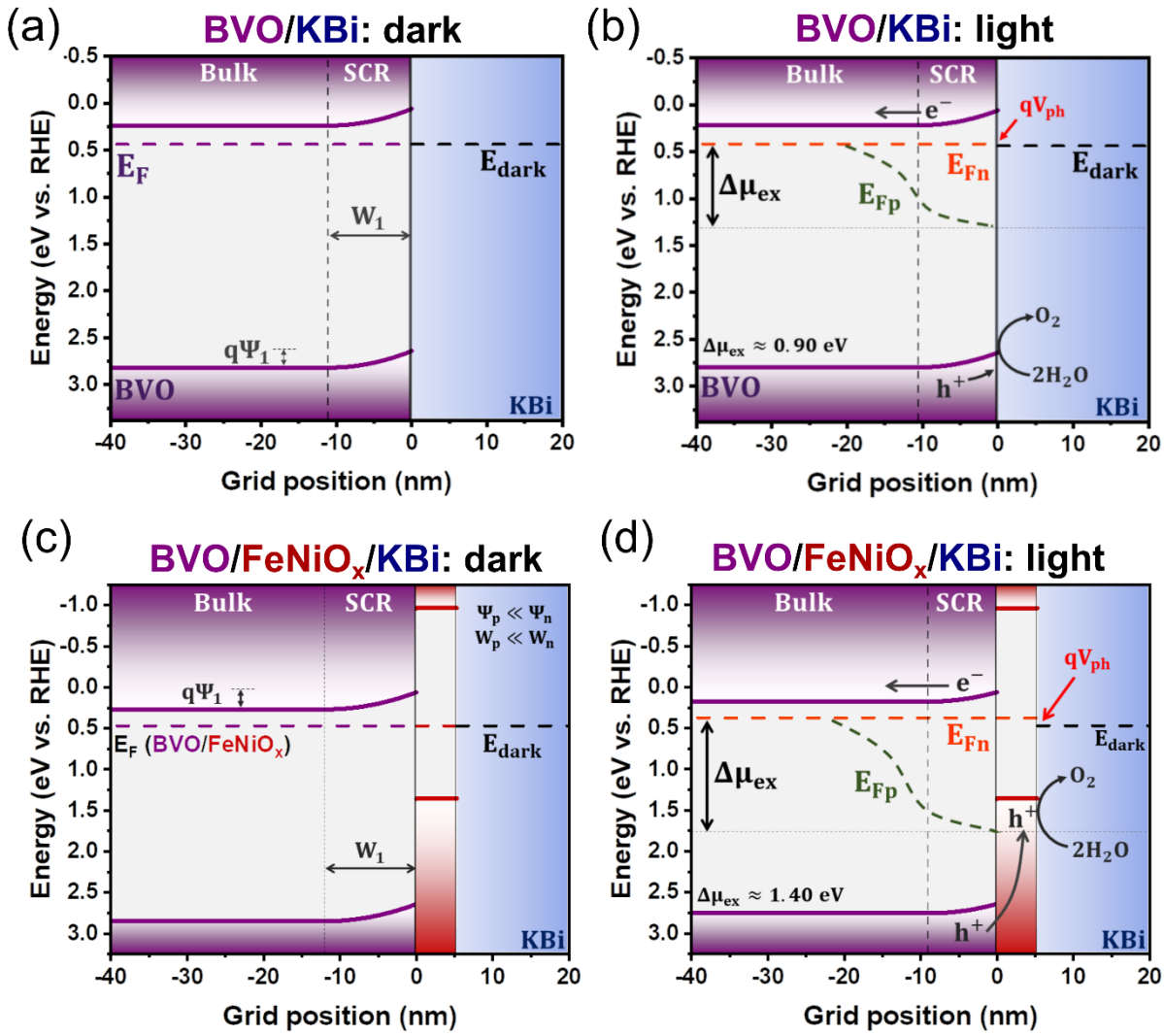

Figure 26 – Estimated interfacial band alignment for (a) BVO/KBi under dark conditions, (b) BVO/KBi under AM 1.5G illumination, (c) BVO/$FeNiO_x$/KBi under dark conditions, and (d) BVO/$FeNiO_x$/KBi under AM 1.5G illumination.
Source: By the author.

Similarly, Figure 26c shows the interfacial band alignment of our BVO/$FeNiO_x$ heterojunction under dark conditions. In this case, the electrochemical potential of the

BVO/FeNiO$_x$ and KBi phases must align with the (dark) open-circuit potential ($qV_{OC}^{dark} = E_{dark} \approx 0.47$ eV). As a result, the BVO/FeNiO$_x$/KBi interfacial structure was simulated by determining the forward bias (from classical band model) that aligns the Fermi energy of the BVO/FeNiO$_x$ heterojunction with the E_{dark} (compare Figures 24d and 26c). When the electrochemical potentials are finally aligned, a pronounced SCR takes place at the BVO/FeNiO$_x$ interface (entirely concentrated on the BVO side), characterized by a built-in electric field that points from the BVO to the FeNiO$_x$ layers, a potential drop $\Psi_1 = 0.26$ V and depletion length $W_1 = 11.97$ nm. The effect of 1.5G AM illumination on the BVO/FeNiO$_x$ heterojunction is shown in Figure 26d, clearly showing the flattening band phenomenon caused by the photovoltage of 94 meV ($\Psi_1^{light} = 0.12$ V and $W_1^{light} = 8.90$ nm) and the qualitative splitting of dark Fermi energy in the QFL for electrons and holes, whose separation at the p-n interface corresponds to the free energy $\Delta\mu_{ex} = 1.4\ eV$ stored in the electron-hole pairs.

Therefore, our band diagram shows that the photogenerated holes in the VB of the BVO are accelerated by the built-in electric field towards the FeNiO$_x$ layer, where the OER reactions occur more efficiently (due to the cocatalyst effect). In contrast, the photogenerated electrons in the CB of BVO are directed by the built-in electric field toward the FTO substrate. It is essential to emphasize that the QFL for the holes at the p-n interface ($E_{FP} \approx 1.80$ eV) is much more positive than the water oxidation potential (and also more positive than E_{Fp} in the SCLJ for bare BVO), thereby producing photogenerated holes with suitable energy to overcome the energetic requirements and overpotentials for OER. Furthermore, due to the type II heterojunction (staggered band alignment), the ΔE_C potential barrier (see Figure 24d) provides a mechanism that prevents the flow of electrons from BVO to the FeNiO$_x$ layer, suppressing electron-hole recombination. As a result, the charge separation and interfacial transfer efficiencies are significantly increased when forming the BVO/FeNiO$_x$ heterojunction due to the presence of a built-in electric field (which efficiently directs the charges) and cocatalyst effect, respectively. These results corroborate our PEC measurements and suggest that the BVO/FeNiO$_x$ heterojunction is a promising photoanodic candidate for OER in a Tandem cell, producing sufficient free energy and photovoltage for the water oxidation reaction without applying external potentials.

4.2 Development of CuO-based photoanodes

In this work, we produced CuO films from magnetron sputtering deposition (with a Cu metallic target) followed by annealing for use as a photocathode in a Tandem cell. To optimize our CuO films for HER, we varied the deposition time (i.e., thickness) between 5, 10, 20, and 30 minutes. It is well known that as-sputtered Cu film converts to Cu_2O at ~ 200 °C, and a further phase transition to CuO occurs at ~ 350 °C.[82,120-121] Thus, our as-sputtered Cu films were subjected to a fixed thermal treatment at 550 °C for 8 hours to obtain the desired crystalline phase. Although exhibiting excellent PEC performance, the all-sputtered CuO films showed severe photodegradation under (high) applied reverse bias, reducing to Cu_2O during chronoamperometric measurements. In this context, future works should be dedicated to producing protective layers and inducing p-n heterojunctions for CuO films. The following sections will discuss the morphological, structural, optical, electronic, PEC, and interfacial band alignment properties of our CuO photocathodes.

4.2.1 Structural and morphological properties

XRD and Raman spectroscopy were employed to investigate the influence of increasing the thickness on the crystallinity of the CuO films. Figure 27a shows the XRD patterns for the CuO films that were deposited in 5, 10, 20, and 30 minutes and annealed at 550 °C for 8 hours. All films showed intense diffraction peaks at 35.6° and 38.8°, corresponding respectively to the (002) and (110) planes of monoclinic CuO (JCPDS no. 48-1548). Similar to the BVO, increasing thickness significantly increases the intensity of diffraction peaks, which is expected as thicker films have more atomic layers to diffract X-rays. This behavior also explains why diffraction peaks at 32.6° and 48.9° start to become visible for the 20 and 30-minute films; for low thicknesses, the low-intensity peaks of CuO are superimposed by the measurement noise. Importantly, no impurities or secondary crystalline phases exist in the XRD patterns for all CuO films, evidencing that the as-sputtered Cu films were successfully converted to monoclinic CuO following annealing.

Conclusively, Figure 27b shows the Raman spectra for these as-annealed Cu films, showing three absorption bands that are characteristic signatures of monoclinic CuO. It is well known that CuO has 12 vibrational modes due to the presence of four atoms in the primitive cell. Group theory and semi-empirical calculations show that these vibrations comprise (i) three

acoustic modes with A_u + $2B_u$ symmetry and (ii) nine optical modes (zone-center) with $4A_u+5B_u+A_g+2B_g$ symmetry; however, only three of these symmetry modes (A_g+2B_g) are Raman active.[122–124] Notably, the three vibrational bands at around 290, 338, and 624 cm^{-1} are associated with the A_g, B_{1g}, and B_{2g} modes, respectively, associated with the movement of oxygen atoms in the CuO structure. Additionally, there are no significant differences among the Raman spectra for our CuO photocathodes, indicating that all films are properly crystallized and that the intensification of XRD peaks is directly related to their thickness rather than with higher crystallization.

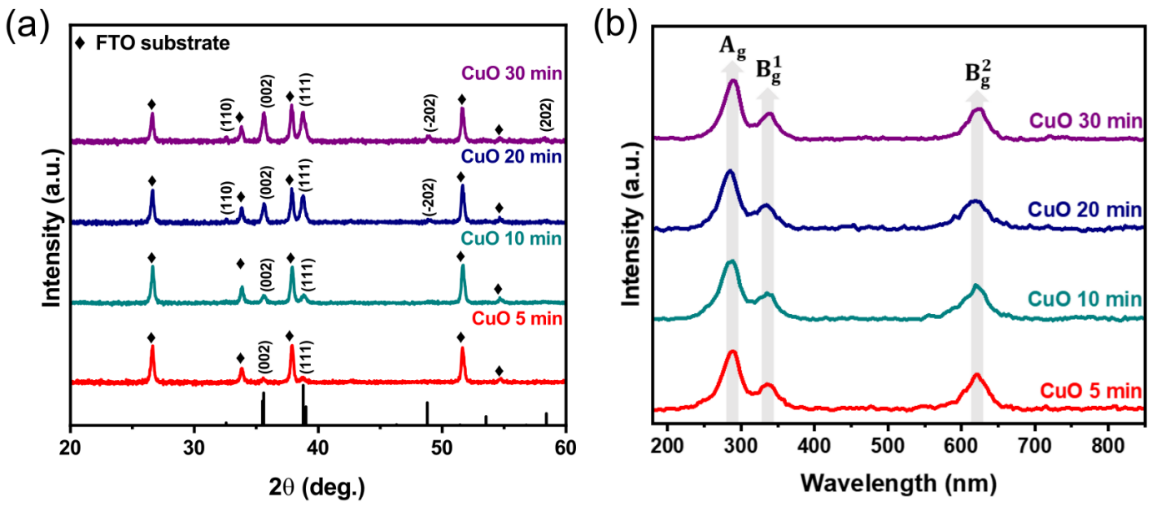

Figure 27 – (a) XRD patterns and (b) Raman spectra for CuO films deposited in 5, 10, 20, and 30 minutes and annealed at 550° for 8 hours.
Source: By the author.

The top-view SEM images of our CuO films are shown in Figure 28. Interestingly, the CuO film deposited in 5 minutes comprises several clusters of small uniform particles (with an average size of ~ 40 nm). This behavior is expected for sputtering depositions, where high-energy Cu atoms are initially nucleated in the substrate and diffuse until they reach a position that minimizes their total energy. With increasing deposition time and thermal treatment, these mobile Cu atoms are converted into CuO particles that combine in larger nucleated particles, originating mobile islands that tend to coalesce and generate a continuous film.[80,95,125] As shown in Figure 28, the agglomerated CuO particles progressively coalesce in a more compact and denser structure, and the average particle size slightly grows by increasing the deposition time.

Furthermore, it is essential to note that the 20-minute film has several pinholes, which is expected due to the contact between the various mobile CuO islands. In contrast, the 30-minute film shows the formation of a compact and dense layer with a significantly smaller number of holes. Indeed, it is well known that these pinholes tend to be shrunken with

increasing deposition, thereby producing more continuous films.[95] Therefore, our SEM results suggest that the higher intensity of XRD peaks is due to the production of larger agglomerates of CuO particles, originating more C-O bonds and providing more crystalline planes for X-ray diffraction. Additionally, Figure 28e exhibits the cross-sectional SEM image of the CuO film deposited for 10 minutes and calcined at 550 °C for 8 h. The image clearly reveals a compact and thick layer of CuO (~450 nm) coating the FTO surface. Importantly, this measured thickness coincides well with the deposition rate of ~ 50 nm min^{-1} estimated by profilometry.

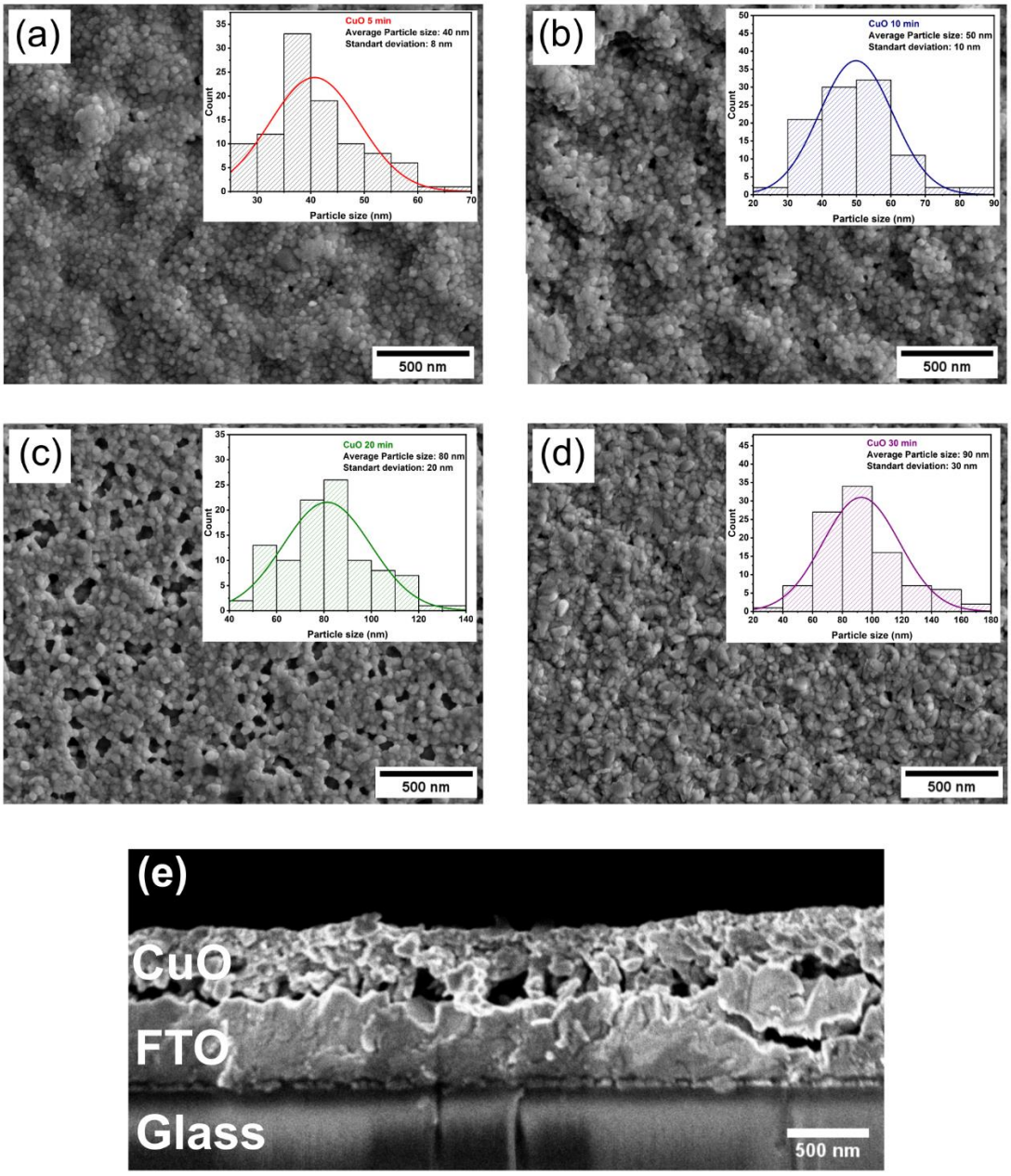

Figure 28 – Top-view SEM images for the CuO films deposited in (a) 5, (b) 10, (c) 20, and (d) 30 minutes and annealed at 550° C for 8 hours. The average particles size and standard deviations for representative samples are shown in the insets. (e) Cross-section SEM for the CuO film deposited in 10 minutes and annealed at 550° C for 8 hours.
Source: By the author.

4.2.2 Optical and electronical properties

In this section, we will only discuss the optoelectronic properties of optimized CuO (in the context of section 4.2.3) because the bandgap, electronic structure, and surface composition of our CuO-based films were not thickness dependent. As shown in Figure 29a, the CuO has a photoactive response across the entire visible spectrum (ideal for PEC applications), exhibiting

an absorption threshold of around 850 nm, characteristic of monoclinic CuO with a bandgap between 1.2 and 1.7 eV.[26-27,80] Tauc analysis (Figure 29b) clearly shows that CuO has a direct bandgap of 1.53 eV, which corresponds to the bandgap of monoclinic CuO.

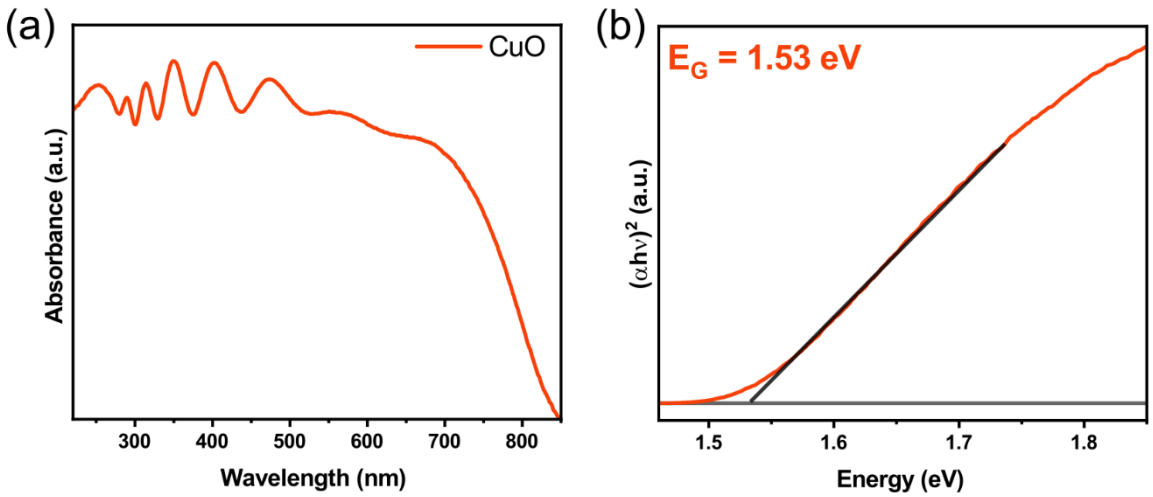

Figure 29 – (a) UV-vis absorption spectrum for the optimized CuO film (deposited in 10 minutes and annealed at 550° C for 8 hours) and (b) Tauc Plot analysis.
Source: By the author.

X-ray photoelectron spectroscopy (XPS) was employed on the CuO film to investigate its electronic structure and surface chemical composition. The high-resolution XPS spectra of Cu 2p (Figure 30a) exhibit two peaks at 953.2 and 933.3 eV, ascribed to the Cu $2p_{1/2}$ and Cu $2p_{3/2}$ of Cu^{2+}, respectively.[126] Furthermore, three satellite peaks were observed at 962.4, 943.9, and 941.3 eV, which are characteristic signatures for the Cu^{2+} state.[127] Figure 30b shows that the XPS spectrum of O 1s can be deconvolved into three characteristic peaks at 529.8, 531.0 and 532.2 eV, which are related to the O^{2-} ions of the crystal structure (Cu-O, O_L peak), oxygen vacancies/defects (O_V peak), and chemisorbed and dissociated oxygen species (O_2^-, O^{2-} or OH^-, O_C peak), respectively.[127] Therefore, the XPS further demonstrates that the as-sputtered Cu film was successfully converted into a high purity CuO film, corroborating with the XPS and Raman results.

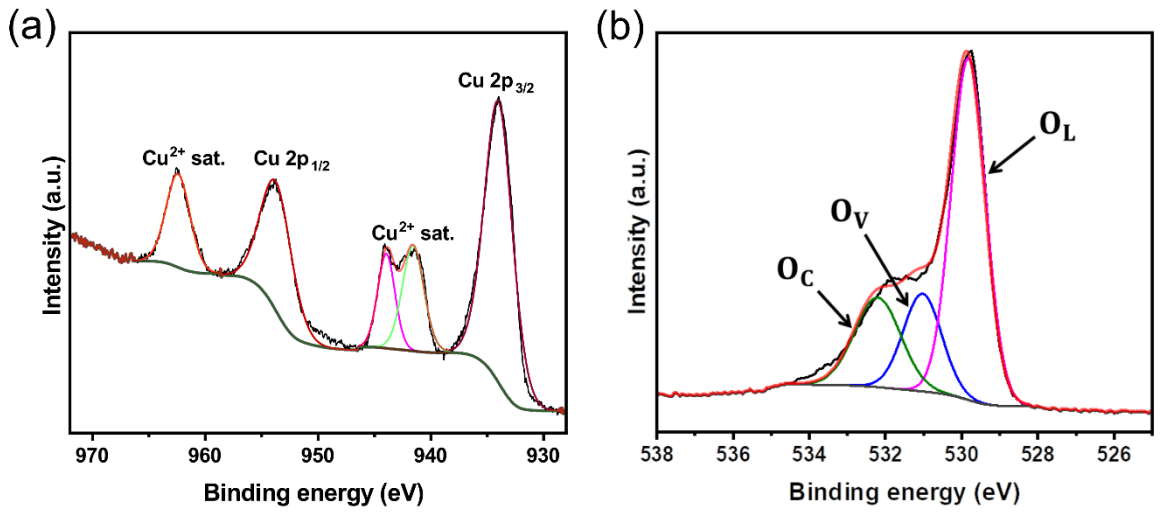

Figure 30 – XPS spectra of CuO film deposited in 10 minutes and annealed at 550° C for 8 hours: (a) Cu 2p and (b) O 1s.
Source: By the author.

4.2.3 Photoelectrochemical properties

The PEC performance of our photocathodes was evaluated in a 1 M KBi buffer (pH 9.5). Figure 31a shows the current density vs. applied potential (j-V) curves – under constant 100 mW cm^{-2} AM 1.5G illumination – for CuO films deposited in 5, 10, 20, and 30 minutes and annealed at 550 °C for 8 hours. All CuO films exhibited cathodic photocurrents when polarized in the reverse direction, evidencing their p-type semiconducting nature. Among these photocathodes, the CuO deposited in 10 minutes showed superior PEC performance, reaching -0.39 mA cm^{-2} at 0.4 V vs. RHE (a relatively high photocurrent density for low applied bias). Nevertheless, photocurrent densities are not significantly decreased for thicker films, suggesting that photogenerated charge carriers have high mobility in the CuO compound. It is essential to note that our photocathodes were not polarized at more negative potentials because (i) only the low-applied bias range matters for Tandem cells, and (ii) CuO has extreme chemical instability under applied reverse potentials. Like the BVO photoanodes (Figure 22a), the compromise between light absorption and charge recombination results in a variation in photocurrent densities as a function of film thickness. The 10-minute condition film produces a CuO layer thick enough to absorb photons and generate charge carriers without compromising charge transfer and separation.

In this context, we employed EIS to further investigate the interfacial charge transfer properties of these all-sputtered CuO films. Interestingly, the Nyquist curves for these photocathodes exhibited two semicircles in the high and low-frequency regions, corresponding to the charge transfer processes inside the semiconductor and in the photocathode/electrolyte

interface, respectively (Figure 31b).[128-129] As a result, all Nyquist curves were simulated with the equivalent circuit shown in the inset of Figure 31b, where (i) C_{SC} and C_H are the constant phase elements associated with the capacitance of the SCR and the Helmholtz layer, respectively, (ii) R_{SC} and R_{CT} represent the charge transfer resistances in the SCR of the photocathode and in the photocathode/electrolyte interface, respectively; and (iii) R_S represents the series resistance (wires and electrolyte). Table 3 shows that R_S and R_{SC} resistances are similar for all CuO photocathodes. In contrast, the thickness significantly influences the charge transfer resistance at the semiconductor/electrolyte interface, with the 5-minute film having a considerably higher value than the others. As a result, EIS suggests that forming more compact and denser CuO layers (see Figure 28) provides a higher contact area between the semiconductor and the electrolyte, which justifies the lower charge transfer resistance and similar current density for the thicker films (10, 20, and 30 minutes). Furthermore, the lower R_{CT} value for the 10-minute film also explains its higher PEC performance seen in Figure 31a.

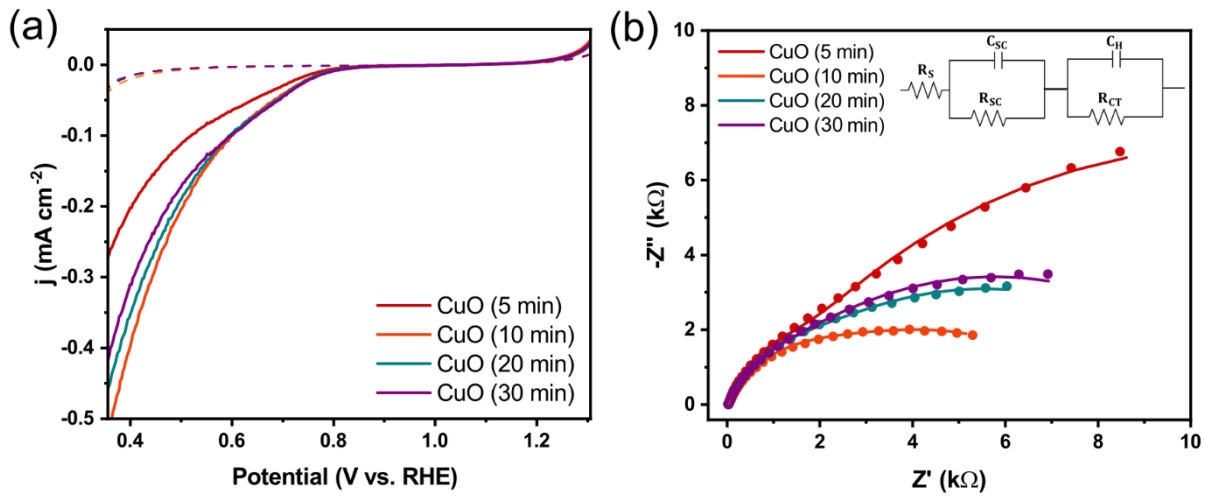

Figure 31 – PEC performance of CuO films. (a) j-V curves under AM 1.5G illumination, (b) EIS response measured under open-circuit potentials and (inset) the equivalent circuit model with components described in the text.

Source: By the author.

Table 3 - Series, space-charge layer, and interfacial charge transfer resistances of CuO photocathodes.

Photocathode	$\mathbf{R_S(\Omega)}$	$\mathbf{R_{SC}(k\Omega)}$	$\mathbf{R_{CT}(k\Omega)}$
CuO (5 min)	28.1± 0.2	0.99 ± 0.02	20.7±0.5
CuO (10 min)	27.3± 0.2	1.12 ± 0.02	6.2±0.3
CuO (20 min)	29.4± 0.2	1.10 ± 0.05	9.2±0.4
CuO (30 min)	28.1± 0.2	0.93 ± 0.03	9.9±0.4

Source: By the author.

Henceforth, all PEC measurements were performed with the optimized CuO film (deposited in 10 minutes and annealed at 550° C for 8 hours). Figure 32a shows the j-V curve for this CuO photocathode under chopped AM 1.5G illumination. Interestingly, the onset for the water reduction (inset of Figure 32a) is approximately 1.03 V, shifted from the flat band potential (section 4.2.4) by ~180 mV. Such onset potential for HER at very positive potentials is ideal for application in Tandem cells since higher photocurrent densities are generated at low applied potentials. Furthermore, an abrupt increase in current density is observed for potentials below ~0.4 V vs. RHE, which is associated with the photodegradation of CuO for large applied reverse bias and illumination.[26,27,83] As a result, the j-V curves for the CuO photocathodes were always measured in the potential range between 1.2 to 0.4 V vs. RHE, where we did not observe variation in the current density after several consecutive PEC measurements.

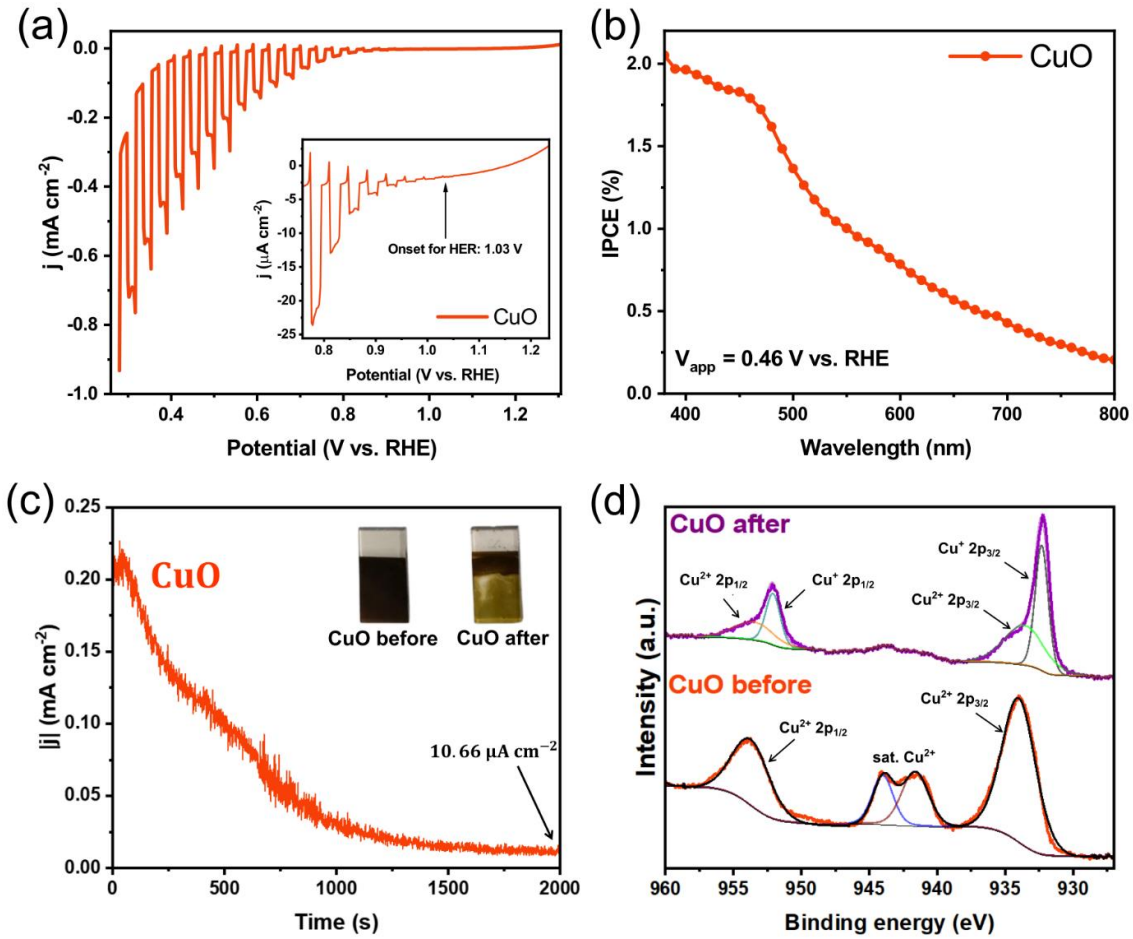

Figure 32 – PEC performance of optimized CuO film (deposited in 10 minutes and annealed at 550° C for 1 hour). (a) Chopped j-V curve under AM 1.5G illumination and (inset) magnification of the low bias region to determine its onset potential. (b) IPCE curves obtained at +0.46 V vs. RHE; (c) temporal stability by chronoamperometry measurements under +0.46 V vs. RHE, and (inset) digital photographs of CuO films before and after stability measurements; (d) Cu 2p XPS spectra for CuO films before and after the temporal stability measurements.

Source: By the author.

To further investigate the influence of light absorption on the PEC performance of the optimized CuO film, we measured its IPCE values under +0.46 V vs. RHE. As shown in Figure 32b, the CuO film has a photoactive range between 380 – 800 nm, corroborating the absorbance spectrum and consistent with the bandgap of 1.53 eV determined by the Tauc Plot (see Figure 29). The extended light absorption of CuO is one of the main advantages of using this compound as a photocathode in a stacked Tandem cell since it can absorb and produce charge carries from a more extensive range of photons transmitted by the photoanode (with a larger bandgap). Furthermore, CuO showed the highest IPCE value of around 2.05 % at 380 nm, indicating that high-energy photons are more efficiently converted into photocurrents.

The key challenge for employing copper oxide-based photocathodes for PEC water splitting is the chemical instability of these compounds in aqueous solutions. To access the PEC stability of our optimized CuO photocathode, we measured its current density against the time (j-t curve) under + 0.46 V vs. RHE for 2500 seconds. As shown in Figure 32c, the CuO film exhibits extreme chemical instability for HER, retaining only ∼18 % of its initial photocurrent density during 1000 seconds. However, a stable current density of $\sim 10\ \mu A\ cm^{-2}$ occurs from 1500 to 2500 seconds. Interestingly, digital photographs of the CuO films before and after the chronoamperometric measurements are also shown in Figure 32c (inset), visually confirming that CuO is strongly photodegraded under working conditions for PEC water splitting.

In this context, XPS was employed to investigate the surface chemical composition of CuO films after chronoamperometric measurements. In particular, it is well known that CuO initially reduces to Cu_2O under reverse bias and illumination and may undergo further reduction to metallic Cu.[82,120,121] Figure 32d shows the high-resolution XPS spectra of Cu 2p for the CuO film before and after the stability test. Notably, in addition to the two characteristic peaks of the Cu^{2+} (at 953.45 and 933.49 eV), two new peaks appear at 952.03 and 932.23 eV, corresponding to Cu $2p_{1/2}$ and Cu $2p_{3/2}$ of the Cu^{+} oxidation state, respectively.[130] The Cu^{+} and Cu^{2+} concentrations in the CuO film after PEC stability (calculated from the Cu 2p spectrum) are 51.2 and 48.8%, respectively. As a result, the XPS unambiguously shows that CuO is partially converted into Cu_2O during PEC measurements. This further indicates that some of the photogenerated electrons are wasted in the photocorrosion of CuO rather than in the hydrogen evolution reaction. In summary, our stability results therefore show that (i) the development of protective layers is of fundamental importance for CuO-based photocathodes, and (ii) Tandem cells based on unmodified CuO films tend to have low durability. Nevertheless, it is essential to point out that the chronoamperometry measurements were

performed with a fixed applied potential, drastically increasing the corrosion of the CuO layer. Indeed, we will show in section 4.3 that our optimized CuO photocathode can be coupled with the BVO/$FeNiO_x$ photoanode in a stacked Tandem cell, producing a bias-free stable current (assisted only by AM 1.5G illumination) for at least 10 minutes.

4.2.4 Interfacial band alignment and charge transport properties

To provide solid insights into the interfacial band alignment and charge transfer properties in our all-sputtered CuO film, we employed UV-vis spectroscopy and Mott-Schottky analysis to construct the isolated energy band diagram of CuO. As shown in Figure 33a, the MS curve for the optimized CuO film exhibits a straight line with a negative slope, characteristic of p-type semiconductors, resulting in flat band potential of $E_{FB} \approx 1.21$ V and acceptor concentration $N_A \approx 2.3 \times 10^{20}$ cm^{-3}, which are values close to those found in the literature.[26,80] Furthermore, from the arguments of section 4.1.4, the CuO band diagram was constructed by assuming that the difference between the flat band energy (approximately giving the semiconductor Fermi energy) and the CB edge is $\sim$0.2 eV. As shown in Figure 33b, the CB edge of CuO lies above 0 eV vs. RHE, indicating that this compound may produce photogenerated electrons with sufficient energy to reduce H^+ to H_2.

To investigate the CuO band diagram under operating conditions for PEC water splitting, we determined the open-circuit potential (OCP) values under dark and AM 1.5G illumination. Importantly, the OCP potential in the dark provides the dark equilibrium energy (E_{dark}) between the Fermi energy of the semiconductor and the electrochemical potential of the electrolyte.[18,42] Note that due to the presence of two redox potentials (water oxidation and reduction) in the electrolyte, the OCP value must be located between 0 and +1.23 V vs. RHE. Figure 33c schematically depicts this situation, showing that the semiconductor Fermi energy aligns with the dark OCP potential (E_{dark}) at $\sim$0.71 V vs. RHE, originating an SCR inside the CuO with potential drop $\Psi_2 = 0.50$ V and depletion length $W_2 = 2.1$ Å. Importantly, these values were calculated by assuming that all potential drop at the CuO/KBi interface occurs over the CuO surface, i.e., $q\Psi_2 = E_{F2} - E_{dark} = q\Psi_{bi}$.

Furthermore, the difference between the OCP value under light and dark provides the photovoltage (V_{ph}) developed in the semiconductor due to the production of photogenerated charges in the SCR.[18,32,42] As shown in Figure 33c, the OCP potential under AM 1.5 illumination is shifted to more positive energies, characteristic of p-type semiconductors,

producing a relatively high photovoltage of ≈ 141 mV. This photovoltage promotes the flattening band phenomenon, reducing the spatial and energetic extension of the SCR and increasing the dark Fermi energy by qV_{ph}. In addition, illumination splits the dark Fermi energy into QFL for electrons and holes, whose separation at the SCLJ interface provides the free energy $\Delta\mu_{ex}$ stored in electron-hole pairs. It is essential to emphasize that the comparison of the j-V curves under dark and AM 1.5G illumination is inappropriate for determining $\Delta\mu_{ex}$ for CuO due to the abrupt increase in dark current density (Figure 32a) caused by the photocorrosion of this compound. Therefore, we assumed that $\Delta\mu_{ex} \approx 0.6E_G$ for our CuO films, a conservative hypothesis compared to Bolton's method[19,43] (where $\Delta\mu_{ex} \approx 0.75E_G$).

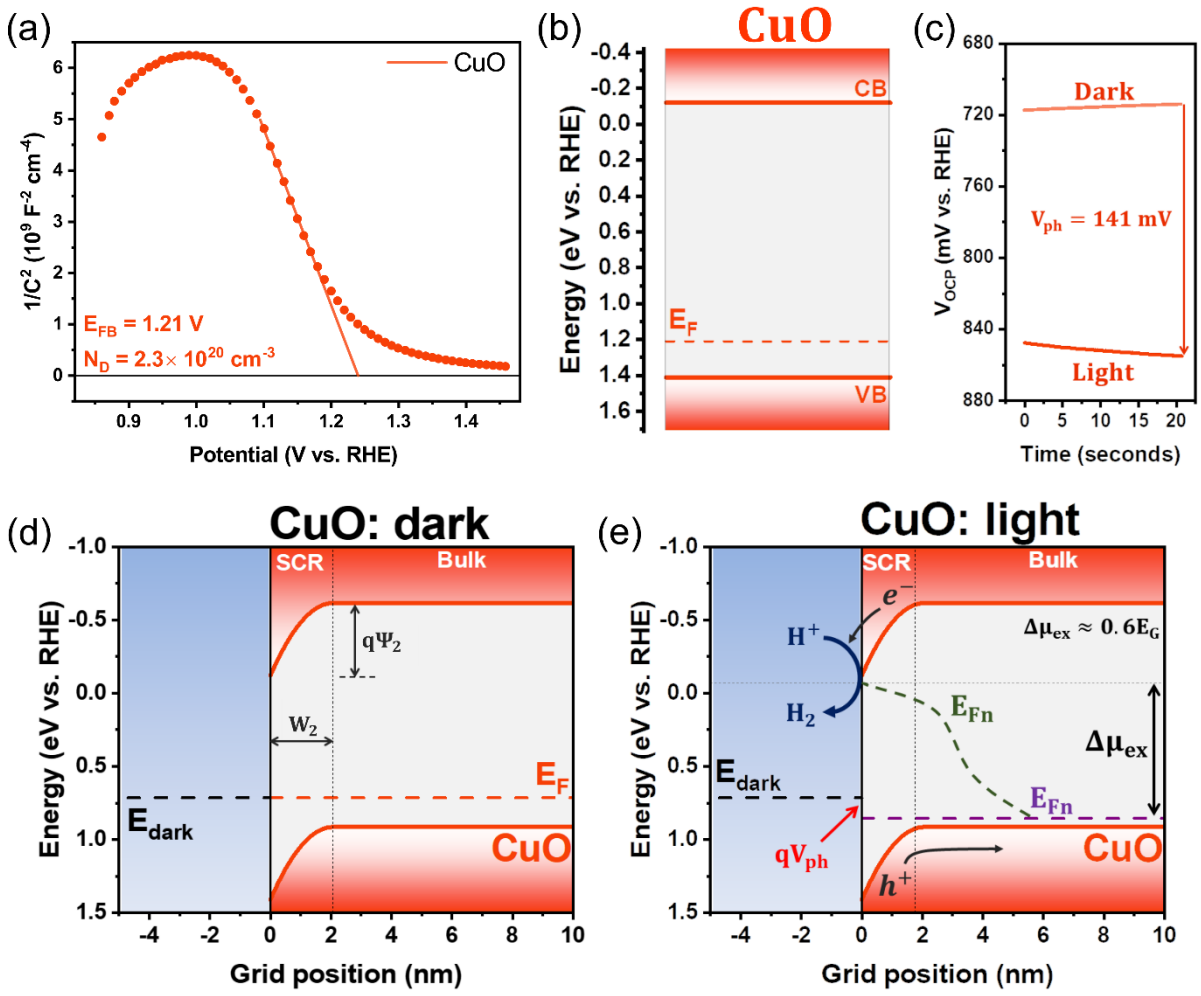

Figure 33 – (a) MS curves under dark conditions and 1 kHz. (b) isolated band diagram, and (c) open-circuit potentials under dark and AM 1.5 illumination for the optimized CuO film. Interfacial band alignment of the SCLJ formed between the optimized CuO and KBi electrolyte (pH 9.5) under (d) dark and (e) AM 1.5 illumination.
Source: By the author.

In this context, Figure 33d shows the band diagram of CuO under 1.5G AM illumination, clearly capturing (i) the band flattening process caused by the photovoltage

(where Ψ_2 and W_2 decays to 0.36 V and 1.76 nm, respectively) and (ii) the qualitative splitting of dark Fermi energy into QFL for electrons and holes. In particular, the dark Fermi energy is increased by $qV_{ph} \approx 141$ mV (Figure 33d), and the QFL separation at the interface is $\Delta\mu_{ex} \approx 0.6E_G = 0.92$ eV. As a result, the QFL for electrons at the SCLJ (≈ -0.1 eV) is more negative than the water reduction potential, showing that photogenerated electrons in CuO have enough energy to reduce H^+ to H_2. Therefore, our band diagrams show that (i) the photogenerated electrons on the CB of CuO are accelerated by the built-in electric field in the SCR (which may be intensified by applying reverse bias) towards the electrolyte for conducting HER, and (ii) the photogenerated holes in the VB of CuO migrate first to the back contact and then are directed to the counter electrode in a three-electrode configuration (or photoanode in a Tandem device). As a result, our optimized CuO film was employed as a photocathode for HER in a Tandem PEC device because it can produce enough photovoltage and free energy to split water molecules into H_2, assisted only by solar energy.

4.3 Tandem PEC cell with $BiVO_4$ and CuO photoelectrodes

Tandem PEC cell construction has been regarded as one of the most promising pathways for producing green H_2 from sunlight. In this context, we employed our optimized BVO/$FeNiO_x$ and CuO semiconducting films as photoelectrodes for OER and HER, respectively, in a simple and low-cost Tandem device. As discussed in section 2.4, photoelectrodes for bias-unassisted overall water splitting in Tandem cells must meet several requirements concerning interfacial band alignment. Remarkably, our semiconducting films satisfy all these requirements (see Figures 26 and 33) since (i) the QFL for holes at the n-BVO/p-$FeNiO_x$ interface ($E_{FP} \approx 1.8$ eV) is more positive than $E^0_{ox} = 1.23$ eV, (ii) the QFL for electrons at the CuO/KBi interface ($E_{Fn} \approx -0.1$ eV) is more negative than $E^0_{red} = 0$ eV, (iii) and the CB edge of the BVO ($E_{C1} = 0.06$ eV) is more negative than the VB edge of CuO ($E_{V2} = 1.41$ eV).

In addition to proper band placement, the total free energy stored in the electron-hole pairs must be higher than $\Delta\mu_{ex}^{min} = 1.23 + \eta_{ox} + \eta_{red}$ for accomplishing bias-free overall water splitting.[16,18] By comparing the onset potentials for water oxidation and reduction (Figures 23a and 31a) with the corresponding flat band potentials (Figures 24a and 33a), we see that $\eta_{ox} \approx 80$ meV for BVO/$FeNiO_x$ and $\eta_{red} \approx 180$ meV for CuO. Remarkably, the predicted $\Delta\mu_{ex}$ for the BVO/$FeNiO_x$-CuO Tandem device is roughly $\Delta\mu_{ex} = \Delta\mu_{ex}^{BVO/FeNiO_x} + \Delta\mu_{ex}^{CuO} \approx 2.3$ eV (see Figure 25a and section 4.2.4). As a result, $\Delta\mu_{ex} \gg \Delta\mu_{ex}^{min} \approx 1.49$ eV, indicating

that our proposed PEC device is capable of producing photogenerated charges with enough energy to satisfy the energetic requirements of overall water splitting and kinetic overpotentials for OER and HER without applying external potentials.

Before developing the Tandem system, the maximum operating current density (j_{OP}) that would flow in the two-electrode arrangement can be estimated by examining the j-V curves for individual photoelectrodes (measured in the three-electrode configuration).[16–18,20] According to section 2.4, the Tandem device only accomplishes bias-unassisted overall water splitting when the photocurrent densities of the photoanode and photocathode intersect at a value $j_{OP} \neq 0$; otherwise, a minimum external potential must be applied to the system. In this context, Figure 34a exhibits the photocurrent densities (j_{ph}) as a function of the applied potential for the BVO/$FeNiO_x$ and CuO photoelectrodes. Note that (i) the dark currents were subtracted from the total current densities (j) for determining j_{ph} produced under 1.5G AM illumination, and (ii) the absolute value of j_{ph} was taken to flip the sign of the cathodic photocurrent in CuO. Encouragingly, the photocurrent densities produced by the two photoelectrodes intersect at $j_{OP} \approx 130\ \mu A\ cm^{-2}$, indicating that the BVO/$FeNiO_x$−CuO Tandem PEC device can produce a bias-unassisted photocurrent density of $j_{OP}^{max} \approx 130\ \mu A\ cm^{-2}$, powered only by AM 1.5G illumination. It is crucial to emphasize that our j-V curves intersect at a value $j_{OP} \neq 0$ mainly because BVO/$FeNiO_x$ exhibits excellent PEC performance for low applied bias, while CuO has an onset for water reduction at a high positive potential.

Motivated by these results, we built a metal oxide-based Tandem device by coupling the BVO/$FeNiO_x$ photoanode with the CuO photocathode in a two-electrode configuration. As shown in the inset of Figure 34b, our novel Tandem cell has a stacked configuration, where the AM 1.5G illumination is first irradiated on the photoanode and subsequently transmitted toward the photocathode. In this ideal arrangement, Bolton's method (section 2.4) indicates a maximum photocurrent density of $\sim 5.3\ mA\ cm^2$ (corresponding to an STH efficiency of ~6.5%), where $E_{G1} = 2.58\ eV$, $E_{G2} = 1.53\ eV$, and $U_{loss} \approx 2\ eV$ for our Tandem cell. It is important to emphasize that this theoretical value is significantly higher than j_{OP}^{max}, demonstrating that there is still much progress to be made in improving the IPCE values, charge transfer separation and efficiencies, and photocurrent densities of our photoelectrodes. As the main result of this dissertation, Figure 34b shows the photocurrent density produced by the BVO/$FeNiO_x$−CuO Tandem device under constant 1.5G AM illumination (without external bias) for 1000 seconds. Interestingly, the j-t curve for our Tandem device exhibits an initial transient behavior, where

the photocurrent density peaks at ~120.2 μA cm^{-2} (close to j_{OP}^{max}) immediately after receiving AM 1.5G illumination and then rapidly declining to ~58.1 μA cm^{-2} in only 50 seconds (a decrease of ~48%). This transient photocurrent spike is attributed to the instantaneous displacement current caused by charging the SCR capacitance with photogenerated charges. However, these charges tend to build-up and recombine in the SCLJ due to the slow kinetics of OER and HER, thereby decreasing j_{ph} until reaching a steady state condition, where the surface charge concentration becomes constant.[18,131] The steady-state condition is clearly seen in Figure 34b, where a slowly decaying photocurrent density takes place after the initial transient peak, retaining ~87% of its value in $t = 50$ seconds ($j_{ph} = 58.1$ μA cm^{-2}) when $t = 1000$ seconds (where $j_{ph} = 50.5$ μA cm^{-2}). Interestingly, this operating photocurrent is very similar to that reported for an analogous Tandem cell composed of BVO-based and Cu_2O photoelectrodes.[45]

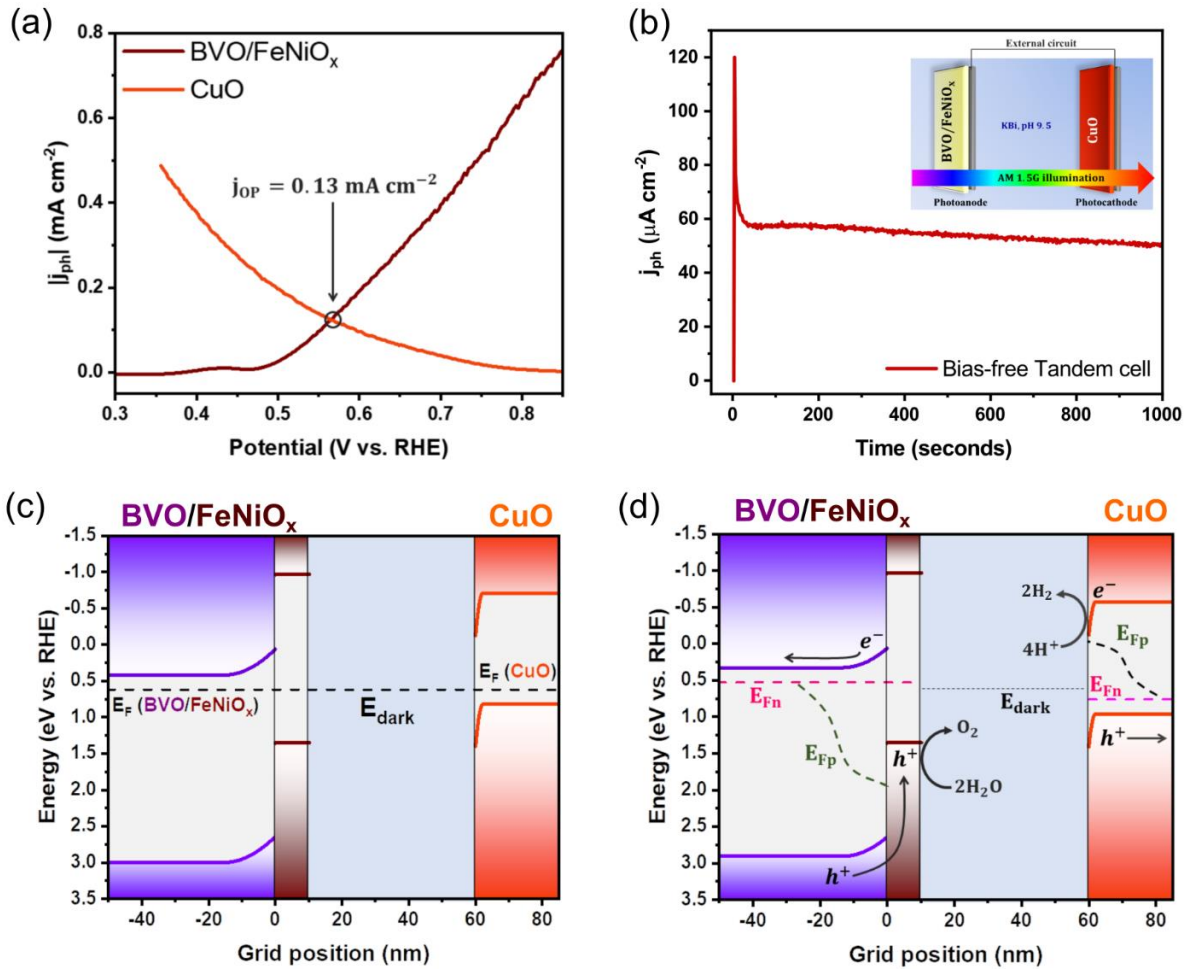

Figure 34 – (a) Absolute value of photocurrent densities in the function of applied potentials for the BVO/FeNiO$_x$ photoanode and CuO photocathode, measured in the three-electrode configuration. (b) Photocurrent density against time curve for the two-electrode BVO/FeNiO$_x$ – CuO Tandem cell, measured under AM 1.5 illumination without applied potential. Interfacial band alignment for the (two-electrode) BVO/FeNiO$_x$ – CuO Tandem cell under (a) dark and (b) AM 1.5G illumination conditions.

Source: By the author.

As a result, our Tandem device can produce an essentially constant operating current density of $j_{OP} \approx 50$ μA cm^{-2} for up to at least 1000 seconds, directly associated with the HER and OER reactions taking place at the surface of photoelectrodes. To further investigate how the BVO/FeNiO$_x$ – CuO Tandem system develops an operating photocurrent $j_{OP} \neq 0$ without external bias, we determined the interfacial band alignment of these semiconductor layers (connected in a two-electrode configuration) under dark conditions and 1.5G AM illumination. Figure 34c shows the alignment of the electrochemical potentials of BVO/FeNiO$_x$, CuO, and KBi phases with the (dark) OCP potential $\left(E_{dark} = qV_{OC}^{dark} \approx 0.62\ eV\right)$, indicating net zero current flow across the Tandem device under dark condition; note that this OCP lies between the E_{dark} for individual BVO/FeNiO$_x$ and CuO films measured in the three-electrode configuration (Figure 25a and 33c). Table 4 displays the values of potential drops and depletion lengths (calculated from the classical band bending model) developed at the BVO/FeNiO$_x$ and CuO/KBi interfaces at (dark) equilibrium.

Under AM 1.5G illumination (Figure 34d), the photovoltages in the BVO/FeNiO$_x$ and CuO photoelectrodes induce the band flattening, lowering the values of dark Ψ_1, Ψ_2, W_1 e W_2 (see Table 3) and increasing (decreasing) the dark Fermi energy of the CuO (BVO/FeNiO$_x$) layer. Figure 35b also depicts the splitting of the dark Fermi level into QFL for electrons and holes, demonstrating that E_{Fp} at the BVO/FeNiO$_x$ interface and E_{Fn} at the CuO/KBi interface are appropriate for producing photogenerated holes and electrons with sufficient energy to perform OER and HER, respectively. Importantly, the values of $\Delta\mu_{ex}$ and V_{ph} for the BVO/FeNiO$_x$ and CuO films were determined in sections 4.1.4 and 4.2.4. Therefore, according to our band diagrams, the photogenerated holes in the VB of BVO are accelerated by the QFL gradient towards FeNiO$_x$, where the OER reaction occurs more efficiently (cocatalyst effect). In contrast, the photogenerated electrons on BVO migrate to the FTO, being conducted through the external circuit towards the VB of CuO. On the other hand, photogenerated electrons on CuO migrate to the electrolyte, reducing H^+ into H_2; the corresponding photogenerated holes are directed towards the FTO, recombining with the electrons from BVO. As a result, our BVO/FeNiO$_x$ – CuO Tandem system can produce enough photovoltage and free energy to conduct OER and HER assisted only by solar energy, justifying the production of an operating current $j_{OP} \neq 0$ without external potentials.

Table 4 - Potential drops (Ψ_1 and Ψ_2) and depletions lengths(W_1 and W_2) as defined in Figure 16 for the BVO/FeNiO$_x$ and CuO/KBi interfaces under dark (superscript: dark) and AM 1.5 illumination (superscript: light). All potential drops are given in volts and depletions lengths in nanometers.

Interface	Ψ_1^{dark}	Ψ_2^{dark}	W_1^{dark}	W_2^{dark}	Ψ_1^{light}	Ψ_2^{light}	W_1^{light}	W_2^{light}
BVO/FeNiO$_x$	0.36	0.01	15.68	0.09	0.27	0.01	13.48	0.08
CuO/KBi		0.59	2.26			0.45	1.97	

Source: By the author.

It is essential to emphasize that the maximum STH efficiency of our PEC device is only 0.06 % (assuming a Faradaic efficiency of 100 %), which is a value significantly lower than that considered as a benchmark for practical applications. However, the faradaic efficiency for the BVO/FeNiO$_x$ – CuO system is certainly less than 100 % due to the photodegradation of CuO into Cu_2O and the production of surface peroxide species on the BVO/FeNiO$_x$ photoanode. That is, a portion of the operating photocurrent density is attributed to surface reactions not involving OER and HER. Indeed, our CuO film was severely photodegraded after chronoamperometric measurement in the Tandem cell (see Figure 35a), evidencing the extreme chemical instability of this compound under AM 1.5G illumination. In contrast, the PEC performance of our BVO/FeNiO$_x$ was unchanged after bias-unassisted water splitting (Figure 35b), as expected due to its excellent chemical stability for OER.

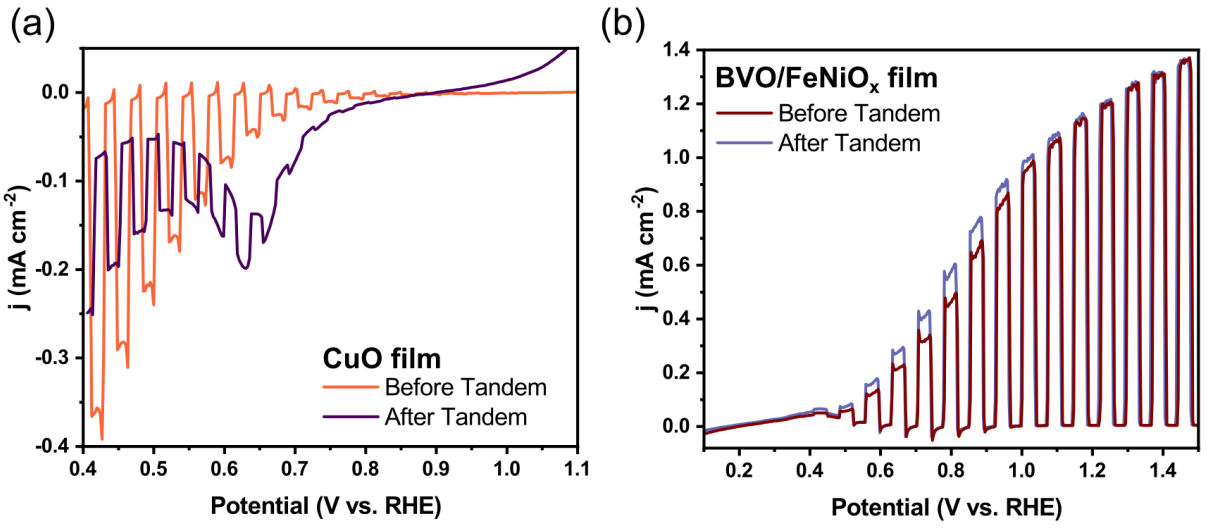

Figure 35 – Chopped j-V curves measured in a three-electrode configuration for (a) CuO and (b) BVO/FeNiO$_x$ photoelectrodes before and after (1000 seconds of) bias-unassisted water splitting in the Tandem cell.
Source: By the author.

As a result, the experimental value of $j_{OP} \approx 50\ \mu A\ cm^{-2}$, much lower than $j_{OP}^{max} = 130\ \mu A\ cm^{-2}$, is directly associated with the substantial photodegradation of the CuO layer

under operating conditions for PEC water splitting. Furthermore, photon loss due to reflection and scattering effects, high interfacial recombination of photogenerated charges, and inefficient injection of photogenerated electrons from CuO to the electrolyte (due to the absence of cocatalysts for HER) may also explain the significant difference in measured j_{OP} against the maximum value for our Tandem cell. These results clearly show that there are still many challenges to be addressed for improving the PEC performance and chemical stability of our photoelectrodes, with the ultimate goal of achieving a more efficient and durable overall water splitting. In particular, developing protective layers for CuO films, ideally inducing p-n heterojunctions or cocatalyst effect, is of fundamental importance to improve the PEC performance and chemical stability of this compound. In addition, new strategies should be employed to improve the PEC performance of the BVO-based photoanode, including (i) doping to decrease its bandgap energy and provide more significant absorption of visible light and (ii) forming more efficient p-n heterojunctions to increase the charge separation efficiency.

5 CONCLUSIONS AND PERSPECTIVES

In summary, we successfully developed a simple and low-cost Tandem cell for bias-unassisted water splitting composed of a BVO/$FeNiO_x$ photoanode and a CuO photocathode, responsible for OER and HER, respectively. In particular, our optimized BVO/$FeNiO_x$ heterojunction showed excellent PEC performance for OER, achieving a photocurrent density of 1.22 mA cm^{-2} at +1.23 V vs. RHE, and a high charge transfer efficiency of 96 % at the same potential. Furthermore, the BVO/$FeNiO_x$ film exhibited excellent chemical stability, retaining ~90 % of its initial photocurrent during 1 hour (under AM 1.5G illumination and +1.23 V vs. RHE). Our band diagrams and MS measurements unambiguously showed the formation of local p-n heterojunctions between the BVO layer and the $FeNiO_x$. As a result, the built-in electric field arising at the p-n interface has several influences on the enhanced PEC performance of the BVO/$FeNiO_x$, including (i) accelerating photogenerated electrons from the BVO to the $FeNiO_x$, (ii) inhibiting electron flow from the BVO to the $FeNiO_x$, (iii) preventing the accumulation of photogenerated charges in the BVO layer (minimizing its photodegradation), and (iv) increasing the charge separation efficiencies of bare BVO. Furthermore, our band diagrams under AM 1.5G illumination showed that the BVO/$FeNiO_x$ heterojunction is a promising photoanode for Tandem cells since it produces holes with enough energy for OER without needing external potentials (as ascertained by the thermodynamically suitable position of E_{Fp} in the p-n interface).

Similarly, the optimized all-sputtered CuO photocathode showed an excellent onset potential for HER (~1.03 V vs. RHE), reaching a modest photocurrent density of −0.39 mA cm^{-2} at +0.4 V. However, our CuO film exhibited severe chemical instability at KBi buffer (pH 9.5), quickly reducing to Cu_2O. Nevertheless, our band diagrams showed that CuO develops enough free energy and photovoltage to produce photogenerated electrons capable of performing HER without applying external potentials. Furthermore, the individual j-V curves of the CuO and BVO/$FeNiO_x$ photoelectrodes intersect at a value $j_{OP}^{max} = 130\ \mu A\ cm^{-2}$, indicating that coupling these photoelectrodes in a Tandem cell can produce a maximum short-circuit current of $j_{OP} = 130\ \mu A\ cm^{-2}$ mainly associated with bias-unassisted water splitting (assuming a faradaic efficiency of 100 %, this j_{OP} corresponds to a STH efficiency of 0.15%).

Conclusively, our Tandem cell constructed by coupling BVO/$FeNiO_x$ with CuO in a two-electrode configuration showed an approximately stable current density of $\sim 50\ \mu A\ cm^{-2}$ under 1.5G AM illumination and zero applied bias, evidencing the occurrence of bias-free solar

water splitting reactions. Unfortunately, even considering a faradaic efficiency of 100%, our Tandem cell produces an STH efficiency of only 0.06 %, much lower than the value of 10 % considered the benchmark for practical applications. Importantly, determining the faradaic efficiencies of our photoelectrodes (for which the necessary infrastructure is being developed in our laboratories) is crucial to evaluate the amount of green H_2 produced by the PEC device. Nevertheless, further studies should be carried out to optimize our proposed Tandem cell, with the primary objective of mitigating the severe photodegradation of CuO during HER and increasing the PEC performance of this compound in the region of low applied bias.

In this context, our research group has achieved relative success in mitigating the chemical instability of CuO through the construction of CuO/BVO (p-n) heterojunctions. In particular, $BiVO_4$ has been chosen because of its (i) CB edge placed around 0 V vs. RHE (suitable for HER); (ii) modest chemical stability in the KBi buffer (pH 9.5), and (iii) n-type nature, which allows the induction of type II p-n heterojunctions with CuO. However, the photocurrent densities obtained for our CuO/BVO heterojunctions are still lower to produce high STH efficiencies. Furthermore, we extensively investigated the $CuBi_2O_4$ photocathode during this research period. Unfortunately, this Cu-based ternary oxide semiconductor showed low photocurrent densities (compared to CuO) and severe chemical instability in the KBi buffer (pH 9.5). As a result, although we obtained an excellent photoanode for the OER, our Tandem cell still needs to be improved by finding a low-cost and stable photocathode for HER.

Therefore, we achieved in this work the aims of (i) developing $BiVO_4/FeNiO_x$ and CuO photoelectrodes via magnetron sputtering deposition (a scalable technique) for application in a simple and low-cost Tandem cell, (ii) proposing a model of interfacial band alignment under working conditions for PEC water splitting (avoiding the traditional analysis of flat band diagrams seen in the literature), (iii) achieving a stable operating photocurrent density of ~ 50 $\mu A\ cm^{-2}$ mainly associated with bias-free water splitting reactions for at least 1000 seconds, and (iv) elucidating the requirements and existing challenges for the construction of an efficient Tandem cell for producing green H_2 via bias-unassisted solar water splitting. In addition to individual optimization of the photoelectrodes, our proposed Tandem cell can also be modified to achieve higher photocurrents and STH efficiencies. In particular, constructing artificial photosynthesis leaves (monolithic system[132]), where the FTO substrate has one side covered with $BVO/FeNiO_x$ and the other with CuO, emerges as a feasible system for carrying out bias-free water splitting reactions in a wireless and more compact configuration.

REFERENCES

1 STATISTICAL review of world energy 2022. London, 2022. Available from: https://www.bp.com/en/global/corporate/energy-economics/statistical-review-of-world-energy.html. Accessible at: 13 Feb. 2023.

2 WORLD energy outlook 2022. Paris, 2022. Available from: https://www.iea.org/reports/world-energy-outlook-2022. Accessible at: 12 Feb. 2023.

3 HALL, C. A. S. Fossil fuels. **Lecture Notes in Energy**, v. 36, p. 95–105, 2017.

4 ABAS, N.; KALAIR, A.; KHAN, N. Review of fossil fuels and future energy technologies. **Futures**, v. 69, p. 31–49, 2015. DOI: 10.1016/j.futures.2015.03.003.

5 SOEST, H. L. VAN; ELZEN, M. G. J. DEN; VUUREN, D. P. VAN. Net-zero emission targets for major emitting countries consistent with the Paris agreement. **Nature Communications**, v. 12, n. 1, p. 1–9, 2021.

6 GLOBAL hydrogen review 2022. Paris, 2022. Available from: https://www.iea.org/reports/global-hydrogen-review-2022. Accessible at: 14 Feb. 2023.

7 KIM, J. H.; HANSORA, D.; SHARMA, P.; JANG, J. W.; LEE, J. S. Toward practical solar hydrogen production – an artificial photosynthetic leaf-to-farm challenge. **Chemical Society Reviews**, v. 48, n. 7, p. 1908–1971, 2019.

8 MAZLOOMI, K.; GOMES, C. Hydrogen as an energy carrier: prospects and challenges. **Renewable and Sustainable Energy Reviews**, v. 16, n. 5, p. 3024–3033, 2012.

9 ABBASI, T.; ABBASI, S. A. Renewable hydrogen: prospects and challenges. **Renewable and Sustainable Energy Reviews**, v. 15, n. 6, p. 3034–3040, 2011.

10 PEREZ, R.; ZWEIBEL, K.; HOFF, T. E. Solar power generation in the US: too expensive, or a bargain? **Energy Policy**, v. 39, n. 11, p. 7290–7297, 2011.

11 LEWIS, N. S.; NOCERA, D. G. Powering the planet: chemical challenges in solar energy utilization. **Proceedings of the National Academy of Sciences**, v. 103, n. 43, p. 15729–15735, 2006.

12 VAN DE KROL, R. *et al*. **Photoelectrochemical hydrogen production.** New York: Springer, 2012.

13 BALZANI, V.; CREDI, A.; VENTURI, M. Photochemical conversion of solar energy. **ChemSusChem**, v. 1, n. 1–2, p. 26–58, 2008.

14 CRABTREE, G. W.; LEWIS, N. S. Solar energy conversion. **AIP Conference Proceedings**, v. 1044, n. 1, p. 309, 2008.

15 FUJISHIMA, A.; HONDA, K. Electrochemical photolysis of water at a semiconductor electrode. **Nature**, v. 238, n. 5358, p. 37–38, 1972.

16 PRÉVOT, M. S.; SIVULA, K. Photoelectrochemical tandem cells for solar water splitting. **Journal of Physical Chemistry C**, v. 117, n. 35, p. 17879–17893, 2013.

17 CHEN, Y.; FENG, X.; LIU, Y.; GUAN, X.; BURDA, C.; GUO, L. Metal oxide-based tandem cells for self-biased photoelectrochemical water splitting. **ACS Energy Letters**, v. 5, n. 3, p. 844–866, 2020.

18 GIMÉNEZ, S.; BISQUERT, J. **Photoelectrochemical solar fuel production**: from basic principles to advanced devices. Switzerland: Springer, 2016. 559 p.

19 BOLTON, J. R.; STRICKLER, S. J.; CONNOLLY, J. S. Limiting and realizable efficiencies of solar photolysis of water. **Nature,** v. 316, n. 6028, p. 495–500,1985.

20 WEBER, M. F.; DIGNAM, M. J. Efficiency of splitting water with semiconducting photoelectrodes. **Journal of the Electrochemical Society**, v. 131, n. 6, p. 1258–1265, 1984.

21 HANNAPPEL, T.; SCHWARZBURG, K. On the benchmarking of multi-junction photoelectrochemical fuel generating devices. **Sustainable Energy & Fuels**, v. 1, n. 3, p. 492–503, 2017.

22 PARK, Y.; MC DONALD, K. J.; CHOI, K. S. Progress in bismuth vanadate photoanodes for use in solar water oxidation. **Chemical Society Reviews**, v. 42, n. 6, p. 2321–2337, 2013.

23 KIM, J. H.; LEE, J. S. Elaborately modified BiVO4 photoanodes for solar water splitting. **Advanced Materials**, v. 31, n. 20, p. 1806938, 2019.

24 KIM, T. W.; CHOI, K. S. Nanoporous BiVO4 photoanodes with dual-layer oxygen evolution catalysts for solar water splitting. **Science**, v. 343, n. 6174, p. 990–994, 2014.

25 SUN, J.; ZHONG, D. K.; GAMELIN, D. R. Composite photoanodes for photoelectrochemical solar water splitting. **Energy & Environmental Science**, v. 3, n. 9, p. 1252–1261, 2010.

26 SIAVASH MOAKHAR, R. *et al.* Photoelectrochemical water-splitting using CuO-based electrodes for hydrogen production: a review. **Advanced Materials**, v. 33, n. 33, p. 2007285, 2021.

27 LI, C.; HE, J.; XIAO, Y.; LI, Y.; DELAUNAY, J. J. Earth-abundant Cu-based metal oxide photocathodes for photoelectrochemical water splitting. **Energy & Environmental Science**, v. 13, n. 10, p. 3269–3306, 2020.

28 ZHANG, B.; SUN, L. Artificial photosynthesis: opportunities and challenges of molecular catalysts. **Chemical Society Reviews**, v. 48, n. 7, p. 2216, 2019.

29 COX, N.; PANTAZIS, D. A.; NEESE, F.; LUBITZ, W. Artificial photosynthesis: understanding water splitting in nature. **Interface Focus**, v. 5, n. 3, p. 20150009, 2015.

30 ROS, C.; ANDREU, T.; MORANTE, J. R. Photoelectrochemical water splitting: a road from stable metal oxides to protected thin film solar cells. **Journal of Materials Chemistry A**, v. 8, n. 21, p. 10625–10669, 2020.

31 JIANG, C.; MONIZ, S. J. A.; WANG, A.; ZHANG, T.; TANG, J. Photoelectrochemical devices for solar water splitting – materials and challenges. **Chemical Society Reviews**, v. 46, n. 15, p. 4645–4660, 2017.

32 CHEN, Z.; DINH, H. N.; MILLER, E. **Photoelectrochemical water splitting**: standards, experimental methods, and protocols. New York: Springer, 2013. 126 p.

33 MAEDA, K.; DOMEN, K. Photocatalytic water splitting: recent progress and future challenges. **Journal of Physical Chemistry Letters**, v. 1, n. 18, p. 2655–2661, 2010.

34 ASHCROFT, N. W.; MERMIM N. D. **Solid state physics.** Boston: Cengage Learning, 1976.

35 SIMON, S. H. **The Oxford solid state basics.** Oxford**:** Oxford University Press, 2013.

36 SZE, S. M.; NG, K. K. **Physics of semiconductor devices**. New York: John Wiley & Sons, 2006.

37 GERISCHER, H. Charge transfer processes at semiconductor-electrolyte interfaces in connection with problems of catalysis. **Surface Science**, v. 18, n. 1, p. 97–122, 1969.

38 MARCUS, R. A. On the theory of oxidation-reduction reactions involving electron transfer. I. **Journal of Chemical Physics**, v. 24, n. 5, p. 966, 2004.

39 BOTT, A. W. Electrochemistry of semiconductors. **Current Separations**, v. 17, n. 3, p. 87-92, 1998.

40 WÜRFEL, P.; WÜRFEL, U. **Physics of solar cells:** from basic principles to advanced concepts. New York: John Wiley & Sons, 2016.

41 SALVADOR, P. Semiconductors photoelectrochemistry: a kinetic and thermodynamic analysis in the light of equilibrium and nonequilibrium models. **Journal of Physical Chemistry B**, v. 105, n. 26, p. 6128–6141, 2001.

42 MIAO, B.; IQBAL, A.; BEVAN, K. H. Utilizing band diagrams to interpret the photovoltage and photocurrent in photoanodes: a semiclassical device modeling study. **Journal of Physical Chemistry C**, v. 123, n. 47, p. 28593–28603, 2019.

43 BOLTON, J. R. Solar photoproduction of hydrogen: a review. **Solar Energy**, v. 57, n. 1, p. 37–50, 1996.

44 LATEMPA, T. J.; CHOI, K. S.; GRIMES, C. A. p-type Cu-Ti-O nanotube arrays and their use in self-biased heterojunction photoelectrochemical diodes for hydrogen generation. **Nano Letters**, v. 8, n. 7, p. 1906–1911, 2008.

45 BORNOZ, P *et al*. bismuth vanadate-cuprous oxide tandem cell for overall solar water splitting. **Journal of Physical Chemistry C**, v. 118, n. 30, p. 16959–16966, 2014.

46 LIANG, X. *et al.* Bias-free solar water splitting by tetragonal zircon BiVO4 nanocrystal photocathode and monoclinic scheelite BiVO4 nanoporous photoanode. **Advanced Functional**

Materials, v. 31, n. 8, p. 2008656, 2021.

47 SITAARAMAN, S. R.; NIRMALA GRACE, A.; SELLAPPAN, R. Photoelectrochemical performance of a spin coated TiO2 protected BiVO4-Cu2O thin film tandem cell for unassisted solar water splitting. **RSC Advances**, v. 12, n. 48, p. 31380–31391, 2022.

48 JIANG, F. 3.17% efficient Cu2ZnSnS4–BiVO4 integrated tandem cell for standalone overall solar water splitting. **Energy & Environmental Science**, v. 14, n. 3, p. 1480–1489, 2021.

49 ZHANG, Y.; WANG, L.; XU, X. A bias-free CuBi2O4–CuWO4 tandem cell for solar-driven water splitting. **Inorganic Chemistry Frontiers**, v. 8, n. 16, p. 3863–3870, 2021.

50 JANG, J. W. *et al.* Enabling unassisted solar water splitting by iron oxide and silicon. **Nature Communications**, v. 6, n. 1, p. 1–5, 2015.

51 YAMADA, T.; DOMEN, K. A novel photocathode material for sunlight-driven overall water splitting: solid solution of ZnSe and Cu(In,Ga)Se2. **Advanced Functional Materials**, v. 26, n. 25, p. 4570–4577, 2016.

52 XU, P.; FENG, J.; FANG, T.; ZHAO, X.; LI, Z.; ZOU, Z. Photoelectrochemical cell for unassisted overall solar water splitting using a BiVO4 photoanode and Si nanoarray photocathode. **RSC Advances**, v. 6, n. 12, p. 9905–9910, 2016.

53 BAI, Z.; ZHANG, Y. A Cu2O/Cu2S-ZnO/CdS tandem photoelectrochemical cell for self-driven solar water splitting. **Journal of Alloys and Compounds**, v. 698, p. 133–140, 2017.DOI: 10.1016/j.jallcom.2016.12.261.

54 HIGASHI, T. *et al.* Overall water splitting by photoelectrochemical cells consisting of (ZnSe)0.85(CuIn0.7Ga0.3Se2)0.15 photocathodes and BiVO4 photoanodes. **Chemical Communications**, v. 53, n. 85, p. 11674–11677, 2017.

55 YAMADA, T.; DOMEN, K. Development of highly efficient CuIn0.5Ga0.5Se2-based photocathode and application to overall solar driven water splitting. **Energy & Environmental Science**, v. 11, n. 10, p. 3003–3009, 2018.

56 CHEN, M.; LIU, Y.; LI, C.; LI, A.; CHANG, X.; LIU, W.; SUN, Y.; WANG, T.; GONG, J. Spatial control of cocatalysts and elimination of interfacial defects towards efficient and robust CIGS photocathodes for solar water splitting. **Energy & Environmental Science**, v. 11, n. 8, p. 2025–2034, 8 ago. 2018.

57 HAGFELDT, A.; LUO, J.; GRÄTZEL, M. Boosting the performance of Cu2O photocathodes for unassisted solar water splitting devices. **Nature Catalysis**, v. 1, n. 6, p. 412–420, 2018.

58 ROSA, W. S.; RABELO, L. G.; TIVERON ZAMPAULO, L. G.; GONÇALVES, R. V. Ternary oxide CuWO4/BiVO4/FeCoOxFilms for photoelectrochemical water oxidation: insights into the electronic structure and interfacial band alignment. **ACS Applied Materials and Interfaces**, , v. 14, n. 20, p. 22858–22869, 2022.

59 LUCAS, T. T. A.; MELO, M. A.; FREITAS, A. L. M.; SOUZA, F. L.; GONÇALVES, R. V. Enhancing the solar water splitting activity of TiO2 nanotube-array photoanode by surface coating with La-doped SrTiO3. **Solar Energy Materials and Solar Cells**, v. 208, p. 110428, 2020. DOI: 10.1016/j.solmat.2020.110428

60 HILL, J. C.; CHOI, K.-S. Effect of electrolytes on the selectivity and stability of n-type WO3 photoelectrodes for use in solar water oxidation. **Journal of Physical Chemistry C**, v. 116, n. 14, p. 7612–7620, 2012.

61 DOTAN, H.; SIVULA, K.; GRÄTZEL, M.; ROTHSCHILD, A.; WARREN, S. C. Probing the photoelectrochemical properties of hematite (α-Fe2O3) electrodes using hydrogen peroxide as a hole scavenger. **Energy & Environmental Science**, v. 4, n. 3, p. 958–964, 2011.

62 CHEREPY, N. J.; LISTON, D. B.; LOVEJOY, J. A.; DENG, H.; ZHANG, J. Z. Ultrafast studies of photoexcited electron dynamics in γ- and α-Fe2O3 semiconductor nanoparticles. **Journal of Physical Chemistry B**, v. 102, n. 5, p. 770–776, 1998.

63 HAUTIER, G.; MIGLIO, A.; CEDER, G.; RIGNANESE, G.-M.; GONZE, X. Identification and design principles of low hole effective mass p-type transparent conducting oxides. **Nature Communications**, v. 4, 2013. DOI: 10.1038/ncomms3292.

64 ABDI, F. F.; BERGLUND, S. P. Recent developments in complex metal oxide photoelectrodes. **Journal of Physics D:** applied physics, v. 50, n. 19, p. 193002, 2017.

65 FAN, R.; DONG, W.; FANG, L.; ZHENG, F.; SHEN, M. More than 10% efficiency and one-week stability of Si photocathodes for water splitting by manipulating the loading of the Pt catalyst and TiO2 protective layer. **Journal of Materials Chemistry A**, v. 5, n. 35, p. 18744–18751, 2017.

66 ALQAHTANI, M. *et al.* Heteroepitaxy of GaP on silicon for efficient and cost-effective photoelectrochemical water splitting. **Journal of Materials Chemistry A**, v. 7, n. 14, p. 8550–8558, 2019.

67 HE, H.; LIAO, A.; GUO, W.; LUO, W.; ZHOU, Y.; ZOU, Z. State-of-the-art progress in the use of ternary metal oxides as photoelectrode materials for water splitting and organic synthesis. **Nano Today**, v. 28, p. 100763, 2019. DOI: 10.1016/j.nantod.2019.100763.

68 JANG, Y. J.; LEE, J. S. Photoelectrochemical water splitting with p-Type metal oxide semiconductor photocathodes. **ChemSusChem**, v. 12, n. 9, p. 1835–1845, 2019.

69 TOKUNAGA, S.; KATO, H.; KUDO, A. Selective preparation of monoclinic and tetragonal BiVO4 with scheelite structure and their photocatalytic properties. **Chemistry of Materials**, v. 13, n. 12, p. 4624–4628, 2001.

70 COOPER, J. K.; GUL, S.; TOMA, F. M.; CHEN, L.; LIU, Y. S.; GUO, J.; AGER, J. W.; YANO, J.; SHARP, I. D. Indirect bandgap and optical properties of monoclinic bismuth vanadate. **Journal of Physical Chemistry C**, v. 119, n. 6, p. 2969–2974, 2015.

71 ZHAO, Z.; LI, Z.; ZOU, Z. Electronic structure and optical properties of monoclinic clinobisvanite BiVO4. **Physical Chemistry Chemical Physics**, v. 13, n. 10, p. 4746–4753,

2011.

72 PAYNE, D. J.; ROBINSON, M. D. M.; EGDELL, R. G.; WALSH, A.; MCNULTY, J.; SMITH, K. E.; PIPER, L. F. J. The nature of electron lone pairs in BiVO4. **Applied Physics Letters**, v. 98, n. 21, p. 212110, 2011.

73 COOPER, J. K.; GUL, S.; TOMA, F. M.; CHEN, L.; GLANS, P.-A.; GUO, J.; AGER, J. W.; YANO, J.; SHARP, I. D. Electronic structure of monoclinic BiVO4. **Chemistry of Materials**, v. 26, n. 18, p. 5365–5373, 2014.

74 DING, K.; CHEN, B.; FANG, Z.; ZHANG, Y. Density functional theory study on the electronic and optical properties of three crystalline phases of BiVO4. **Theoretical Chemistry Accounts**, v. 132, n. 5, p. 1–7, 2013.

75 CORREA, A. S.; RABELO, L. G.; ROSA, W. S.; NIQAB, K.; SATHEESH, K.; KHAN, S.; GONÇALVES, R. V. Interfacial band alignment and photoelectrochemical properties of all-sputtered BiVO 4 /FeNiO x and BiVO 4 /FeMnO x p–n heterojunctions. **Energy Advances**, v. 2, n. 1, p. 123–136, 2023.

76 LUO, W.; LI, Z.; YU, T.; ZOU, Z. Effects of surface electrochemical pretreatment on the photoelectrochemical performance of Mo-doped BiVO 4. **Journal of Physical Chemistry C**, v. 116, n. 8, p. 5076–5081, 2012.

77 WOO KIM, C.; SEOK SON, Y.; JONG KANG, M.; YOON KIM, D.; SOO KANG, Y.; KIM, C. W.; SON, Y. S.; KANG, M. J.; KIM, D. Y.; KANG, Y. S. (040)-Crystal facet engineering of BiVO4 plate photoanodes for solar fuel production. **Advanced Energy Materials**, v. 6, n. 4, p. 1501754, 2016.

78 PIHOSH, Y. *et al*. Photocatalytic generation of hydrogen by core-shell WO3/BiVO4 nanorods with ultimate water splitting efficiency. **Scientific Reports**, v. 5, n. 1, p. 1–10, 2015.

79 ZHANG, Q.; ZHANG, K.; XU, D.; YANG, G.; HUANG, H.; NIE, F.; LIU, C.; YANG, S. CuO nanostructures: synthesis, characterization, growth mechanisms, fundamental properties, and applications. **Progress in Materials Science**, v. 60, n. 1, p. 208–337, 2014.

80 MASUDY-PANAH, S. *et al*. Nanocrystal engineering of sputter-grown CuO photocathode for visible-light-driven electrochemical water splitting. **ACS Applied Materials and Interfaces**, v. 8, n. 2, p. 1206–1213, 2016.

81 PARACCHINO, A.; LAPORTE, V.; SIVULA, K.; GRÄTZEL, M.; THIMSEN, E. Highly active oxide photocathode for photoelectrochemical water reduction. **Nature Materials**, v. 10, n. 6, p. 456–461, 2011.

82 LIU, Y.; ZHANG, J.; ZHANG, W.; LIANG, W.; YU, B.; XUE, J. Effects of annealing temperature on the properties of copper films prepared by magnetron sputtering. **Journal Wuhan University of Technology:** materials science edition, v. 30, n. 1, p. 92–96, 2015.

83 XING, H.; LEI, E.; GUO, Z.; ZHAO, D.; LI, X.; LIU, Z. Exposing the photocorrosion mechanism and control strategies of a CuO photocathode. **Inorganic Chemistry Frontiers**, v. 6, n. 9, p. 2488–2499, 2019.

84 KUSHWAHA, A.; MOAKHAR, R. S.; GOH, G. K. L.; DALAPATI, G. K. Morphologically tailored CuO photocathode using aqueous solution technique for enhanced visible light driven water splitting. **Journal of Photochemistry and Photobiology A:** chemistry, v. 337, p. 54–61, 2017.

85 LIU, C.; MENG, F.; ZHANG, L.; ZHANG, D.; WEI, S.; QI, K.; FAN, J.; ZHANG, H.; CUI, X. CuO/ZnO heterojunction nanoarrays for enhanced photoelectrochemical water oxidation. **Applied Surface Science**, v. 469, p. 276–282, 2019.

86 KARTTUNEN, A. **CuO** - solid state chemistry. Available from: https://wiki.aalto.fi/display/SSC/CuO. Accessible at: 14 Feb. 2023.

87 CHEN, L.; TOMA, F. M.; COOPER, J. K.; LYON, A.; LIN, Y.; SHARP, I. D.; AGER, J. W. Mo-Doped BiVO4 photoanodes synthesized by reactive sputtering. **ChemSusChem**, v. 8, n. 6, p. 1066–1071, 2015.

88 GELDERMAN, K.; LEE, L.; DONNE, S. W. Flat-Band Potential of a Semiconductor: using the Mott-Schottky equation. **Journal of Chemical Education**, v. 84, n. 4, p. 13, 2007.

89 VALANT, M.; SUVOROV, D. Chemical compatibility between silver electrodes and low-firing binary-oxide compounds: conceptual study. **Journal of the American Ceramic Society**, v. 83, n. 11, p. 2721–2729, 2000.

90 MANOHAR, A.; VIJAYAKANTH, V.; HONG, R. Solvothermal reflux synthesis of NiFe2O4 nanocrystals dielectric and magnetic hyperthermia properties. **Journal of Materials Science:** materials in electronics, v. 31, n. 1, p. 799–806, 2020.

91 RÀFOLS I BELLÉS, C.; SELIM, S.; HARRISON, N. M.; AHMAD, E. A.; KAFIZAS, A. Beyond band bending in the WO3/BiVO4 heterojunction: insight from DFT and experiment. **Sustainable Energy & Fuels**, v. 3, n. 1, p. 264–271, 2018.

92 CHEN, L.; ALARCÓN-LLADÓ, E.; HETTICK, M.; SHARP, I. D.; LIN, Y.; JAVEY, A.; AGER, J. W. Reactive Sputtering of Bismuth Vanadate Photoanodes for Solar Water Splitting. **Journal of Physical Chemistry C**, v. 117, n. 42, p. 21635–21642, 2013.

93 HARDCASTLE, F. D.; WACHS, I. E. Determination of vanadium-oxygen bond distances and bond orders by Raman spectroscopy. **Journal of Physical Chemistry**, v. 95, n. 13, p. 5031–5041, 2002.

94 SARAKINOS, K.; MARTINU, L. Synthesis of thin films and coatings by high power impulse magnetron sputtering. *In*: LUNDIN, D.; MINEA, T.; GUDMUNDSSON, J. T. (ed.). **High power impulse magnetron sputtering:** fundamentals, technologies, challenges and applications. Berlin: Springer, 2020. p. 333–374.

95 BISHOP, C. A. Nucleation, coalescence, and film growth. *In*: BISHOP, C. A. **Vacuum deposition onto webs, films, and foils**. New YorK: William Andrew, 2007. p. 205–224.

96 GONG, H.; FREUDENBERG, N.; NIE, M.; KROL, R. VAN DE; ELLMER, K. BiVO4 photoanodes for water splitting with high injection efficiency, deposited by reactive magnetron

co-sputtering. **AIP Advances**, v. 6, n. 4, p. 045108, 2016.

97 JU, S.; JUN, J.; SON, S.; PARK, J.; LIM, H.; KIM, W.; CHAE, D.; LEE, H. Structured BiVO4 photoanode fabricated via sputtering for large areas and enhanced photoelectrochemical performance. **ACS Sustainable Chemistry & Engineering**, v. 8, n. 49, p. 17923–17932, 2020.

98 WANG, S.; HE, T.; YUN, J.-H.; HU, Y.; XIAO, M.; DU, A.; WANG, L. New iron-cobalt oxide catalysts promoting BiVO4 films for photoelectrochemical water splitting. **Advanced Functional Materials**, v. 28, n. 34, p. 1802685, 2018.

99 JIANG, Z.; LIU, Y.; JING, T.; HUANG, B.; ZHANG, X.; QIN, X.; DAI, Y.; WHANGBO, M. H. Enhancing the photocatalytic activity of BiVO4 for oxygen evolution by Ce doping: Ce3+ ions as hole traps. **Journal of Physical Chemistry C**, v. 120, n. 4, p. 2058–2063, 2016.

100 COSTER, D.; KRONIG, R. New type of auger effect and its influence on the x-ray spectrum. **Physica**, v. 2, n. 1–12, p. 13–24, 1935.

101 NYHOLM, R.; MARTENSSON, N.; LEBUGLET, A.; AXELSSON, U. Auger and coster-kronig broadening effects in the 2p and 3p photoelectron spectra from the metals 22Ti-30Zn. **Journal of Physics F:** metal physics, v. 11, n. 8, p. 1727,1981.

102 JAIN, S.; SHAH, J.; NEGI, N. S.; SHARMA, C.; KOTNALA, R. K. Significance of interface barrier at electrode of hematite hydroelectric cell for generating ecopower by water splitting. **International Journal of Energy Research**, v. 43, n. 9, p. 4743–4755, 2019.

103 WANG, Q.; WU, L.; ZHANG, Z.; CHENG, J.; CHEN, R.; LIU, Y.; LUO, J. Elucidating the role of hypophosphite treatment in enhancing the performance of BiVO4photoanode for photoelectrochemical water oxidation. **ACS Applied Materials and Interfaces**, v. 14, n. 23, p. 26642–26652, 2022.

104 ZHANG, B.; WANG, L.; ZHANG, Y.; DING, Y.; BI, Y. Ultrathin FeOOH Nanolayers with Abundant Oxygen Vacancies on BiVO4 Photoanodes for Efficient Water Oxidation. **Angewandte Chemie International Edition**, v. 57, n. 8, p. 2248–2252, 2018.

105 ZHANG, K. H. L.; WU, R.; TANG, F.; LI, W.; OROPEZA, F. E.; QIAO, L.; LAZAROV, V. K.; DU, Y.; PAYNE, D. J.; MACMANUS-DRISCOLL, J. L.; BLAMIRE, M. G. Electronic structure and band alignment at the NiO and SrTiO3 p–n heterojunctions. **ACS Applied Materials and Interfaces**, v. 9, n. 31, p. 26549–26555, 2017.

106 WANG, H.; YAO, Q.; WANG, C.; MA, Z.; SUN, Q.; FAN, B.; JIN, C.; CHEN, Y. Hydrothermal synthesis of nanooctahedra MnFe2O4 onto the wood surface with soft magnetism, fire resistance and electromagnetic wave absorption. **Nanomaterials**, v. 7, n. 6, p. 118, 2017.

107 ALI-LÖYTTY, H.; LOUIE, M. W.; SINGH, M. R.; LI, L.; SANCHEZ CASALONGUE, H. G.; OGASAWARA, H.; CRUMLIN, E. J.; LIU, Z.; BELL, A. T.; NILSSON, A.; FRIEBEL, D. Ambient-pressure XPS study of a Ni-Fe electrocatalyst for the oxygen evolution reaction. **Journal of Physical Chemistry C**, v. 120, n. 4, p. 2247–2253, 2016.

108 RUI, K. *et al.* Hybrid 2D dual-metal–organic frameworks for enhanced water oxidation

catalysis. **Advanced Functional Materials**, v. 28, n. 26, p. 1801554, 2018.

109 YANG, J. W.; PARK, I. J.; LEE, S. A.; LEE, M. G.; LEE, T. H.; PARK, H.; KIM, C.; PARK, J.; MOON, J.; KIM, J. Y.; JANG, H. W. Near-complete charge separation in tailored BiVO4-based heterostructure photoanodes toward artificial leaf. **Applied Catalysis B:** environmental, v. 293, p. 120217, 2021.DOI: 10.1016/j.apcatb.2021.120217.

110 SEABOLD, J. A.; CHOI, K. S. Effect of a cobalt-based oxygen evolution catalyst on the stability and the selectivity of photo-oxidation reactions of a WO3 photoanode. **Chemistry of Materials**, v. 23, n. 5, p. 1105–1112, 2011.

111 BEDIN, K. C.; MUCHE, D. N. F.; MELO, M. A.; FREITAS, A. L. M.; GONÇALVES, R. V.; SOUZA, F. L. Role of cocatalysts on hematite photoanodes in photoelectrocatalytic water splitting: challenges and future perspectives. **ChemCatChem**, v. 12, n. 12, p. 3156–3169, 2020.

112 PALANISELVAM, T.; SHI, L.; METTELA, G.; ANJUM, D. H.; LI, R.; KATURI, K. P.; SAIKALY, P. E.; WANG, P. Vastly enhanced BiVO4 photocatalytic OER performance by NiCoO2 as cocatalyst. **Advanced Materials Interfaces**, v. 4, n. 19, p. 1700540, 2017.

113 YANG, J.; WANG, D.; HAN, H.; LI, C. Roles of Cocatalysts in Photocatalysis and Photoelectrocatalysis. **Accounts of Chemical Research**, v. 46, n. 8, p. 1900-1909, 2013.

114 ORAZEM, M. E.; TRIBOLLET, B. **Electrochemical impedance spectroscopy**. Hoboken: John Wiley & Sons, 2008. 523 p.

115 MATSUMOTO, Y. Energy positions of oxide semiconductors and photocatalysis with iron complex oxides. **Journal of Solid State Chemistry**, v. 126, n. 2, p. 227–234, 1996.

116 CHUN, W.-J.; ISHIKAWA, A.; FUJISAWA, H.; TAKATA, T.; KONDO, J. N.; HARA, M.; KAWAI, M.; MATSUMOTO, Y.; DOMEN, K. Conduction and valence band positions of Ta 2 O 5 , TaON, and Ta 3 N 5 by UPS and electrochemical methods. **Journal of Physical Chemistry B**, v. 107, n. 8, p. 1798–1803, 2003.

117 LI, H.; YU, H.; QUAN, X.; CHEN, S.; ZHANG, Y. Uncovering the Key role of the fermi level of the electron mediator in a Z-scheme photocatalyst by detecting the charge transfer process of WO3-metal-gC3N4 (Metal = Cu, Ag, Au). **ACS Applied Materials and Interfaces**, v. 8, n. 3, p. 2111–2119, 2016.

118 HARRISON, S.; HAYNE, M. Photoelectrolysis using Type-II semiconductor heterojunctions. **Scientific Reports**, v. 7, n. 1, p. 11638, 2017.

119 IQBAL, A.; KAFIZAS, A.; SOTELO-VAZQUEZ, C.; WILSON, R.; LING, M.; TAYLOR, A.; BLACKMAN, C.; BEVAN, K.; PARKIN, I.; QUESADA-CABRERA, R. Charge transport phenomena in heterojunction photocatalysts: the WO3/TiO2System as an archetypical model. **ACS Applied Materials and Interfaces**, v. 13, n. 8, p. 9781–9793, 2021.

120 FIGUEIREDO, V.; ELANGOVAN, E.; GONÇALVES, G.; BARQUINHA, P.; PEREIRA, L.; FRANCO, N.; ALVES, E.; MARTINS, R.; FORTUNATO, E. Effect of post-annealing on the properties of copper oxide thin films obtained from the oxidation of evaporated metallic copper. **Applied Surface Science**, v. 254, n. 13, p. 3949–3954, 2008.

121 LOS SANTOS VALLADARES, L.; SALINAS, D. H.; DOMINGUEZ, A. B.; NAJARRO, D. A.; KHONDAKER, S. I.; MITRELIAS, T.; BARNES, C. H. W.; AGUIAR, J. A.; MAJIMA, Y. Crystallization and electrical resistivity of Cu2O and CuO obtained by thermal oxidation of Cu thin films on SiO2/Si substrates. **Thin Solid Films**, v. 520, n. 20, p. 6368–6374, 2012.

122 DEBBICHI, L.; MARCO DE LUCAS, M. C.; PIERSON, J. F.; KRÜGER, P. Vibrational properties of CuO and Cu 4O 3 from first-principles calculations, and raman and infrared spectroscopy. **Journal of Physical Chemistry C**, v. 116, n. 18, p. 10232–10237, 2012.

123 KLICHE, G.; POPOVIC, Z. V. Far-infrared spectroscopic investigations on CuO. **Physical Review B**, v. 42, n. 16, p. 10060, 1990.

124 REICHARDT, W.; GOMPF, F.; AÏN, M.; WANKLYN, B. M. Lattice dynamics of cupric oxide. **Zeitschrift für Physik B:** condensed matter, v. 81, n. 1, p. 19–24, 1990.

125 LUNDIN, D.; GUDMUNDSSON, J. T.; MINEA, T. **High power impulse magnetron sputtering:** fundamentals, technologies, challenges and applications. Amsterdan: Elsevier, 2019. 384 p.

126 SANTHANAGOPALAN, D. *et al.* Surface chemical analysis of CuO nanofiber composite electrodes at different stages of lithiation/delithiation. **Journal of Power Sources**, v. 340, p. 356–364, 2017. DOI: 10.1016/j.jpowsour.2016.11.087.

127 BHATTACHARJEE, A.; MORYA, V.; GHOROI, C. Enzyme-mimetic activity of sugar cane juice stabilized CuO nanospheres and CuO/GO nanocomposite: green synthesis and applications. **Colloid and Interface Science Communications**, v. 35, p. 100239, 2020.DOI: 10.1016/j.colcom.2020.100239.

128 FORMAL, F. LE; TÉTREAULT, N.; CORNUZ, M.; MOEHL, T.; GRÄTZEL, M.; SIVULA, K. Passivating surface states on water splitting hematite photoanodes with alumina overlayers. **Chemical Science**, v. 2, n. 4, p. 737–743, 2011.

129 SIVULA, K.; FORMAL, F. LE; GRÄTZEL, M. Solar water splitting: progress using hematite (α-Fe2O3) photoelectrodes. **ChemSusChem**, v. 4, n. 4, p. 432–449, 2011.

130 WANG, Y.; LÜ, Y.; ZHAN, W.; XIE, Z.; KUANG, Q.; ZHENG, L. Synthesis of porous Cu2O/CuO cages using Cu-based metal–organic frameworks as templates and their gas-sensing properties. **Journal of Materials Chemistry A**, v. 3, n. 24, p. 12796–12803, 2015.

131FORMAL, F. LE; SIVULA, K.; GRÄTZEL, M. The transient photocurrent and photovoltage behavior of a hematite photoanode under working conditions and the influence of surface treatments. **Journal of Physical Chemistry C**, v. 116, n. 51, p. 26707–26720, 2012.

132 AHMET, I. Y.; BERGLUND, S.; CHEMSEDDINE, A.; BOGDANOFF, P.; PRÄG, R. F.; ABDI, F. F.; KROL, R. van de. Planar and nanostructured n-Si/Metal-Oxide/WO3/BiVO4 monolithic tandem devices for unassisted solar water splitting. **Advanced Energy and Sustainability Research**, v. 1, n. 2, p. 2000037, 2020.